THE DESIGN & CONSTRUCTION OF THE BEAM SCINTILLATION COUNTER FOR CMS

A thesis
submitted in partial fulfillment
of the requirements for the degree of
Master of Science in Physics
at the University of Canterbury
by

Alan J. Bell

University of Canterbury

2008

Abstract

This thesis presents the design qualification and construction of the Beam Scintillator Counter (BSC) for the CMS Collaboration at CERN in 2007 - 2008. The BSC detector is designed to aid in the commissioning of the Compact Muon Solenoid (CMS) during the first 2 years of operation and provide technical triggering for beam halo and minimum-bias events. Using plastic scintillator tiles mounted at both ends of CMS, it will detect minimum ionizing particles through the low-to-mid luminosity phases of the Large Hadron Collider (LHC) commissioning. During these early phases, the BSC will provide probably the most interesting and widely used data of any of the CMS sub-detectors and will be employed in the track based alignment procedure of the central tracker and commissioning of the Forward Hadron Calorimeter.

Contents

List of Figures

List of Tables

List of Acronyms

ASIC - Application Specific Integrated Circuit

ADC - Analog-to-Digital Converter

ATLAS - A Toroidal LHC Apparatus

BCM - Beam Conditions Monitor. Part of the BRM groups' detector responsibilities.

BRM - Beam Radiation Monitoring

BSC - Beam Scintillator Counter

CERN - Conseil Européen pour la Recherche Nucléaire

CMS - Compact Muon Solenoid

ECL - Emitter Coupled Logic. An electronics logic family where the input and output stages a driven by differential signals. The transistors in these stages are always biased on providing the ability for very fast switching at the expense of higher power consumption. Used when fast, low noise data transfer is required. *HAL* - Hardware Access Library. CERN designed software which allows high level VME module access and eases development of readout system designs

LEP - Large Electron Positron Collider. Hugely successful predecessor of the LHC. *LHC* - Large Hadron Collider. 27km proton-proton collider with

a com energy of 14TeV, the largest and most powerful particle accelerator ever built.

LHCb - Large Hadron Collider Beauty Experiment

PS - Proton Synchrotron. *PMT / PM tube* - Photomultiplier tube. *PVT* - Polyvinyl Toluene (Plastic Scintillator)

NIM - Nuclear Instrumentation Module. An electronics module standard. Since superseded by VME.

Radmon - Radiation Monitoring. RadFET and Alanine based radiation dose measuring detector located at several points around the UXC cavern.

SPS - Super-Proton Synchrotron. *TDC* - Time-to-Digital Converter

TOTEM - Total Cross-Section & Elastic Scattering Experiment

UXC - Underground Experimental Cavern

USC - Underground Service Cavern

VME - Versa Module Europa. An electronics module standard that allows control and acquisition via a PC via a PCI-VME interface.

Foreword

The Compact Muon Solenoid (CMS) is currently being constructed at the European Center for Nuclear Research (CERN). It is one of the two main experiments on the Large Hadron Collider (LHC) ring, the other being ATLAS. An overview of the LHC with focus on the CMS experiment and the requirements for beam monitoring and triggering is given in the introductory chapter 1.

Chapter 2 explains the physics behind why the BRM detector systems are required. In the early stages of the LHC operation, there will be many factors which will contribute to beam losses and the generation of particles in the beam pipe upstream of the CMS detector. These particles constitute a background of particles passing into and sometimes through the CMS detector and it is vital that their quantity is measured and minimized in order to measure the collision product particles produced in the heart of CMS by the coming together of the proton-proton beams.

CMS is commonly referred to as a detector, although, strictly speaking, it is a collection of many detectors, each with its own specialized purpose. Most of these detectors are designed to record the energies, momenta and directions of the millions of particles that are emitted from the interaction point every second. However, there is a small group of detectors whose purpose is to measure the quality of the incoming particle beams before the collisions take place and to record the radiation doses to the CMS experimental cavern throughout the running of the CMS experiment and protect the experiment from damage in the event of loss of beam control. These detectors belong

to the Beam & Radiation Monitoring (BRM) Group and are described in chapter 3. One of the BRM subsystems is the Beam Scintillation Counter (BSC) and during the initial operational phase of the LHC it will produce important data on the beam conditions for CMS.

The BSC design can be considered of consisting of two main parts. The first, explained in chapters 4 and 5 is the front-end (i.e. near the detector) hardware and the environmental factors which determine its layout and design. The tests carried out on the hardware are described in chapter 7. The second part is the readout electronics situated approximately 70 m away and accepts the signals from the front-end hardware.

Electrical noise is a potential problem with such a large scale detector. Incorrect wiring of a sub-detector like the BSC can cause severe noise and power supply problems not only within the sub-detector itself, but also neighboring sub-detectors. The overall high voltage and grounding schemes of the BSC and the Electromagnetic Compatibility (EMC) requirements of the underground experimental cavern (UXC) are described in chapter 6.

The BSC has two separate readout systems which are described in detail in chapter 8. One system is designed to measure the rates of incoming background particles and outgoing collision product and background particles and is described in the first part of chapter 8. The second role of the BSC is to provide halo triggering information to other sub-detectors either for commissioning phase alignment or as part of a veto trigger, discarding the information from a particular event if the background rates are too great, as explained in chapter 10.3. The design of the technical trigger readout is explained in the second part of chapter 8.

An invaluable part of the development procedure for any particle physics detector is the use of particle accelerators as 'test beams'. These accelerators provide high energy particles that simulate the expected environment in which the detector is to operate. Two of these 'test beam' opportunities were exploited during the latter half of 2007 and the data gathered was used to aide in the design of the BSC as well as characterizing the front-end hardware. The details of these tests are given in chapter 9.

The data produced by the BSC system must be available to the BRM and CMS databases for online and postmortem analysis. The data exchange for a large multi-detector system such as CMS is complicated. However, software tools are available which handle the data flow with the minimum required effort of the sender or the receiver. These systems with regards to the BSC and BRM sub-system data are described in chapter 10. The technical triggering scheme which will send data to the Global Trigger is also explained in this chapter.

The BSC is due for completion in May 2008. Work on the final readout systems still needs to be completed and some mechanical installation work still remains. Once installed, the BSC will run continuously to take measurements of background cosmic rates before the LHC is made operational. Once the proton beams are circulating in the LHC, the BSC is expected to provide vital beam conditions data for approximately 2 years, after which time the scintillator tiles will have sustained fatal radiation damage. Chapter 11 summarizes the conclusions made from the BSC design and construction so far and discusses the future plans for the current Beam Scintillator Counter and its possible upgrade.

Chapter 1

Introduction

1.1 CERN

Founded in 1954, CERN (Conseil Européen pour la Recherche Nucléaire)[12] is one of the most respected scientific research institutions in the world, specializing in the field of high energy particle physics. The CERN council began with the 12 founding Member States: Belgium, Denmark, France, the Federal Republic of Germany, Greece, Italy, the Netherlands, Norway, Sweden, Switzerland, the United Kingdom, and Yugoslavia. Today, the number of member states has expanded to 20 including Austria, Finland, Bulgaria, the Czech Republic, Poland, the Slovak Republic, Spain, Hungary and Portugal as well as many non-member state countries including New Zealand.

CERN is credited with many impressive particle physics discoveries. One of the first experimental achievements occurred in 1957 when the decay of a pion directly into an electron and a neutrino was observed using the 600MeV

synchro-cyclotron. Two years later, experiments involving illusive neutrinos began and have become a specialty of the laboratory with the Gran-Sasso experiment currently running which involves sending muon neutrinos through the Swiss Alps from Geneva to Gran-Sasso in Italy. The experiment is looking for evidence of neutrino oscillations and mass.

As a leading particle physics research center, CERN physicists are renowned for the development of new radiation detector media. The invention of multi-wire proportional chambers at CERN and drift chambers in 1968 started a new era of electronic particle physics detection*. Other important discoveries were made using the French-built Gargamelle bubble chamber in a neutrino beam at the Proton Synchrotron (PS) in 1973. It was found that neutrinos can interact with another particle without changing into a muon thus confirming the hypothesis of the existence of a neutral boson involved in weak interactions, the Z^0. This discovery, known as the 'neutral current interaction', pointed the way to uniting the weak and electromagnetic forces. In 1983, CERN announced the discovery of the W and Z bosons, mediators of the weak force, an achievement which earned the laboratory the Nobel Prize in 1984†.

For higher energy particle interactions, a larger accelerator needed to be built. The Large Electron and Positron (LEP) collider began in 1983. With a circumference of 27km, it remains the largest particle accelerator ever built‡.

* George Charpak received the Nobel Prize in 1992 for his work in the development of these detectors.

† Carlo Rubbia and Simon Van Der Meer shared the prize for heading the UA1 experiment and for work on developing antimatter storage rings respectively.

‡ More powerful magnets have been installed into the same tunnel and it is now known as the Large Hadron Collider, LHC.

Over its 15 year operation, LEP made extremely accurate measurements of the Z^0 particle width, the Z resonance parameters and reconstructed millions of Z particle decays [13].

CERN is now gearing up for the next phase of particle physics. The LHC will collide two proton beams at a center of mass energy $\sqrt{s} = 14\text{TeV}$ in the search for the Higgs boson.

1.2 The Large Hadron Collider

The Large Hadron Collider (LHC)[29] started construction in 1994 in the same tunnel that housed the hugely successful LEP (Large Electron Positron) accelerator 11 years previously. The LHC incorporates approximately 9300 superconducting magnets including 1232 dipole and 858 quadrupole magnets around its 27km circumference. The collider tunnel contains two pipes enclosed within these superconducting magnets cooled by liquid helium, each pipe containing a proton beam. The two beams travel in opposite directions around the ring. Sets of Inner Triplet Magnets are used to focus the beams together at four intersection points where interactions between them will take place. There will be five experiments positioned at the four interaction points (I.P); ALICE (**A** **L**arge **I**on **C**olliding **E**xperiment), LHCb (**L**arge **H**adron **C**ollidor **b**eauty experiment) and TOTEM* (Total Cross Section, Elastic Scattering and Diffraction Dissociation at the LHC) are three specialized experiments. The Compact Muon Solenoid (CMS) [17] and ATLAS (**A** **T**oroidal **L**HC **A**pparatu**S**) are the two main, multi-purpose experiments

* Totem co-inhabits Point 5 with CMS.

Collision Types	Proton/Proton & Heavy Ion.
Injected Beam Energy	450 GeV (Protons)
Nominal Beam Energy	7 TeV (Protons)
Operating Temperature	1.9 K
Magnetic Field	8.33 Tesla
RF Frequency	400.8 MHz
Revolution Frequency	11.2455 kHz

Table 1.1: Some statistics of the LHC[29].

positioned at Point 5 and Point 1 of the LHC ring respectively. Table 1.1 gives some vital statistics of the LHC accelerator. Of particular interest are the injection and collision energies of the proton beams which results in a collision *center of momentum* energy of 14TeV. The LHC operating temperature of 1.9K is achieved by liquid helium cryogenics which cools the superconducting magnets. An uncontrolled magnet quench near any of the experiments could result in a high helium concentration within the experimental cavern which must be guarded against. Figure 1.1 shows the path of the protons in the LHC and preliminary accelerators.

The protons make their way into the LHC by the following sequence (refer to figure 1.1):

1 The protons are produced by removing the electrons from Hydrogen atoms in the duoplasmatron giving 300mA of beam current at the start of Linac 2. The resulting protons are then injected into the proton Synchrotron Booster (PSB) at an initial energy of 50MeV by Linac 2.

2 The PSB accelerates the protons to an energy of 1.4GeV and feeds the beam into the Proton Synchrotron (PS).

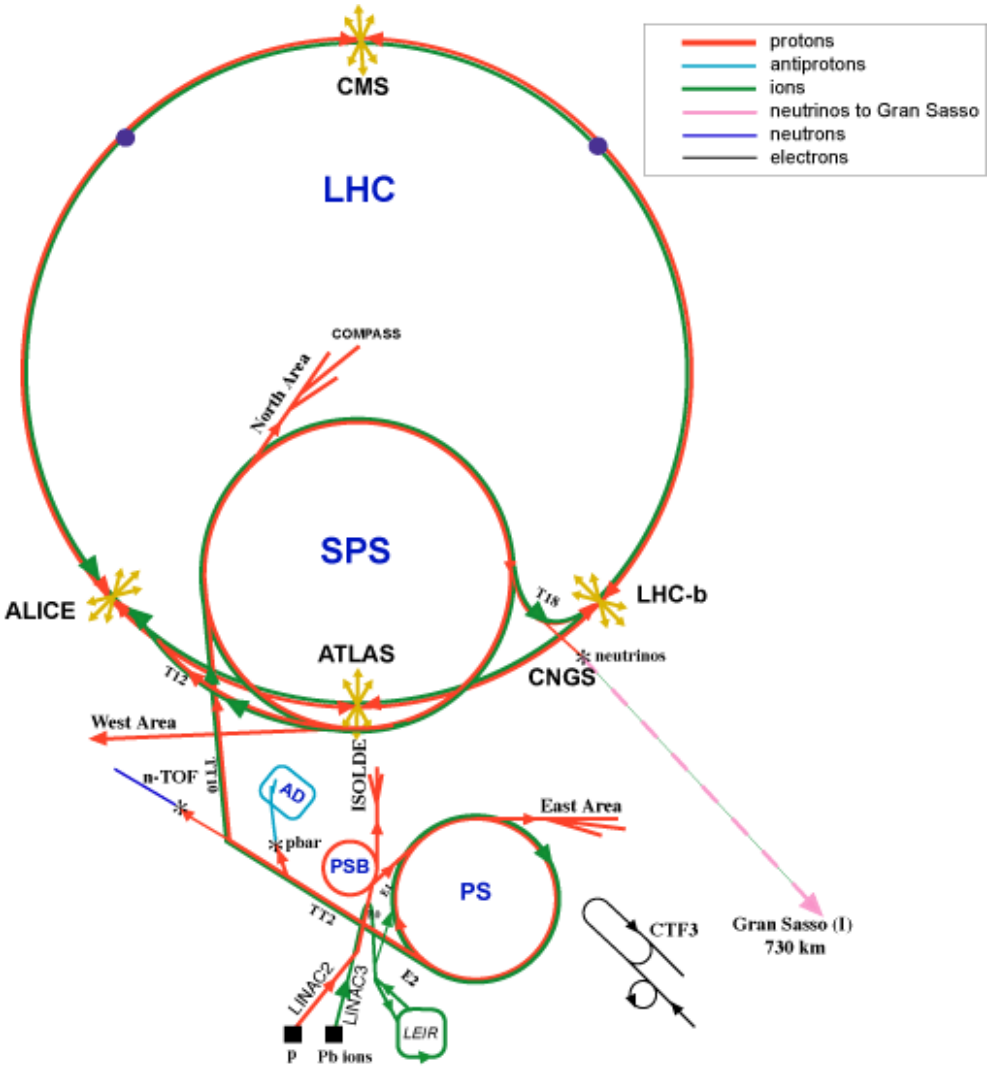

Figure 1.1: The path of the proton beams from production to injection into the LHC. LINAC = Linear Accelerator; PSB = Proton Synchrotron Booster; PS = Proton Synchrotron; SPS = Super-Proton Synchrotron; LHC = Large Hadron Collider.

3 The PS further accelerates the proton beam to 25GeV and sends them on to the Super-Proton Synchrotron (SPS). Here they are finally accelerated to the LHC injection energy of 450GeV. They enter the LHC in both clockwise and counter-clockwise directions. It will take approximately 20 minutes to accelerate the protons to the 7 TeV nominal LHC energy. They circulate the LHC beam-pipe in a carefully designed bunch pattern, shown in figures 1.2 and 1.3. This bunch pattern provides a 4-fold symmetry which ensures the 4 LHC experimental sites see 'full holes'. i.e. no experiment will experience a proton beam entering from one side whilst a beam gap enters from the opposite side. This will only occur during the beam dump kicker, a 3μs abort gap.

The proton beams will circulate for many hours under normal operating conditions. The beam intensity will decrease exponentially as the beam-beam interactions occur. This decrease in beam intensity should be discernible through the BSC and other BRM systems as the beams pass through the CMS cavern (UXC) at Point 5 on the LHC ring.

Figure 1.2 and figure 1.3 show the currently envisioned filling schemes for the LHC. Initially, only a single proton bunch of low luminosity ($\mathcal{L} = 10^{17} cm^{-2} s^{-1}$) will be injected into the LHC and accelerated to 450GeV. Over time, the luminosity will be increased along with the bunch fills and energy until the 75ns bunch spacing scheme is achieved. The BSC will play an important role during this early phase as it provides information of the beam dynamics and gives an early warning of alignment issues or the existence of gas within the beam-pipe. Either of these issues will cause a large amount

of scattered particles to enter the CMS detector giving rise to unwanted background or even a risk of catastrophic damage to the sensitive inner electronics. Eventually, the nominal 25ns bunch spacing and luminosity of $\mathcal{L} = 10^{34} cm^{-2} s^{-1}$ will be reached and the data gathering and analysis from *p-p* collisions with a center of momentum energy of 14 TeV will begin. It should be possible to view and monitor these bunch patterns directly with the BSC.

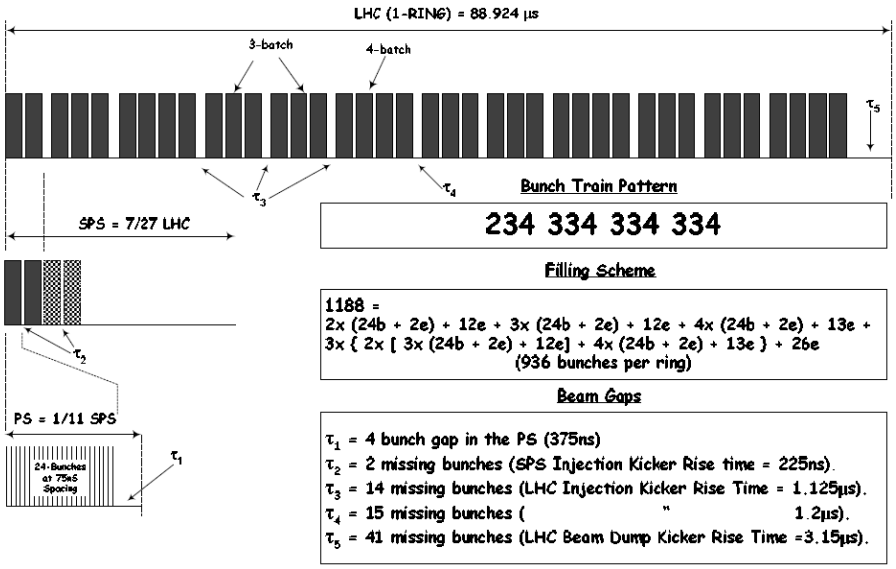

Figure 1.2: The proposed filling scheme of the LHC for the initial 75ns bunch spacing run [36]. One entire LHC orbit is shown. The protons are injected as 936 bunches. 24 of these bunches, spaced 75ns apart form one batch. The batches are injected in the pattern shown (234 334 334 334). In the table, 'b' represents RF buckets containing bunches, 'e' represents empty RF buckets.

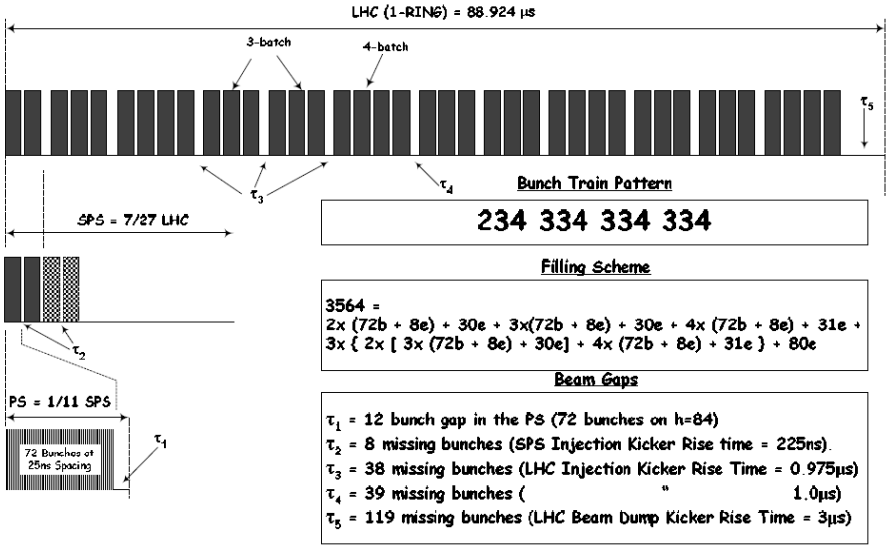

Figure 1.3: The proposed filling scheme of the LHC for the nominal 25ns bunch spacing run[36]. One entire LHC orbit is shown. The protons are injected as 2808 bunches. 24 of these bunches, spaced 25ns apart form one batch. The batches are injected in the pattern shown (234 334 334 334).

1.3 Aims of the ATLAS & CMS Experiments

CMS[] and ATLAS[] are the two general purpose detectors of the LHC. They have common goals but have radically different approaches to their design. Only measurements made in both detectors will be considered true. The main goals of the experiments are

- to explore particle physics cross-sections in the TeV scale.
- discover the Higgs boson, the gauge boson particle thought to be responsible for the property of mass.
- look for evidence of supersymmetry which would confirm the theory that explains the non-existence of anti-matter in the universe.

- search for extra dimensions, showing up as missing transverse energy [51].
- using Pb nuclei, study heavy ion collisions.
- make more accurate measurements of already discovered particles, for example, the top quark.

1.4 The Compact Muon Solenoid

The Compact Muon Solenoid (CMS) experiment is a general purpose detector designed to investigate particle physics at the highest energy accelerator in the world, namely the LHC. As well as looking for new physics beyond the standard model, CMS will perform precise measurements such as the mass of the top quark and other parameters of the Standard Model. This is in part due to the high event rates of the LHC. Some important processes are given in table 1.2 for the luminosity of $\mathcal{L} = 2 \times 10^{33} cm^{-2} s^{-1}$.

Process	Events/s	Events/year
$W \rightarrow ev$	40	4×10^8
$Z \rightarrow ee$	4	4×10^7
$t\bar{t}$	1.6	1.6×10^7
$b\bar{b}$	10^6	10^{13}
Higgs (m = 120GeV)	0.002	2×10^4
Higgs (m = 800GeV)	0.001	1×10^4
QCD jets $p_T > 200GeV$	10^2	10^9

Table 1.2: Predicted event rates of some physics processes at the LHC for a luminosity of $\mathcal{L} = 2 \times 10^{33} cm^{-2} s^{-1}$ [53].

The CMS detector is being constructed at Point 5 of the LHC near

the French town of Cessy. The majority of the construction was done on the surface before being lowered 100m into the Underground eXperimental Cavern (UXC) in 11 'slices'.

The detector is built around a 13m long, 6m diameter superconducting solenoid with a core magnetic field of 4T. The innermost detector system is the central tracking system which consists of pixel detectors placed close to the interaction region. The pixel detectors have a spatial resolution of 15μm. Outward from the pixel trackers detectors are 25000 silicon microstrip detectors. It will generate data from a total of 9.6 million readout channels.

Lead Tungstate crystals ($PbWO_4$), a scintillating crystal is used in the electromagnetic calorimeter. This crystal offers excellent energy resolution (0.39GeV $\pm$ 0.01% measured with 120GeV electrons)[37] for photons and electrons, a vital characteristic for the calorimeter. The scintillation light is captured using avalanche photodiodes. The final detector in front of the magnetic coil is the Hadronic Calorimeter which uses quartz scintillators sandwiched with copper as its detector medium.

Embedded within the magnetic field return yoke are four layers of muon chambers. Each muon station consists of twelve planes of aluminum drift tubes (DT). Each of the four endcap stations consists of six planes of Cathode Strip Chambers (CSC). A second, fast and redundant, Level-1 trigger is provided by Resistive Plate Chambers (RPC)[17].

Together these detector layers make up the core of the CMS detector barrel.

1.4.1 CMS Coordinate System

With a large scale project such as CMS, it is vital that everyone involved is working to the same coordinate system. i.e. the way which *x,y* and *z* are orientated within the UXC cavern. This information is included here to clarify subsequent sections describing topics such as mechanics and beam halo.

The CMS experimental cavern is situated 100m underground on the northern side of the LHC ring. The coordinate system has been defined as follows[19].

- The x axis is horizontal, pointing south towards the LHC center.
- The y axis is vertical pointing upwards.
- The z axis is horizontal pointing west.
- The sign of pseudo-rapidity, $\eta = -\ln\tan(\frac{\theta}{2})$ is equal to the sign of z.
- The polar angle θ is measured w.r.t. the z axis:

  $\theta = 0$ is $+z$ axis, $\theta = \pi$ is -z axis.

- The azimuthal angle ϕ is measured in the x/y plane:

  $\phi = 0$ is $+x$ axis, $\phi = \pi/2$ is $+y$ axis, $\phi = atan2(y, x)$.

Pseudorapidity, describes the angle of a particle relative to the beam axis. To first order, particle production is a function of rapidity.

Therefore, the beam-lines pass through the CMS cavern in the direction of $+z$ and -z. The CMS detector's exterior structures are approximately

symmetrical in x and z orientations and locations on the detector are described by their relevant x and z sign. The Forward Hadron (HF) Calorimeters, for example are referred to as +HF on the $+z$ end and -HF on the -z end. Similarly, $+x$ refers to the side of the CMS detector closest the center of the LHC ring and -x to the outer side.

1.5 Purpose of Beam Radiation Monitoring

During the nominal p-p beam collision operation, the LHC will store 2808 bunches of 10^{11} protons at 7TeV [36]. The total energy stored can be as high as 0.35GJ and a loss of as little as 3×10^{-9} of this energy can have a serious impact on the operation of the LHC [16]. These beams, if poorly defined, will deposit their energy in the LHC magnet coils and may cause the magnets to quench or even permanently damage the coils. Additional monitoring is required in the regions of the experimental detectors to protect the innermost electronics. This monitoring must provide fast feedback to the LHC control to optimize beam conditions; provide fast triggering ($< 500\mu s$) of a beam abort should the beam losses exceed the predefined threshold and send postmortem data in the event of a beam abort for diagnostic purposes to help prevent the same problem occurring.

The response time and monitoring rates of the beam monitoring systems are more critical in the CMS experiment due to the proximity of the beam dump kicker, a series of fast steering magnets upstream at point 6 which deflect the beams into absorber material. These magnets are intended to switch on only during the beam abort gap shown in figures 1.2 and 1.3 and

therefore require a minimum ramp time of $3\mu s$.

There are many possible causes for the beam-dump kicker to malfunction resulting in a loss of approximately 1×10^{12} protons into the CMS cavern in a period of about 1μs [33]. In the case of an unsynchronized beam abort, the tracker detectors of CMS must withstand instantaneous dose rates 10^8 times above normal conditions [32]. The beam monitoring systems in CMS must also measure the integrated dose to the experiment both during normal running and during beam-abort scenarios to help assess the level of radiation damage sustained by the CMS sub-detectors.

1.6 Purpose of technical triggering

One of the critical steps in the run-up to physics data taking for CMS is the alignment and commissioning of the various detector systems such as the pixel tracker and silicon micro-strip detectors. The general alignment strategy for CMS is as follows [52].

- precise position measurements during assembly of the detector.
- measurements of the relative positions of the sub-detectors with a dedicated hardware alignment system.
- Track-based alignment.

The eventual precision required of the inner tracker, for example is less than 10μm in ϕ. However, the alignment uncertainties resulting from position measurements and the hardware alignment systems alone are expected to be

in the range of 100 - 500μm. Hence, for the tracker, Track Based Alignment is the most important part of the alignment strategy.

Track based alignment involves using the tracks left from particles passing through the detectors to align those same detectors. High energy (> 100GeV) muons (μ^+/μ^-) are the most suitable particle for this purpose due to being charged* and being leptons†. Therefore, Track Based Alignment can only be implemented once there is beam in the LHC. Several Track Based Alignment algorithms have been considered which involve various decay schemes resulting in μ^+/μ^- tracks. Two examples are the $W^{\pm} \rightarrow \mu^{\pm}\upsilon$ and $Z^0 \rightarrow \mu^+\mu^-$.

At low luminosity ($\mathcal{L} = 10^{33} cm^{-2} s^{-1}$), it has been calculated that approximately 20000 Z^0 and 100000 $W^{\pm}$ events per day will be selected by the high level trigger (HLT). It is estimated that between 1 - 2 million tracks are required to align the tracker (1 - 2 weeks of data). During the initial pilot runs of the LHC, the luminosity will be much lower than $10^{33} cm^{-2} s^{-1}$ and the availability of the $W^{\pm}$ and Z^0 decay products will be several orders of magnitude less.

An alternative source of alignment tracks comes from *beam halo events*. These interactions are essentially part of the background noise of the LHC resulting from spurious collisions between the accelerated beams at places other than the intended interaction points. Collision products with low transverse momentum (p_t) traveling almost horizontal to the beam axis could

* Most devices are only capable of detecting charged particles without the use of a conversion material.

† Leptons are not subject to the weak force and will penetrate much further than hadrons of similar energy.

be useful for tracker alignment, especially for the forward region detectors (large η) where the detector geometry is typically perpendicular to the beam axis. During the initial low luminosity run ($\mathcal{L} = 10^{28} cm^{-2} s^{-1}$), these may in fact be the only source of muon tracks available for alignment purposes. Cosmic muons and Beam Halo muons will also be useful for alignment of the tracker [52].

Whichever event causes the passage of high energy muons through the CMS, in order to be useful as a Track Based Alignment tool, a suitable triggering device will be required. The TOTEM T1 telescope is expected to help provide some triggering for such a purpose. The BSC will be sensitive to minimum ionizing particles generated from beam gas collisions and from minimum bias, low p_t events thus being capable of providing a suitable trigger signal.

Chapter 2

Beam Luminosity & Conditions

The search for new physics, mentioned in chapter 1 will not commence until the extensive testing and commissioning of the LHC and its detectors (CMS, ATLAS, LHCb, TOTEM and ALICE) is completed. In addition, with the potential of 0.35GJ of energy being stored within the circulating protons, there is a serious potential for a catastrophic failure if the LHC magnets, collimators, cooling systems, vacuum systems and kicker magnets are not fine tuned and their operation clearly understood. The energy stored within the protons in the LHC ring is sufficient to melt 2 tonnes of copper, so the commissioning phases will be carried out with meticulous precision to prevent any serious failure. This chapter explains the LHC commissioning phases during which the BSC will be one of the most important tools for CMS. Also described are the mechanisms by which large quantities of background particles can be generated. It is the quantities and timings of these particles that the BSC data must record.

2.1 LHC Commissioning

An important characteristic of any particle collider is its luminosity. This is defined as the number of collision particles per unit area per unit time (usually given in $\mathrm{cm}^{-2}\mathrm{s}^{-1}$) at the target (interaction point). The target proton luminosity of the LHC is $10^{34}\mathrm{cm}^{-2}\mathrm{s}^{-1}$ at an energy of 7TeV per beam. At the time of writing, the LHC is complete and commissioning with beam is scheduled to commence in June 2008 and will be performed in the following stages[34]:

- Stage A. Initial commissioning with a single bunch in both directions ($\mathcal{L} = 1 \times 10^{27} cm^{-2} s^{-1}$ and a bunch intensity of 10^{10}) moving toward 43 on 43 bunches and finally to 156 on 156 bunches with a gradually increasing bunch intensity up to 9×10^{10}. Conditions for first collisions are expected to be achieved after 30 days. Stage A is expected to take 44 days.

- Stage B. Move to 75 ns bunch spacing with the aim of moving to intensities around $3 - 4 \times 10^{10}$ particles per bunch. During the entirety of this phase, the LHC will carry 936 bunches in each direction with a bunch intensity increasing from 4×10^{10} to 6×10^{10} particles per bunch. The target luminosity for this phase is 5×10^{32}.

- Stage C. Move to 25 ns bunch spacing with the aim of moving to intensities around $3 - 4 \times 10^{10}$ particles per bunch. With the bunch spacing reduced to 25ns, the LHC will circulate 2808 bunches in each direction. The bunch intensity will be steadily increased up to 6×10^{10}

particles per bunch and a luminosity of 2.8×10^{33}. The expected average number of events per bunch crossing is only 5.2 at this stage. Stage C will be follower be a long shutdown period for installation of additional collimators and beam dump diluters.

- Stage D. Nominal 25 ns running pushing toward design intensity and full squeeze. The intensity of the 2808 proton bunches will be increased to 1.15^{11} and a luminosity of $1.0 \times 10^{34} cm^{-2} s^{-1}$. The event rate per bunch crossing at the interaction point will increase to approximately 19.

Overall, it is expected to take approximately 3 years before nominal luminosity in the LHC is reached.

2.2 Beam-Pipe Wall & Beam Gas Interactions

In the ideal scenario, interactions with the accelerated proton beams would occur solely at the designated Interaction Points. In reality, this is not the case and a significant fraction of the proton beams could be lost. Beam losses occur due to interactions with collimators which are intended to remove off-energy particles from the beam. Additionally, the beam optics which are tuned to deal with proton beams of specific energy will also cause the loss of protons whose energy falls outside the necessary energy range, possibly due to a close encounter with the collimators or beam-pipe wall. Another loss occurs due to an imperfect vacuum within the beam-pipe. The incoming

proton beam can collide with residual gas within the beam pipe producing many particles that deposit their energy in to the detectors at the forward regions. Also, until the LHC control is fully understood, collisions between the proton beam and the beam pipe walls will frequently occur.

On entry to the LHC ring, the protons will already have been accelerated to 450GeV [29], which is more than enough to create new particles if collisions occur with residual beam gases. Of greatest concern are the long lived particles that are able to penetrate in to the heart of the CMS detector, clouding the desired signals behind a shower of background noise.

Throughout the running of the LHC and particularly the early phases of operation, it will be necessary to be able to detect when these types of interactions and subsequent particle creations occur. Hadrons are the most abundant particles created in such collisions. However, most will be removed by the collimators and shielding before entering the detector. Lepton particles are relatively rare products of beam gas collisions but are much more penetrating. In fact, one tell-tale signature of beam gas events is the passage of high energy μ^- and μ^+, the latter of which are created as shown in the Feynman diagram of figure 2.1.

New particles can be created from the interaction of the proton beams and residual gas within the beam pipe. Perhaps the most abundant are positive and negative pions (π^+, π^-).

Imagine a beam proton colliding with a nucleus of a stationary hydrogen atom, i.e. a proton. The protons have a rest mass energy of 938MeV. A π^+ has a rest mass energy of 140MeV. In the center-of-momentum (com) frame, the total momentum is zero and all the energy is made up of the proton's

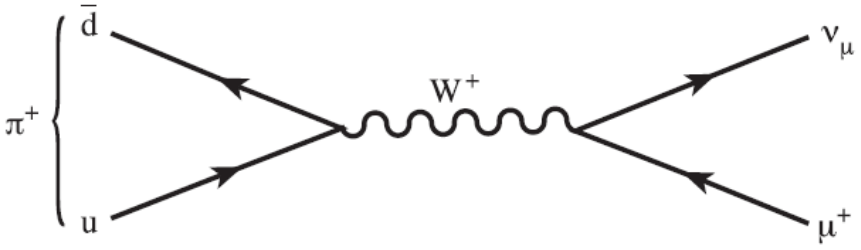

Figure 2.1: The pions created in beam gas events decay to $\mu^+/\mu^-$with a branching ratio of 99.9877% [59].

mass energy m_p. The minimum excess energy required to create a π^+ is 140MeV, or 70MeV per proton. Thus,

$$E_{Total} = E_{mass} + K.E \tag{2.1}$$

Before Collision

$$E_{Total} = 2m_pc^2 + K.E \tag{2.2}$$

After Collision

$$E_{Total} = (2m_pc^2) + m_\pi c^2 + 0 \tag{2.3}$$

Therefore,

$$K.E = m_\pi c^2 = 140MeV \tag{2.4}$$

The kinetic energy is shared equally between the two protons. Each proton has a total energy of,

$$E_{Total} = m_pc^2 + 70MeV = 1008MeV. \tag{2.5}$$

Using the equation for relativistic mass,

$$m = \frac{m_0}{\sqrt{(1-\beta^2)}} \tag{2.6}$$

where $\beta = \frac{v^2}{c^2}$, we can calculate the velocity based on the protons' mass.

$$\frac{938}{1008} = 0.9226 = \sqrt{(1-(\beta^2))} \tag{2.7}$$

$$\beta = \sqrt{(1 - 0.9226^2)} = 0.38c \tag{2.8}$$

The velocity of the two protons in the *com* frame is ± 0.38c. In the lab frame, this means that the incoming beam proton need only have a velocity of 0.76c, or an energy of 1.44GeV. This is far less than the 450GeV injection energy of the LHC. Even with careful vacuum pumping and cooling of the beam pipe, collisions with residual gases is still expected to occur frequently during the first few months of LHC operation.

The π^+/π^-particles have an average lifetime of $2.603 \times 10^{-8} s^*$[59] before they decay. 99.9% of the charged pion decays result in the production of a $\mu^+/\mu^-$and an muon neutrino ν [59]. The μ^+/μ^- particles will continue to travel as a cloud parallel with the beampipe and roughly in time with the *p*-*p* bunches. Muons, being leptons do not interact via the strong force and with a rest mass of 105.6MeV are too massive to be significantly deflected by atomic electric fields that they encounter. They are therefore deeply penetrating, so much so that these *beam halo muons* are capable of passing through the entire 22m length of the CMS detector, inducing undesired signals as they interact with the tracker detectors and calorimeters.

However, these same halo muons can be useful in aligning the tracker elements as explained in section 1.6 of chapter 1. The halo muons will create tracks in the pixel tracker or strip detectors. These tracks will show where the detectors are misaligned and enable their positions to be corrected for the tracking of collision product particles after the commissioning phase.

In both cases, it is important to trigger on these halo muon rich events.

* Lifetime in the rest frame.

In the first case, the trigger acts as a veto, discarding the data of that particular bunch crossing. With large amounts of μ^+/μ^-background, any further analysis of the data generated from the collision would be futile and so the event in question can be removed from the pipeline, as described in section 10.3. In the second scenario, the beam halo passing through the detector causes a trigger to record the event, thus producing data images of the paths through the pixel tracker. Without triggering, every event would have to be recorded and analyzed during the alignment procedure, creating a vast amount of data that would need to be stored. Triggering on only halo muon rich events will reduce the data storage requirements and processing time considerably.

Chapter 3

BRM Subsystems

It is the task of the Beam Radiation Monitoring (BRM) group to develop hardware and software systems which will monitor all possible aspects and conditions of the LHC *p-p* beams. This includes the measurements of particle flux rates close to the beam pipe (BCM1-L, BCM1-F and BCM2), radiation doses around the CMS cavern (RADMON & Passives) beam intensity, positioning and timing relative to the CMS clock (BPTX) and general background particle rates (BSC). The group consists of the following Universities and Institutions.

- BCM1-F : CERN, DESY-Zeuten (Germany), Rutgers (New Jersey, USA).
- BSC : University of Canterbury and University of Auckland (New Zealand), CERN.
- BCM : Interface: University of Tennessee (Knoxville, USA), CERN.
- BCM1-L : Princeton University (New Jersey, USA), Rutgers (New

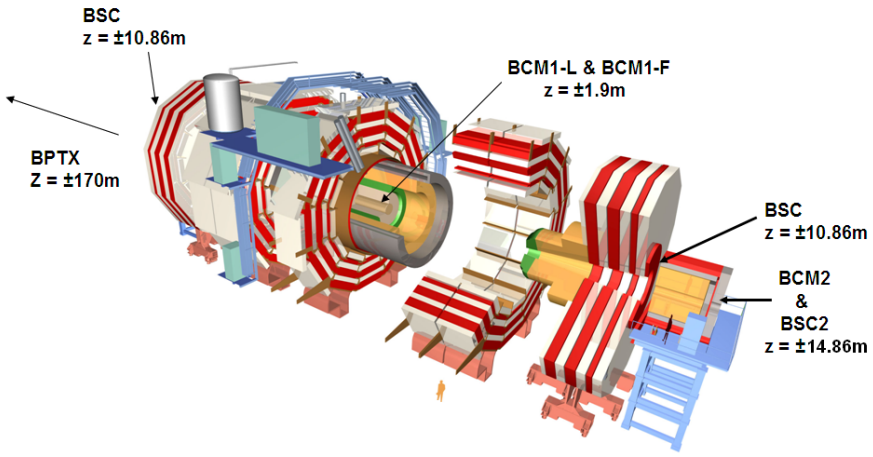

Figure 3.1: 3D diagram of the Compact Muon Solenoid. The 21.5 m long, 15 m diameter solenoid contains a 4T magnetic field. Radiation monitoring detectors are placed at points along the detector depending on their specific aims.

Jersey, USA), CERN.

- BCM2 : Universität Karlsruhe (Germany), CERN, Rutgers (New Jersey, USA).

- BPTX : Technische Universitaet (Wien, Austria), CERN.

Figure 3.1 shows the positions of each of the detectors of the BRM group. The data from all these detectors are handled by the BRM Interface[49].

Table 3.1 lists each of the BRM sub-systems along with their position, sampling time, and primary functions.

The seven sub-systems were chosen to gather the widest range of information on the radiation and beam conditions in the CMS experiment. Each system has it own specialized purpose and in most cases, there is a

Subsystem	**Position**	**Sampling Time**	**Function**
Passives TLD & Alanine	In CMS & UXC	Long Term	Monitoring
RADMON	18 months around CMS	1s	Monitoring
BCM2 Diamonds	$z = \pm 14.4m$	$40\mu s$	Protection
BCM1L Diamonds	$z = \pm 1.8m$	Sub-orbit 5μs	Protection
BSC Scintillator	$z = \pm 10.86m$ & $z = \pm 14.4m$	Bunch-by-Bunch	Monitoring
BCM1F Diamonds	$z = \pm 1.8m$	Bunch-by-Bunch	Monitoring & Protection
BPTX	$z = \pm 175m$	200ps	Monitoring

Table 3.1: BRM sub-system overview[40].

crossover of the data gathered so that one system can be used to commission and crosscheck another system, particularly during the early stages of the LHC[1, 4]. The following sections give a brief description of the BRM subsystems including their detector medium and purpose.

3.1 The BCM Subsystem

In CMS there are two protection systems foreseen for initial LHC operation. The first is the BCM1L which is four polycrystalline diamonds[15, 58, 45], each 10×10×0.4mm, positioned on either side of the IP at Z values of ± 1.8 m, close to the beam pipe and the pixel detectors at a radius of 4.5 cm. The second protection system is the BCM2L. This is a set of twelve polycrystalline diamonds on either side of the IP behind the TOTEM T2 detector at a z position of ± 14.4 m

Here BCM refers to Beam Conditions Monitor, the index 1 or 2 refers to the two locations in z and the final character L indicates that these detectors are used in a leakage current measurement mode as relative flux monitors, typically integrating the leakage current over micro-second time scales. The BCM1L diamonds are arranged on the x and y axes.

The BCM2L comprises eight diamonds at 45° intervals at radius and four on the x,y axes at small radius. One of these diamonds is shown in figure 3.2. The diamond (the dark square) has a metalized coating on to which several thin wires are bonded to take the picoAmp signals to the output connector on the right hand side. The left hand connector supplies a 100V/μm bias voltage. The BCM1L and inner BCM2L diamonds measure a rate which is

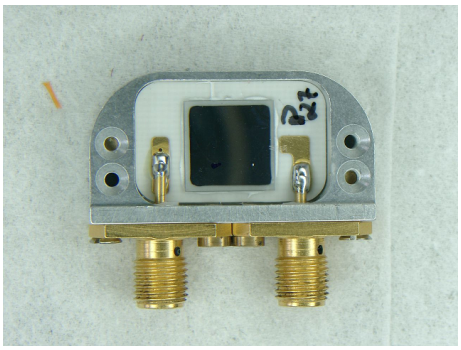

Figure 3.2: The BCM2 diamond ($1cm^2$) in its housing. The wire bonds to the metalization can be seen on the right hand side of the diamond.

dominated by pp interactions at the IP. The outer BCM2L diamonds are hidden from the beam-spot and are expected to be largely sensitive to beam-halo rates.

The diamonds used for BCM1L and BCM2L are essentially identical, but the two systems differ in the read out methods adopted. The BCM2L uses a completely standard LHC Beam Loss Monitor (BLM) electronics and data processing [5, 7] that is read out asynchronously with the LHC machine with 40 μs sampling. The BCM1L readout uses the same LHC BLM backend electronics, but uses an additional mezzanine card to provide sub-orbit sampling. The readout is synchronized with the LHC orbit, allowing user-configurable sampling over the 89 μs orbit so that the sampling can be matched to the bunch trains within the LHC orbit. In addition the BCM1L allows sampling of the LHC abort gap, which must be kept empty to avoid a spray of particles being directed at CMS during a beam dump.

Using a set of thresholds in the readout systems and a combinatorial logic to reduce sensitivity to individual noise events, a hardware beam abort signal can be generated and transmitted to the LHC machine via the Beam Interlock

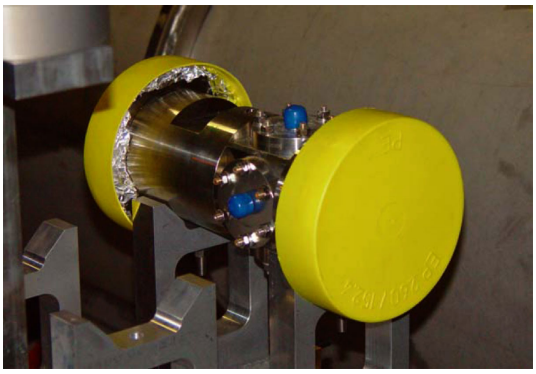

Figure 3.3: One of the BPTX stations situated $\pm 175m$ from the I.P.

System [41], leading to the dumping of the beams within 3 orbits. A lower threshold value can be used to send hardware signals to CMS sub-detector clients to initiate high and/or low voltage ramp-downs.

In the event of a beam abort initiated by CMS, or any of the other LHC- or experiment- protection systems, a full history of the BCM1L and BCM2L signals is produced and transmitted to the CMS and LHC control room for postmortem diagnosis in the event of a beam abort[39].

3.2 The Beam Position Monitor (BPTX)

The BPTX sub-system is designed to measure the bunch-by-bunch timing and structure of the p-p beams in the region of the CMS cavern. It consists of two electrostatic pick-up stations located at $z = \pm 175m$ from the interaction point (Figure 3.3). Identical pick up detectors are positioned at various points around the LHC including ATLAS and LHCb. As the proton bunches pass the stations, a mirror charge is induced in the detectors causing a signal which is used for monitoring the timing of a bunch structure of the beams[50].

A commercial 4-channel high-resolution oscilloscope running Linux and LabView Virtual Instruments are used as the BPTX readout and will capture an entire LHC orbit every 2 seconds with a time resolution of <200ps. The data from the BPTX will be used in the initial commissioning of the BSC sub-system.

3.3 RADMON & Passives

RADMON (radiation monitoring) and the Passive dose meters are to be put in place to measure the short term and long term radiation dose to the CMS cavern. RADMON uses RadFETs (Radiation sensitive Field Effect Transistors) at 16 points within the cavern close to the equipment racks. Each RadFET is readout along a common trunk line at a sample rate between 1 per $100ms$ - 1s. The information provided from RADMON will tell if the equipment shielding needs to be improved to prevent excessive radiation damage to the electronic equipment. It will also act as an early warning if radiation levels in the cavern unexpectedly increase. The system is capable of determining the radiation dose with a 1rad (0.01Gy) resolution [24].

The Passive detectors use Alanine and Thermo-luminescent Dosimeter (TLDs) to monitor the long term radiation dose within the cavern. Alanine is an amino acid which forms radicals when exposed to ionizing radiation. The amount of radicals formed is proportional to the radiation dose absorbed by the dose meter. Alanine dose meters cover a dose range from several Gy up to several 100 kGy. The read-out method of the dose meters is based on Electron Paramagnetic Resonance (EPR) which allows the determination

of the total quantity of produced radicals formed within the Alanine crystal and thus the absorbed dose [31].

Thermo-luminescent Dosimeter (TLDs) are also in place to act as a cross check for the RADMON detector. These crystal structures operate in a similar way to the Alanine crystals. However, the readout of the TLDs involves heating the crystal to liberate the electrons trapped within the lattice, the quantity of which is a function of the absorbed dose. During this process, the electrons returning to their ground state emit light. Therefore the amount of light detected is proportional to the dose absorbed by the crystal.

Together, the RADMON system and the passive dosimeters will give information which will be used to calculate the expected lifetime of the electronics in the UXC cavern, determined by the absorbed dose in the various regions.

3.4 The Beam Scintillation Counter

The Beam Scintillation Counter is the only BRM subsystem capable of detecting minimum ionizing particles (MIPs). Its primary goals are to measure the relative rates of background particles and collision products entering and exiting the CMS experiment. Detectors like the BSC have been invaluable in previous high energy physics experiments such as Zeus [26] and FermiLab's Tevetron. The detector medium is made from polyvinyl-toluene plastic scintillator which when hit by high energy charged particles, emits light which is the basis of the signal. From the pulse heights and rates, the

quantity of charged particles passing through the scintillator tiles can be estimated. The directions of the particles can be determined from the times at which the signals arrive from the tiles and front end hardware.

The design, qualification and implementation of this detector forms the subject of the rest of this thesis.

Chapter 4

Scintillator Mechanisms

Scintillation materials are widely used in high energy particle physics detectors due to their sensitivity and fast response times. Coupled with a suitable photomultiplier tube, they make a very robust, cost effective detection system. The BSC uses plastic *polyvinyl-toluene* (PVT) scintillation tiles with wavelength shifting fibres (WLS). The photomultiplier (PM) tubes were chosen for their sensitivity to the output light from the WLS fibres.

The output signal characteristics from the scintillation tile and PM tube pair varies for different incident particle types and energies. It is important to understand the underlying mechanisms in order to analyze the results of both the SPS/PS test beam experiments and the signals from the BSC when the LHC becomes operational.

4.1 General Characteristics of Scintillators

Scintillators come in several forms; organic crystals, liquids, plastics, inorganic crystals, glasses and gases. The most common form used in particle physics and in the BSC sub-detector are plastic tiles. These are a form of organic scintillator but in a solid plastic solvent [60]. PVT is luminescent when irradiated by ionizing radiation and this luminescence yield is proportional to the radiation stopping power and to the absorbed dose.

When scintillator materials are exposed to energetic charged particles, some of the energy of these incident particles is absorbed and re-emitted as visible light in a process known as *luminescence*. In the case of the BSC detectors, the incident particles are usually cosmic muons, beam halo muons and high energy charged hadrons. These particles interact with the valance electrons in the scintillator compound exciting the electrons in to a singlet state (Spin paired $S = 0$). Some of the excited S^* electrons relax back to the ground state S_0. However, some will lose their energy in a non-radiative manner and settle temporarily in to a lower energy *triplet* state (at least one unpaired set of electron spins) denoted in figure 4.1 as T^* and T_0.

The electron energy transition from the excited S^* and S^{**} states to the ground state S_0 gives rise to the fast component of the scintillation emission. A transition from the T_0 state to the S_0 state is forbidden. However, two T_0 state molecules can interact to leave one of the molecules in the S^* state which then decays to S_0 radiating a photon. This mechanism gives rise to the slow component of the scintillation emission [60].

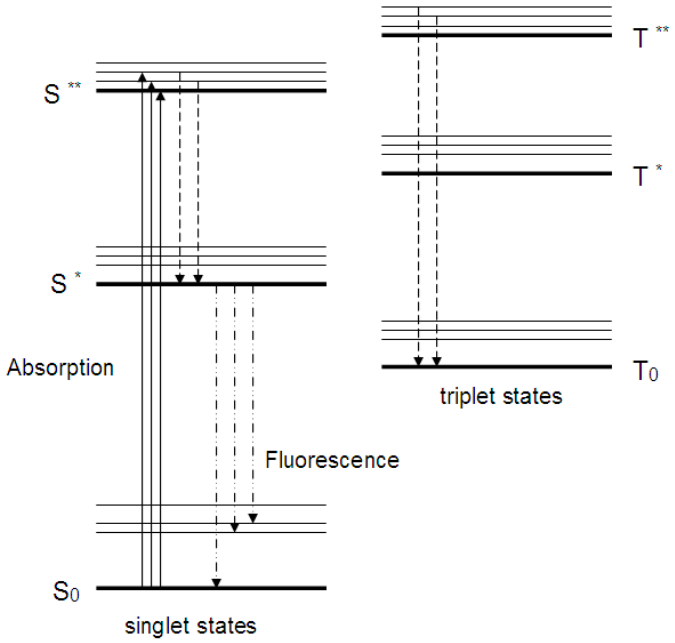

Figure 4.1: Energy diagram of plastic scintillator molecule. The singlet states are denoted by S_0, S^*, S^{**} and the triplet states by T_0, T^*, T^{**}.

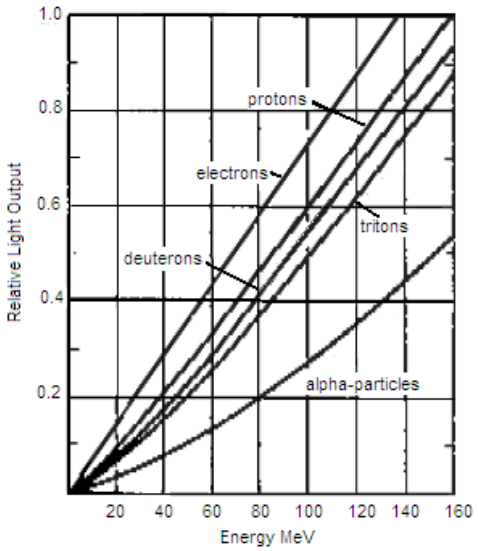

Figure 4.2: Response curve for polyvinyl toluene plastic scintillator material [46]. Output given relative to Anthracene.

4.1.1 Output Response

It is important to understand the way in which the particle types and energies influence the light output from the scintillator tiles. The efficiency and the resolution of the scintillator, and therefore the BSC front-end system is determined by the light output response with respect to the incident muon and hadron radiation energy deposits. Figure 4.2 shows the relative light output of BC408 polyvinyl toluene scintillator for various energies of electrons, deuterons, tritons, protons and alpha-particles. Light output is referenced to the output of anthracene scintillator. For all but extreme dose rates, the light output response of PVT can be taken as linear [38]*.

The mean rate of energy deposited by charged particles in matter is

* At high dose rates, exciton migration and exciton-exciton interactions can occur, causing a non-linear light yield.

described by the Bethe-Bloche equation, shown in Eq 4.1.

$$-\frac{dE}{dx} = Zz^2\frac{K}{A}\frac{1}{\beta^2}\left[\frac{1}{2}ln\frac{2m_ec^2\beta^2\gamma^2T_{max}}{I^2} - \beta^2 - \frac{\delta(\beta\gamma)}{2}\right] \tag{4.1}$$

- $-\frac{dE}{dx}$: Rate of energy loss per unit length by the incident charged particle.
- $\frac{K}{A}$: $4\pi N_A r_e^2 m_e c^2/A = 0.307075 MeV g^{-1} cm^2$.
- Z : Atomic number of the absorber.
- ze : Charge of incident particle.
- T_{max} : Maximum kinetic energy which can be imparted to a free electron in a single collision.
- I : Mean excitation energy in eV.
- γ : $\frac{1}{\sqrt{1-\frac{v^2}{c^2}}}$
- β : $\frac{v}{c}$

At high energies, radiative processes become more significant than the ionisation processes for all charged particles. This *critical energy* is much higher for protons than it is for μ^+/μ^- or π^+/π^- in which the radiative processes start to occur at several hundred GeV. For PVT, which has a $Z_{Eff} = 4.67$ [43], the energy at which the radiative and ionization processes are equal is around 1000GeV [21]. The mean excitation energy of PVT is 64.7eV [44].

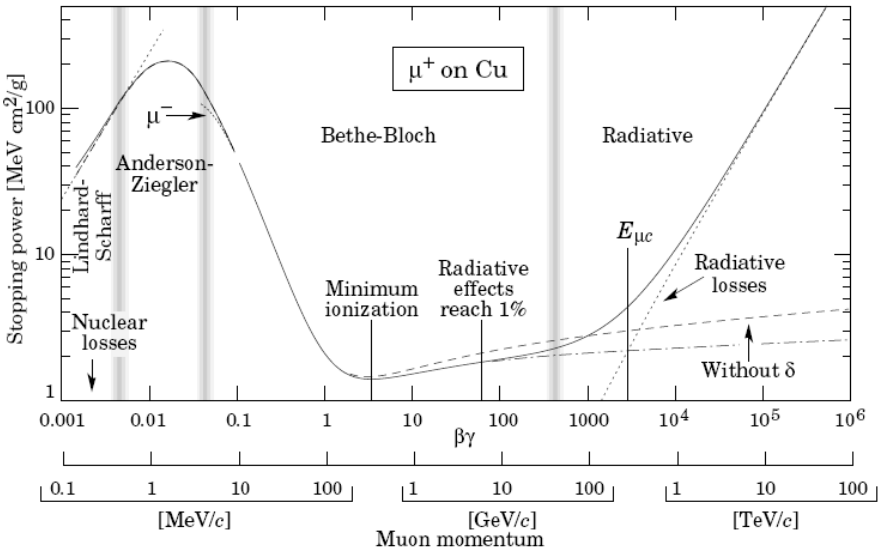

Figure 4.3: A plot of the results of Bethe-Bloche equation for μ^+/μ^- in Copper.

4.2 Expected Fluences in the BSC Tiles

The majority of incident particles on the scintillator tiles will be protons. The hadron flux throughout the CMS cavern has been simulated [54] using GEANT4 and the graphical results are shown in figure 4.4. These results give an approximate rate at which the BSC system will be expected to operate and are based on the LHC full luminosity of $\mathcal{L} = 10^{32}$ protons per bunch. These rates are shown in table 4.1 and graphically in figure 4.4. The inner most tiles of the BSC1 on the front face of the Hadron Forward (HF) calorimeter (z = $\pm$ 10.91m) and the BSC2 tiles (z = $\pm$ 13.36m) will experience an estimated flux of 1×10^9 hadronic particles per square centimeter per second. The outer BSC1 tiles will experience an estimated flux of 1×10^8 hadronic particles per square centimeter per second.

Although the hadronic flux will be much greater than the halo muon flux,

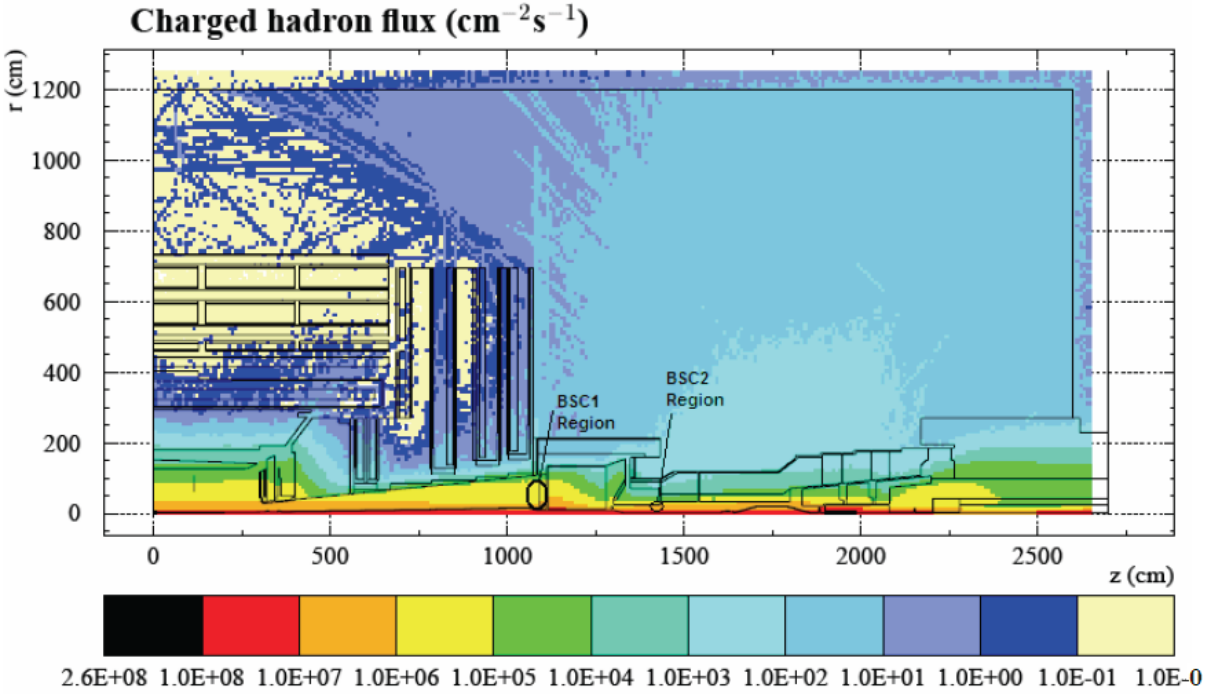

Figure 4.4: The simulation results of the expected hadron flux in CMS at full LHC luminosity of $\mathcal{L} = 10^{32}$. The figure shows the cross section of CMS along the beam line ($x = 0$) [54].

Tile Name	Tile Area	Luminosity				
		10^{27}	10^{30}	10^{32}	10^{33}	10^{34}
Paddle Tile		Rates s^{-1}				
Large Section	$823cm^2$	82	8.23×10^4	8.23×10^6	8.23×10^7	8.23×10^8
Small Section	$548cm^2$	55	5.48×10^4	5.48×10^6	5.48×10^7	5.48×10^8
Annular Segment	$489cm^2$	490	4.89×10^5	4.89×10^7	4.89×10^8	4.89×10^9

Table 4.1: Hadron fluxes through each of the BSC tile subsections [56].

Halo Muon Rate on Forward Calorimeter	16477 $\pm$231s^{-1}
Active Area of Forward Calorimeter	28350 cm^2
Halo Muon Flux at Forward Calorimeter Region	16477/28350 = 0.58$cm^{-2}s^{-1}$
Active Area of Annular Ring Segment	489cm^2
Halo Muon Rate on One Annulus Channel of BSC	284 $s^{-1}\pm4s^{-1}$
Halo Muon Rate on Entire BSC1 Area (1.2m^2)	6960 $s^{-1}\pm64s^{-1}$

Table 4.2: Extrapolation of the HF halo muon flux to the active area of the BSC1. Halo muon rates on the forward calorimeter were taken from simulations[22].

the latter have the ability to penetrate through the entire CMS detector and induce signals in to both $+z$ and -z BSC tile assemblies. Simulations of the muon flux on various sub-detectors in the CMS experiment have been carried out[22] based on the full luminosity of $10^{34}cm^{-2}s^{-1}$. The most relevant detector for the BSC in this study was the Hadron Forward Calorimeter (HF) as it is the front face of this detector that the BSC is mounted on to. The results for the HF muon flux have been extrapolated to estimate the flux through the active area of the BSC1 tiles. Table 4.2 shows these calculations. The estimated halo muon rate in the BSC1 tiles at full luminosity is of the order of 300 particles per second.

There are several plans of how the LHC commissioning will take place, each differing in time scale and luminosity of injection. Experience from

accelerators such as DESY and Tevetron suggests that full luminosity will take several months or even years to achieve. Based on the results shown in figure 4.4, the BSC front end hardware will not be able to cope with the hadron hit rates when the LHC reaches 10^{32} luminosity. This is due to the combined effects of the scintillator signal decay times and the maximum output rate of the PM tubes.

4.3 Radiation Damage to PVT Scintillators

Radiation damage in PVT causes the production of C-H bond breaks, dehydrogenation and free radical formation which permanently damages the polymer structure and reduces the luminescence yield significantly. The residual polymer contains more and more carbon with the irradiation dose. Generally, a dose of 10^{14} ions/cm^2 of 100 keV helium beam produces a black color of the polymer. In terms of the absorbed dose this value corresponds to about 10 MGy [28]. The radiation damage effect increases with the stopping power of the incident particle and produces a decrease in luminescence. For example, for 60MeV proton irradiation (stopping power 1.1 keV/mm), this reduction is about 15% at a dose of 1 kGy [28].

The particles of interest to the BSC are minimum ionizing particles (MIPs) and have a much lower stopping power and hence cause less damage to the plastic's polymer structure. Even so, the BSC scintillator tiles are expected to have a lifetime of just 12 to 18 months, depending on the time line of the LHC commissioning and bunch filling schemes. This life span is adequate as the BSC is intended for use during the commissioning stages

when the LHC will be running at low luminosity. It should be noted that the efficiency of the BSC will degrade over this time and calibration corrections may need to be made during operation on the measured hit rates of the inner most tiles which will experience the highest radiation exposure and therefore be damaged most rapidly.

Chapter 5

Beam Scintillator Counter Mechanics

The purpose of the BSC as a commissioning and safety device established the design philosophy of the system. The main requirement was that the hardware used must be simple and well tested rather than constructing novel electronics with unknown long term characteristics and a difficult commissioning phase. With the hardware for high energy physics experiments being notoriously expensive, finance was also an issue. Fortunately, most of the front-end hardware for the BSC was available from a previous CERN experiment called OPAL [20] which ran at LEP prior to the construction of the LHC. Due to the prior usage of the front-end hardware, rigorous testing needed to be carried out to determine the extent of any radiation damage or natural aging. This chapter explains each of the front-end hardware components.

	Scintillator	WLS fibre
Material	Polyvinyltoluene (BC408)	Polystyrene & PMMA
Peak Wavelength	425nm	495nm
FWHM	2.5ns	12ns (with BC408)
Attenuation Length	210cm	225cm
Refractive Index	1.58	1.42 – 1.49
Density	$1.032 g/cm^3$	

Table 5.1: Characteristic properties of the scintillator and WLS fibres.

5.1 Scintillator Tiles

The Beam Scintillation Counter uses scintillators tiles made from 13mm thick polyvinyl-toluene (BICRON BC408 [46]). Embedded within the plastic are wavelength shifting fibres (Kuraray Y11-200 non-S[27] and Bicron BCF91A MC[47]). Figures 5.1, 5.2 and 5.3 show the interior and dimensions of these tiles with the embedded wavelength shifting fibres coiled inside. Table 5.1 gives some of the core material and optical properties of the scintillator tiles. Note that the long paddle tiles contain two separate plastic tiles with their own embedded wavelength shifting fibres (WLS fibres). The annular tiles contain 4 equal sized segments of scintillator, again with the WLS fibres. Each segment has two output connectors from which the light captured by the embedded WLS fibres is emitted. Each connector requires four optical fibres and, together, take the light signal to a photomultiplier tube. The tile segments also contain an ultraviolet light emitting diode (LED) which is used to test and calibrate the front-end system.

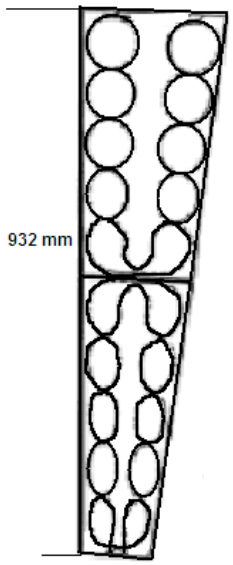

Figure 5.1: Interior of the long paddle scintillation tile.

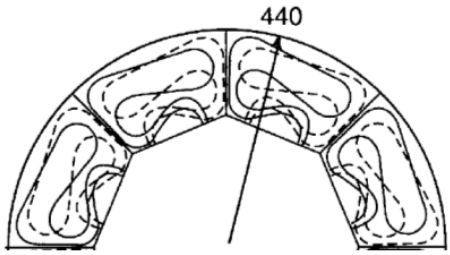

Figure 5.2: Interior of the inner annular disk scintillation tile.

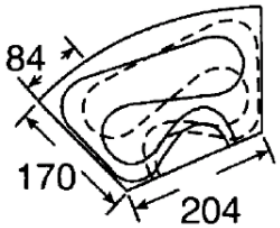

Figure 5.3: Interior of the BSC2 scintillation tile.

5.1.1 Timing analysis & Geometrical Layout of Scintillators

The position along the z axis and orientation of the scintillation tiles is an important factor as it affects the ability to discern between the signals generated by incoming and outgoing particles. The nominal bunch spacing of the LHC is 7.5 m with bunches 25 ns apart. With bunches traveling in opposite directions, a standing wave pattern is set up with the nodes evenly spaced by 3.75 m. At these nodes, it is impossible to distinguish between the incoming background particles and the outgoing collision products plus background as all the particles arrive at the detector at the same time. The midway point between these nodes gives the greatest Δt between the incoming and outgoing particle bunches. Δt can be calculated using equation 5.1.

$$\Delta t(z) = min|\frac{2z}{c} - nB|, \quad n = 0, 1, 2... \tag{5.1}$$

Here, z is the distance along z from the I.P, c is the speed of light and B is the bunch spacing in nanoseconds.

Tables 5.2 and 5.3 give some of the optimum z and poor z positions for the detectors with regards to timing of the incoming and outgoing particles.

By the time it was decided to include the BSC project into the BRM system for CMS, space within the CMS detector was very limited. It was

75ns bunch spacing	25ns bunch spacing
5.625m	1.875m
16.875m	5.625m
28.125m	9.375m
39.375m	13.125m

Table 5.2: The optimum z axis detector positions for maximum Δt of incoming and outgoing particles for 75ns and 25ns bunch spacing.

75ns bunch spacing	25ns bunch spacing
11.250m	3.750m
22.500m	7.500m
33.750m	11.250m
45.000m	15.000m

Table 5.3: The z axis detector positions for zero Δt of incoming and outgoing particles for 75ns and 25ns bunch spacing. These are the least favourable z positions for the BSC tiles. The BSC1 tiles are positioned at 10.91m; close to the node at 11.25m, due to the unavailability of space for the large tiles in more favourable positions.

therefore decided that the front face of the Hadron Forward (HF) calorimeter would be the best available position to put the BSC scintillators tiles. This position is 10.91m from the I.P giving a time difference of incoming and outgoing particles of 2.26 ns. Investigations into whether the BSC front-end hardware is capable of operating with this time resolution were carried out and are explained in chapter 9.

An extra set of small scintillation tiles, now known as the BSC2, were installed within the BCM2 structure, and mounted on the CASTOR table at a distance of 14.36 m from the interaction point (IP). This gives a time difference of 4.27 ns at the nominal 25 ns bunch spacing. More importantly, it allows for a Δt of 20.7ns during the engineering run of the LHC when

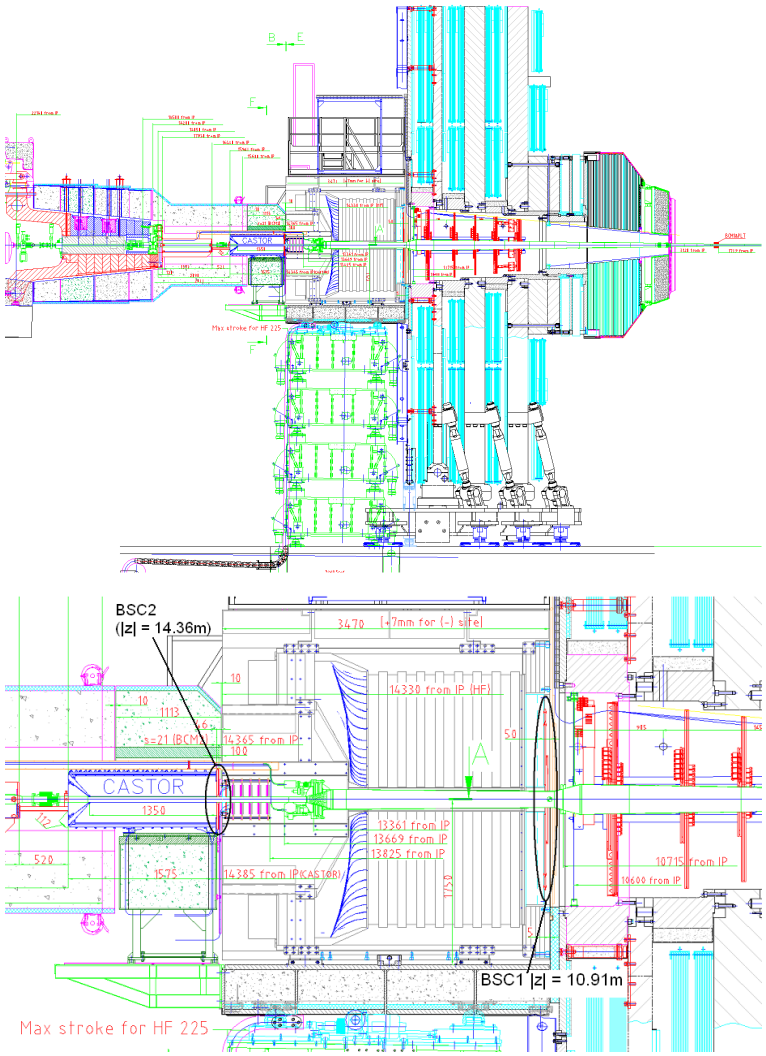

Figure 5.4: Cross section drawings of the CMS detector showing where the BSC1 and BSC2 detector tiles are located. These positions give a 2.26ns (BSC1) and 4.27ns (BSC2) Δt between incoming and outgoing particles.

bunches will be spaced 75ns apart. The position of the BSC1 tiles on HF gives the same Δt irrespective of whether bunches are spaced 25ns or 75ns apart.

Several designs for the layout of the BSC1 tiles were worked through. A compromise between a physically useful geometry of the tiles and the

	Distance from I.P	75ns bunch spacing	25ns bunch spacing
	± 10.91	2.26ns	2.26ns
	± 14.46m	20.7ns	4.27ns

Table 5.4: The Δt between the incoming background and outgoing particles+background for the locations of the BSC1 (z=±10.91m) and BSC2 (z=±14.36m).

Paddle Tile, Large Section	Paddle Tile, Small Section	Disk Tile Segment
823cm^2±20cm^2	548^2±20cm^2	489^2±5cm^2

Table 5.5: The active areas of each of the three tile segments use in the BSC.

mechanical constraints inherited from their position on the HF front face had to be made. The final design of the BSC1 tile layout is shown in figure 5.5 which also shows that radial distances from the beam-pipe center to the edges of the active area for the disk tiles and paddle tiles. The geometrical layout of the BSC1 tiles is shown in figure 6 and 7. The area covers approximately 1.2m^2 (1m^2 active area) of the HF front face and provides a pseudo-rapidity, η of $3.9 < 4.4$ based on the tiles which encompass the beam pipe. These tiles provide 8 channels per end of the BSC. To increase the radial coverage on the HF front face, four long tiles (1370cm^2 active area) will be placed diagonally as shown, to form an outer annulus. These tiles each consist of two separate sections, divided approximately midway. These four tiles constitute an additional 8 channels per end of the BSC.

The long paddle tiles contain two independent segments; one slightly broader than the other. Table 5.5 gives the active area of each of the tile segments.

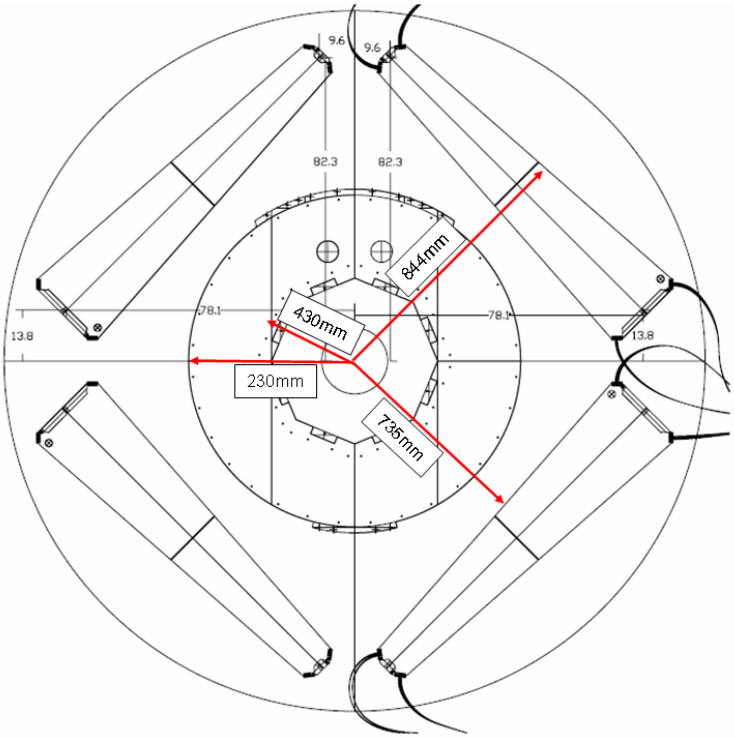

Figure 5.5: BSC1 Final Tile Layout on the Front Face of HF with indications of the paddle tile and disk tile radial dimensions.

Although it does not provide the ideal geometry*, this design was chosen as none of the tiles cross the center of the HF calorimeter. This is important due to the proximity of the delicate beryllium beam pipe once the HF calorimeter is opened. This layout was also the most symmetric of all the designs considered. This will make particle flux calculations easier as the symmetry around x and y does away with the need for correction requirements due to tile area differences. This greatly simplifies the interpretation of the rate monitoring.

5.2 Optical Fibres

Plastic (PMMA) optical fibres were used to transport the scintillation signal from the tiles to the photomultiplier tubes (PM tube). Eight optical fibres are required for each scintillator segment. These eight fibres go to a single light plug which is optically bonded to the window of a PM tube. Although these optical fibres are not as fragile as glass fibres, attention to the minimum bending radius must be considered when designing routing paths for the fibres from the scintillator tiles to the PMT boxes. The diameter of the active area of the fibres is 1mm. A 10% light loss can be expected for a bending radius of 60 times the diameter of the fibre. i.e. a bending radius of 60mm would result in a 10% light loss from the fibres. Throughout the design of the BSC mechanics, the minimum bending radius was limited to 80mm.

The BSC1 fibres had to exit the face of the HF calorimeter and traverse the outer steel rim in order to reach the PMT boxes. Two pair of grooves

* A layout with the long panels being radial to the central beam pipe would give a more convenient geometry. However, the panels were too long to fit within the HF inner radius.

were cut into the HF steel rim as shown in figure 5.6. Cherenkov radiation, in the form of visible light is produced when a charged particle passes through a medium with a velocity greater than that of light in the medium. Cherenkov radiation can be induced into PMMA fibres [2] by charged particles as they pass through. This light contributes to the background noise of the detector and must be prevented as much as possible. Each BSC tile segment uses two sets of four optical fibres to transfer the scintillator light to the PM tubes. A stream of charged particles passing through a majority of these fibres would produce a larger signal than if they had passed through only a few fibres.

Figure 5.6: Photograph showing the two pairs of grooves cut into the HF outer steel rims to allow the exit of the BSC1 optical fibres. The grooves were positioned in a way to reduce Cherenkov radiation in the optical fibres and do not allow a direct line of sight to the beam pipe from the outside.

The two grooves in each HF rim allow the eight optical fibres from each tile segment to be kept separated by several centimeters until they reach the relatively low radiation area outside the HF envelope, thus reducing the

possibility of a single stream of particles producing Cherenkov light in all 8 fibres. The grooves were also cut horizontally to reduce the effects of particle jets which are frequently emitted radially from the I.P.

The refractive index of PMMA is approximately n = 1.49. A difference in length of the optical fibres from the tiles causes a spread in the arrival times of the signals at the PM tubes. For example, a length of 1m between two sets of fibres will result in a time difference of nearly 5ns of the light signals at the windows of the PM tubes. This could be avoided by ensuring all the fibres are the same length. However, it is much easier to implement a time offset of each channel individually in software using the single bunch filling scheme of the LHC to induce a scintillator signal in all $+z$ and $-z$ BSC1 tiles simultaneously.

5.3 Photomultiplier Tubes

The PM tubes are Thorn EMI* 9902KA 10 dynode tubes with a 32mm diameter active area with a green light sensitive bialkali photo cathode [18]. These tubes have been selected for their uniform sensitivity across their optical window. The operating voltage of new tubes is documented as -750 to -900v.

Photocathode materials are required to have very low work functions to ensure they have a good sensitivity. However, due to this characteristic, they are able to emit thermionic electrons even at room temperature. Most dark currents originate from the thermionic emissions, especially those from

* Now manufactured by Electron Tubes Ltd.

the photocathode as they are multiplied by the dynodes. Cooling the photocathode can drastically reduce the levels of thermionic emission and is particularly useful in applications where very low dark current is required, such as photon counting.

Thermionic emission increases with operating voltage. A low operating voltage will result in low thermionic noise from the tube but will also give a poor spectrum of signal amplitudes. Increasing the operating voltage will produce a more useful output from the tube. The signal amplitude will be greater and the output amplitude will be a function of the quantity of incident photons, thus allowing the discrimination between high energy particle hits and low energy depositing MIPs. The increased operating voltage will also produce a higher dark current from thermionic emission and this has to be considered when designing the readout system and choosing the PM tube operating voltages.

Aging of the tubes will increase this operating voltage slightly and tests were conducted to find their optimum operating voltage as well as characterize their signal amplitudes, fall-times and pulse widths. These tests are described in chapter 7.

The PM tubes will be housed in Aluminum alloy boxes (see figure 5.7)in the upper corners of the HF calorimeters. These boxes protect the PM tubes and act as Faraday cages suppressing the noise pickup by the signal lines. These boxes are grounded to the UXC by braided earthing cables. However, the PM tubes inside are isolated from the box by halogen free plastic brackets.

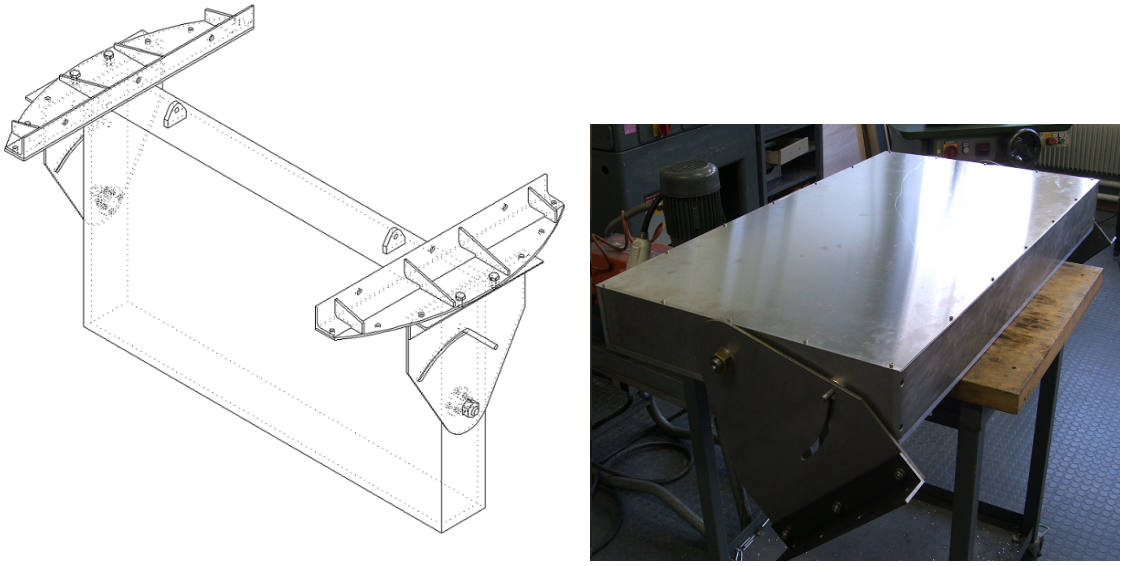

Figure 5.7: PM Tube box CAD design (left) and the completed box (right).

5.4 High Voltage Cabling & Routing

Two CAEN A1535N [10] negative high voltage power supplies were installed into the S1 control room in the USC* at an approximate distance of 70 m. The high voltage was delivered to the UXC arriving at the far side ($+x$) side of the HF calorimeters. The high voltage cable used was a 56 core steel braided cable capable of handling 3kV. In order to supply the PM tubes on the near side of the HF calorimeters, the cable was first sent to a splitter box (figure 5.8) and high voltage channels for each side were taken to their corresponding PM tube.

* Underground Service Cavern.

Figure 5.8: Photo of the high voltage splitter box with the 23 pin Radiall connector. The box will be mounted under the HF platform.

5.4.1 High Voltage Connectors

The BSC scintillator tiles are only expected to function for 18 - 24 months and so the need for radiation hard high voltage connectors was not vitally important. The A1535N power supplies use Radiall high voltage output connectors so it was decided to use these connectors throughout the BSC high voltage design (figure 5.10. Figure 5.9 shows the layout of the high voltage wiring and the connectors used.

The A1535N[10] supplies are controlled via the CAEN SY1527[11] crate controller. Each BSC channel, consisting of a scintillator tile/ PM tube pair, was assigned to a specific output channel from the A1535N supplies and control software for the SY1527 was written to accommodate this hardware mapping. Figure 5.11 shows the mapping of the high voltage channels from the A1535N power supply, through the Radiall connectors and high voltage cables, splitter box and finally to the PM tubes.

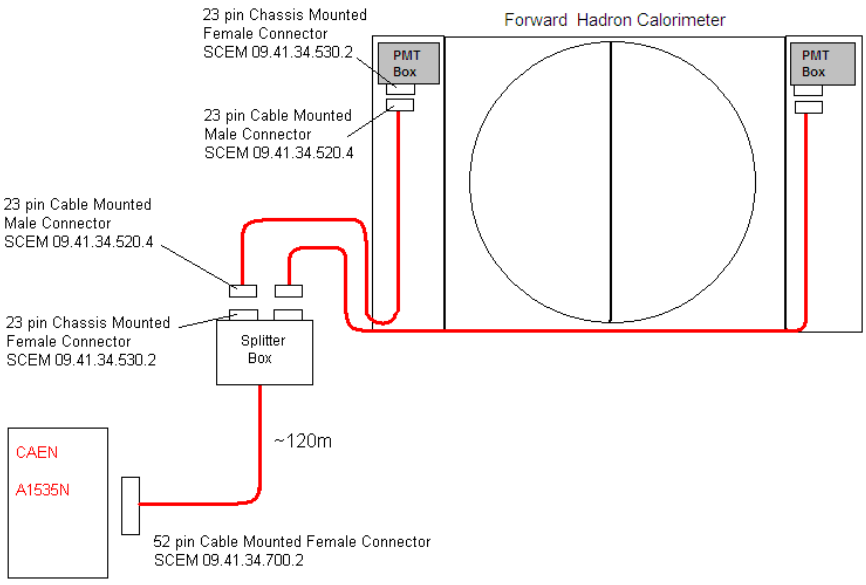

Figure 5.9: Diagram of the BSC high voltage wiring and connectors. The $+z$ and $-z$ systems are identical.

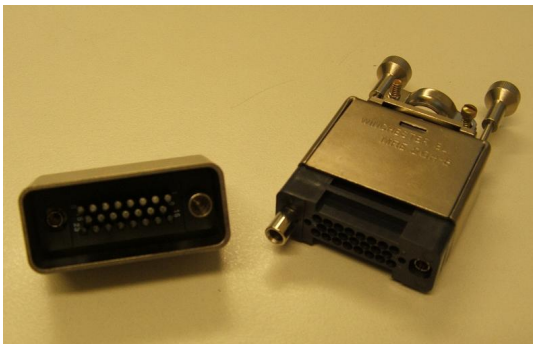

Figure 5.10: Photograph of the Radiall HV connectors used throughout the BSC.

The power supply output channels were chosen such that the connections for the $+x$ and $-x$ channels would be easy to connect and kept separate from one another. The HV cable cores were chosen to match the Radiall connector pin assignments, simplifying the task of installing the connectors.

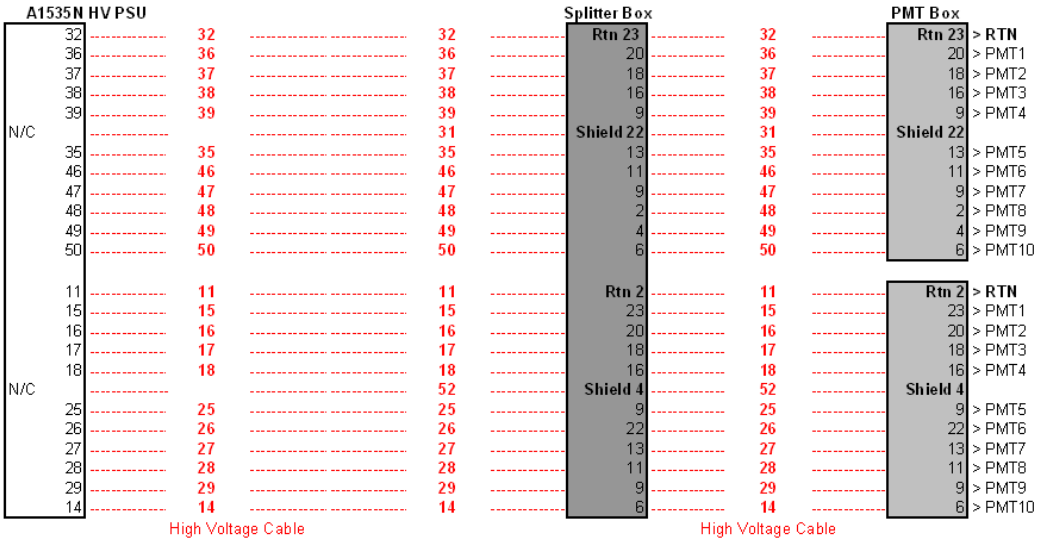

Figure 5.11: Diagram of the BSC high voltage hardware channel mapping. The channels from the A1535N power supply have been mapped to specific BSC tile/PM tubes so each can be controlled independently.

5.5 Nitrogen Gas System

As mentioned in chapter 1, the LHC magnets operate at a temperature of 1.9K, cooled by liquid helium. If any of the magnets close to the CMS cavern were to quench, millions of cubic meters of Helium gas would flow in to the CMS cavern. Helium gas can diffuse through the optical window of the PM tubes. Here it can react with the photocathode material, reducing its quantum efficiency. To protect the PM tubes from such a scenario, the PMT boxes will be flooded with Nitrogen gas. This gas will act to displace the majority of the Helium that would otherwise have filled the boxes and damaged the tubes. The details of the mechanical designs of the gas flow system are still ongoing. However, a supply of Nitrogen from the HF calorimeter group has been negotiated and gas flow valves will be installed

on to the gas distribution panels. The PMT boxes will be made almost leak proof to prevent excessive use of the Nitrogen gas. A nominal flow rate of <4 litres per hour should be sufficient to supply two PMT boxes on either end of the experiment.

5.6 Embedded LED Driver

Each of the 34 tile segments of the BSC1 and BSC2 incorporate embedded ultraviolet LEDs within the scintillator plastic with connection terminals situated on the edges near the optical fibre connectors. These LEDs will be used to check the basic connectivity of each of the BSC channels and also help to tune the channels to provide an equal amplitude response. The LEDs will be driven using a standard pulse generator connected to a dedicated RG58 signal cable. This cable will enter the PMT box and connect to the LED fan out board shown in figure 5.12. This board takes the pulse waveform (>2v) from the RG58 cable and supplies up to 10 LEDs connected to the small white connectors with halogen free twisted pair wires. These wires follow the optical fibres out of the PMT box to the front face of the HF calorimeter and plug in to the LED connectors on the tile segments using 0.8mm diameter, 2mm pitch headers.

The LED board has been tested and using a Phillips pulse generator, 9 LEDs can be driven via a 70m length of RG58 coaxial cable.

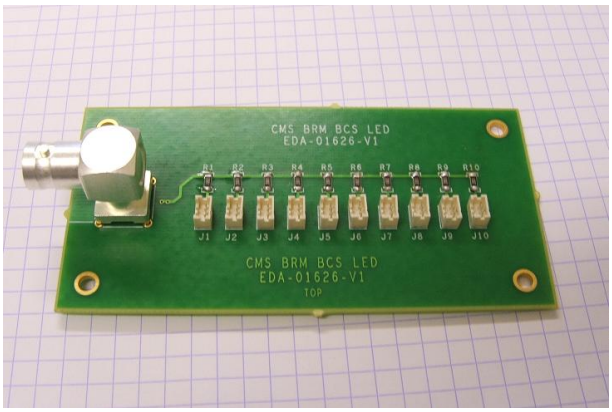

Figure 5.12: A photo of one of the LED fan out board which will be situated inside each of the four PMT boxes. Each board can be connected to all 9 channels of each quadrant of the BSC to test for connectivity problems and help set up PMT bias voltages for uniform gains.

Chapter 6

High Voltage Supply & Grounding

There are two A1535N power supplies used for powering the 4 banks of PM tubes of the BSC; one for each end of the CMS detector ($+z$ and $-z$). Certain features, such as current trip threshold and voltage ramp-up/ramp-down rates can be set through software. Table 6.1 shows the specifications of the programmable settings of the A1535N supplies for the BSC.

The output channels have been chosen in a way that separates the $+x$ and $-x$ sides so that the cores of the HV cables can easily be split to go to their physical destinations.

The physical mapping of the channels for both power supplies is the same. Only the logical mapping, i.e. the naming of the channels in software is different. The naming scheme describes the tile location for which each HV channel corresponds to. This way if the tile of one channel of the BSC is registering excessive hits but the channel of a neighboring tile is not, the

Nominal Voltage	$1400 - 1800V$
Maximum Voltage Limit	$2000V$
Ramp-Up Rate	$50V/s$
Ramp-Down Rate	$100V/s$
Nominal Current I_{nom}	$200\mu A$
Over Current Warning I_{warn}	$250\mu A$
Current Kill I_{kill}	$350\mu A$

Table 6.1: Thresholds for currents and voltages from the CAEN A1535N power supply.

high voltage can be adjusted in an intuitive way to compensate.

Figure 6.1 shows the output pins from the Radiall connector on the A1535N chosen to facilitate the wiring in such a way that the $+x$ and $-x$ channels are kept separate, an important consideration when the connector installation has to be performed in the cramped conditions under the HF calorimeters. Figure 6.2 gives the positions of the tiles on the HF front face and the BSC2 tiles situated behind HF. Table 6.2 lists the channel names allocated to these channels. Channels 36 - 39 and 46 - 50 go to the $-x$ side PM tubes. Channels 15 - 18 and 25 - 29 go to the $+x$ side PM tubes.

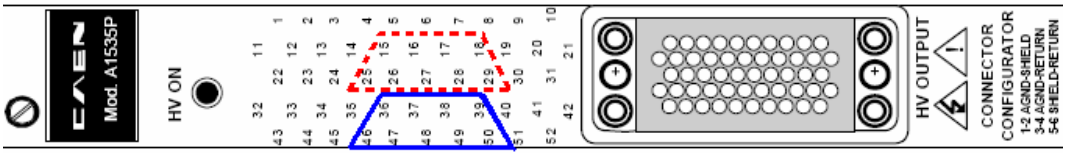

Figure 6.1: The Radiall output socket of the A1535N power supply. The blue line (solid) encompasses the -X side channels. The red line (dashed) encompasses the -X side channels. This output scheme is the same for +Z and -Z supplies.

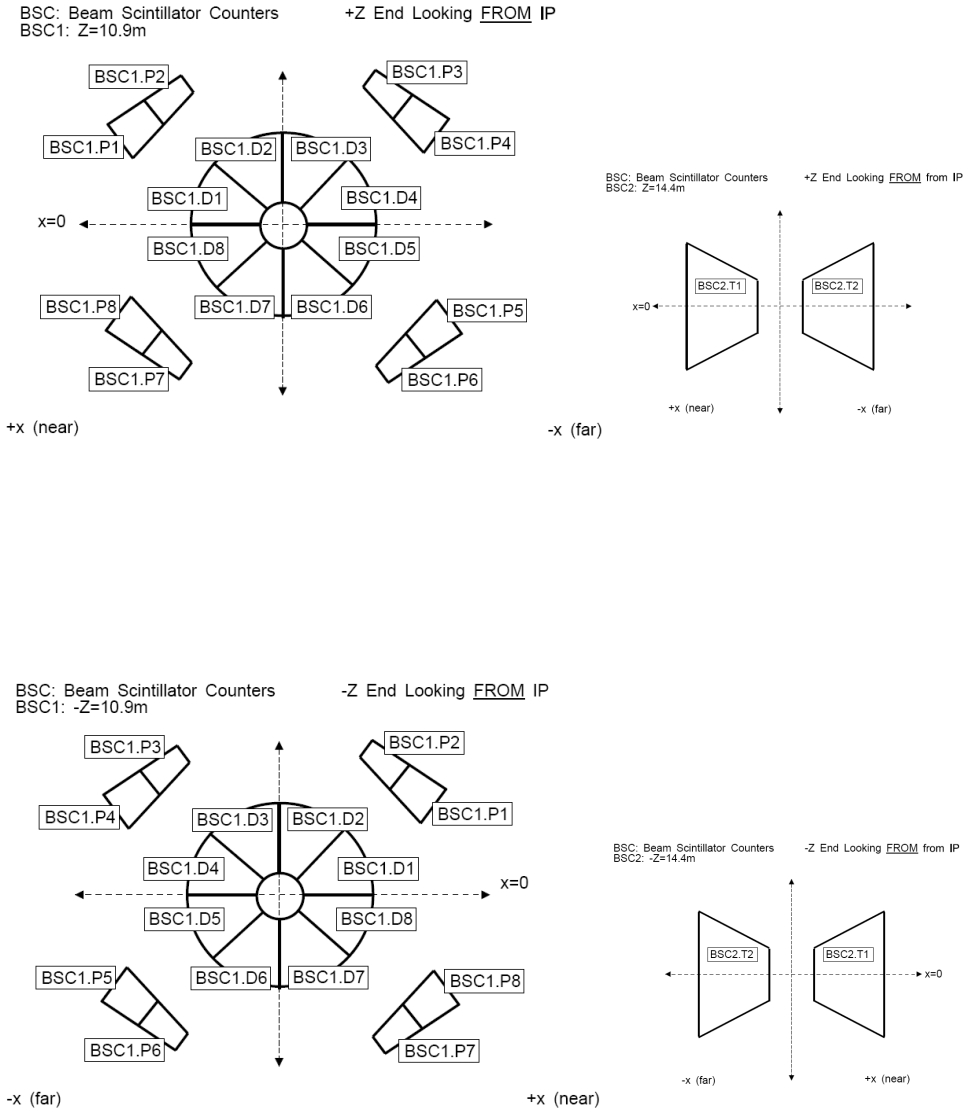

Figure 6.2: The BSC1 tile layout on the HF front face (left) and the BSC2 tiles. The numbers correspond to the naming convention explained in the text. Both *+Z* and *-Z* ends are shown viewed as looking away from the I.P. Table 6.2 lists the channel names that will be used in the HV control software of the SY1527 crate that houses the A1535N power supplies.

High Voltage Channel Mapping

To control the A1535N channels via the SY1527 crate and software requires a intuitive nomenclature to identify the tiles. These names must also follow the BRM group convention of having the prefix CMS_BRM_*sub-dectector name*. The names should give some indication of the position of the tile which the channel influences. The scheme chosen is as follows:

CMS_BRM_[BSC**1 or BSC2**][**Near or Far**][**Tile Type**][**Tile No.**]

Where tile type is signified by P (Paddle), D (Disk) or T (Tile). Table 6.2 lists the tile names for each quadrant of the BSC.

During testing of the front-end hardware, each tile has been paired with a particular PM tube. The channels of the CAEN power supply must go to a known PM tube and thus control the signal amplitudes of a known tile of the BSC1 or BSC2. Table 6.3 shows a list of tile numbers, PM tube numbers, their default voltage settings and their logical mapping names. All voltages listed in table 6.3 are negative and each channel is set with a ramp up rate of 50V/s. From the information in this table and that of table 6.1 all the software variables for the BSC high voltage system are known.

6.1 BSC Grounding

During the design process of a detector system, it is extremely difficult to simulate the noise problems that will be encountered when normal operation begins. The CMS detector has many channels which work with very low signal amplitudes and are connected to their readout electronics

Scintillator Tile No.	Logical Tree Name
(+Z,+X) Side	D = disk, P = Paddle, T = Tile
	CMS_BRM_1NBSC1.D1
	CMS_BRM_1NBSC1.D2
	CMS_BRM_1NBSC1.D7
	CMS_BRM_1NBSC1.D8
	CMS_BRM_1NBSC1.P1
	CMS_BRM_1NBSC1.D2
	CMS_BRM_1NBSC1.D7
	CMS_BRM_1NBSC1.D8
	CMS_BRM_1NBSC2.T1
(+Z,-X) Side	
	CMS_BRM_1FBSC1.D3
	CMS_BRM_1FBSC1.D4
	CMS_BRM_1FBSC1.D5
	CMS_BRM_1FBSC1.D6
	CMS_BRM_1FBSC1.P3
	CMS_BRM_1FBSC1.P4
	CMS_BRM_1FBSC1.P5
	CMS_BRM_1FBSC1.P6
	CMS_BRM_1FBSC2.T2
(-Z,+X) Side	
	CMS_BRM_2NBSC1.D1
	CMS_BRM_2NBSC1.D2
	CMS_BRM_2NBSC1.D7
	CMS_BRM_2NBSC1.D8
	CMS_BRM_2NBSC1.P2
	CMS_BRM_2NBSC1.P1
	CMS_BRM_2NBSC1.P7
	CMS_BRM_2NBSC1.P8
	CMS_BRM_2NBSC2.T1
(-Z,-X) Side	
	CMS_BRM_2FBSC1.D3
	CMS_BRM_2FBSC1.D4
	CMS_BRM_2FBSC1.D5
	CMS_BRM_2FBSC1.D6
	CMS_BRM_2FBSC1.P3
	CMS_BRM_2FBSC1.P4
	CMS_BRM_2FBSC1.P5
	CMS_BRM_2FBSC1.P6
	CMS_BRM_2FBSC2.T2

Table 6.2: Names of the BSC1 and BSC2 tiles for the logical tree in the software control. *F* stands for *Far*, *N* stands for *NEAR*. 1 represents +Z and 2 represents -Z. D (Disk), P (Paddle) and T (BSC2 Tile) 6.2.

+Z	+X			
Map No.	Tile No.	PMT No.	$Voltage_{set}$	Logical Name
1	C5A	17217	1600v	CMS_BRM_1NBSC1.D2
2	C5B	17117	1560v	CMS_BRM_1NBSC1.D1
3	C5C	17106	1625v	CMS_BRM_1NBSC1.D8
4	C5D	17232	1550v	CMS_BRM_1NBSC1.D7
5	1S	17109	1610v	CMS_BRM_1NBSC1.P2
6	1L	17197	1570v	CMS_BRM_1NBSC1.P1
7	5L	17227	1570v	CMS_BRM_1NBSC1.P8
8	5S	17105	1590v	CMS_BRM_1NBSC1.P7
9	BSC2	17107	1600v	CMS_BRM_1NBSC2.T1
+Z	-X			
Map No.	Tile No.	PMT No.	$Voltage_{set}$	Logical Name
1	C6D	17119	1600v	CMS_BRM_1FBSC1.D3
2	C6C	17230	1500v	CMS_BRM_1FBSC1.D4
3	C6B	17231	1550v	CMS_BRM_1FBSC1.D5
4	C6A	17200	1500v	CMS_BRM_1FBSC1.D6
5	6S	17109	1500v	CMS_BRM_1FBSC1.P3
6	6L	17196	1600v	CMS_BRM_1FBSC1.P4
7	11L	33001	1550v	CMS_BRM_1FBSC1.P5
8	11S	17206	1550v	CMS_BRM_1FBSC1.P6
9	BSC2	17108	1500v	CMS_BRM_1FBSC2.T2
-Z	+X			
Map No.	Tile No.	PMT No.	$Voltage_{set}$	Logical Name
1	C1D	17209	1650v	CMS_BRM_1NBSC1.D2
2	C1C	17102	1500v	CMS_BRM_1NBSC1.D1
3	C1B	17065	1580v	CMS_BRM_1NBSC1.D8
4	C1A	17110	1600v	CMS_BRM_1NBSC1.D7
5	13S	17114	1600v	CMS_BRM_1NBSC1.P2
6	13L	33002	1600v	CMS_BRM_1NBSC1.P1
7	14L	17225	1580v	CMS_BRM_1NBSC1.P8
8	14S	17211	1600v	CMS_BRM_1NBSC1.P7
9	BSC2	17136	1500v	CMS_BRM_1NBSC2.T1
-Z	-X			
Map No.	Tile No.	PMT No.	$Voltage_{set}$	Logical Name
1	C3A	17121	1550v	CMS_BRM_1FBSC1.D3
2	C3B	17111	1600v	CMS_BRM_1FBSC1.D4
3	C3C	17118	1560v	CMS_BRM_1FBSC1.D5
4	C3D	17103	1500v	CMS_BRM_1FBSC1.D6
5	10S	17206	1700v	CMS_BRM_1FBSC1.P3
6	10L	17187	1600v	CMS_BRM_1FBSC1.P4
7	16L	17219	1500v	CMS_BRM_1FBSC1.P5
8	16S	17203	1600v	CMS_BRM_1FBSC1.P6
9	BSC2	17120	1700v	CMS_BRM_1FBSC2.T2

Table 6.3: BSC1 and BSC2 tile locations and PMT number allocations. The default PMT voltages (negative) and Logical tree names are also listed.

over cable lengths typically in the range of 20 - 140m. Sub-detectors are packed closely together and noise generated by one could easily effect the surrounding detectors' signal quality. The grounding and earthing of detector subsystems has to be carefully planned to prevent unacceptable levels of noise appearing in the signal chains or causing oscillations on the output of power supplies. However, the primary consideration is safety and earthing of metallic structures is a legal requirement.

This chapter outlines some of the rules and recommendations for the grounding and earthing schemes of detector sub-system electronics and explains the grounding scheme of the BSC detector.

6.1.1 Common Grounding Problems

Ground Currents & Loops

Many of the signal channels in CMS are transmitted to the counting rooms via optical cables instead of the more conventional twisted pair or coaxial cables. This Electromagnetic Compatibility (EMC) design requirement was imposed to try to reduce the noise problems seen at previous large scale experiments. Some sub-detectors, the BSC and BPTX for example, were not able to follow this recommendation due to the necessity to simplify their commissioning phases and following EMC practices became an very important factor.

One of the most common EMC problems in large scale experiments is the unintentional creation of large ground loops in the signal lines. In CMS, back-end readout electronics and computers are located in the S1 - S4

service caverns 70 - 100m away from the front-end electronics and the CMS detector. The BSC and the BPTX sub-detectors both use coaxial cables for transporting their signals to the BRM racks in the S1 area of the USC.

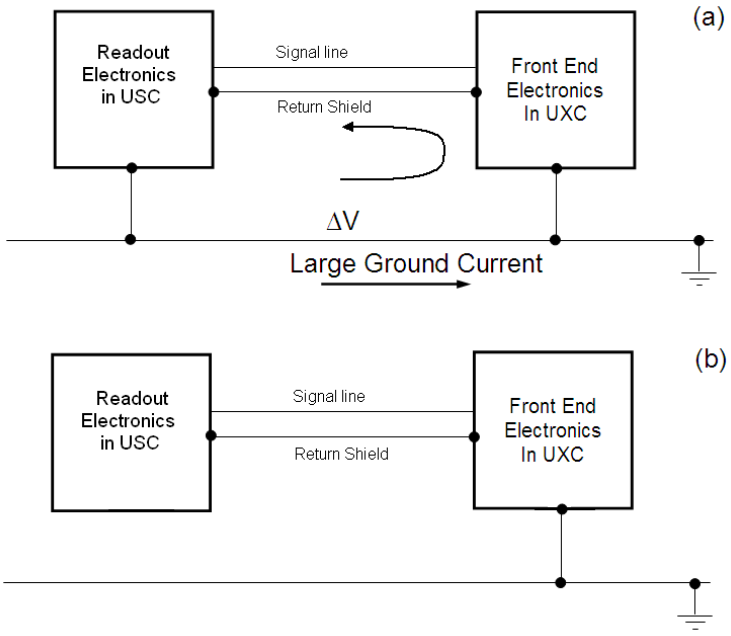

Figure 6.3: Grounding of the signal cables at both the detector and the readout end (a) may cause problematic ground currents which can be induced in to the signal conductor and appear as noise. The signal cable should only be connected at one end, usually near the detector (b) [23].

The 'ground' in the UXC cavern may not be at the same potential as the ground in the S1 counting room. Therefore, connection of the coaxial signal cable shields to ground at both ends would cause a noise current to flow through the ground and the shielding of the cables. This current can be induced in to the signal line and appear as noise.

Low voltage and high voltage power supplies also need to be carefully grounded in order to allow stable operation of the supplies. A power supply

Source	Frequency
LHC machine	
RF frequency	400.8 MHz
Bunch crossing rate	40MHz
Bunch groups $80 \times 25ns$	500kHz
Orbit 3654 bunches $\times 25ns$	10.9kHz
CMS	
FrontEnd & BackEnd electronics	40MHz & harmonics
L1 trigger	Approximately 100kHz
Power Supplies	
Mains	50Hz
Switching supplies	20kHz-500kHz
Wireless networks GSM	900/1800Mhz
Computer WiFi	2.4GHz

Table 6.4: A list of likely noise sources in the CMS experiment. The frequencies of these sources must be prevented or suppressed from entering the readout system [57].

line grounded at two or more points can cause variations in the ground voltage at the PSU sense point. The power supply module will try to compensate for these variations but is only capable of doing so up to a frequency limit, beyond which the power supply system will go in to oscillation.

6.1.2 CMS Noise Sources

With such a large amount of computers and electronics, as well as millions of violent particle collisions occurring every 25ns in the proximity of the readout systems, it is not surprising that many sources of electromagnetic noise exist. Preventing noise pick-up is the best option but this cannot always be achieved and noise suppression is required. Table 6.4 lists some of the noise sources along with their peak frequencies that need to be considered.

6.1.3 The BSC Grounding Design

As the BSC sub-detector uses coaxial cable for its signal transmission, care had to be taken so that ground loops were not created between the UXC and the S1 service cavern where the readout and power supplies are located. A simplified schematic of the BSC grounding scheme is shown in figure 6.4. The high voltage is supplied to the PM tubes which are located inside and isolated from the four metal boxes mounted on the HF calorimeters. These boxes protect the tubes and act as a Faraday cage. The A1535N power supply provides 24 channels with common floating return. The HV return is connected to the outer steel housing via the SHV connectors on the rear of the PM tubes. To comply with French electrical safety laws and to prevent noise pick-up by the PM tubes, the metal PMT boxes are grounded via the HF calorimeter bulk structure. The output signal is transported to the S1E09 rack in the S1 counting room via RG58 coaxial cables which are grounded at the readout end.

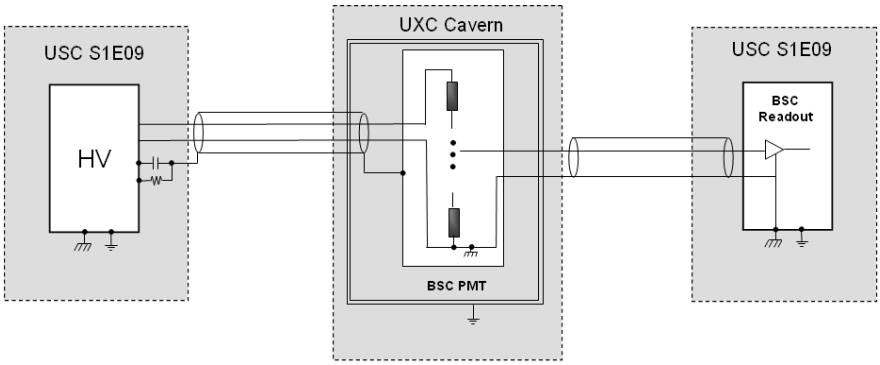

Figure 6.4: Simplified schematic diagram of the BSC grounding system. The front-end PM tubes are housed in, but isolated from an aluminum box which is grounded to the HF structure using grounding braid.

Except for the PMT boxes, there is no galvanic connection to the UXC ground through the power lines nor the signal cables. Some noise suppression filtering may be required once the LHC and CMS begin operation.

Chapter 7

Front-End Hardware Tests

The front-end hardware installation in the UXC meant that rigorous testing and characterization needed to be done prior to installation. Access to the photomultiplier tubes in particular will be impossible except during maintenance shut-downs. The PM tubes are required to operate within the fringe magnetic field of CMS, therefore the effects of an externally applied magnetic field needed to be understood. Also, due to the age and prior use of the PM tubes and scintillator tiles, each component of the front-end hardware needed to be tested to ensure its operation is as expected.

7.1 Testing the Basic Scintillator Tile Conditions

As the scintillator tiles had undergone previous use in LEP and had since been badly handled and stored, testing the tiles for scintillation output was necessary. This was done using a Strontium Sr-90 30MBq beta source

(0.546MeV) positioned such that the emitted betas passed through the width of each tile. The number of hits per minute were recorded for each tile subsection. During these investigations, it was found that some of the tiles suffered from light leaks that needed repair. This was also noted and subsequently these light leaks have been repaired. The measurements also provided information on the relative sensitivity of each tile so that tiles could be selected based on the most uniform sensitivity.

Experimental Set Up

A PM tube (Serial Number 17200) was set up with a supply voltage of -750v and connected via optical fibres to each tile segment in turn. The output was fed into a NIM discriminator with the threshold set at the minimum -30mV, then in to a counter. The background counts from cosmic muons were recorded before placing the Sr-90 source on the tile. The counter was reset to zero and allowed to count the β induced signals for 5 minutes. The average counts per minute minus the pre-recorded background counts were recorded.

Results

The results are shown in table 7.1. This information identified, to first order, the scintillator tiles with the most similar sensitivity. In addition, light leaks in to the tiles were located and marked to be repaired at a later stage. Based on this simple test, the tiles chosen for use in the BSC1 were Tiles 14, 1,16,5,2,6,13 and 11. Further tests on all the tiles was carried out to confirm these findings. Also, light leak repairs to all tiles, including those

that were not damaged, were done using 3M halogen-free black polyethylene tape*. PVC tape is not permitted for use near the stainless steel beam-pipe due to possibility of radiolysis, a chemical reaction of the PVC that leads to the formation of hydrochloric acid which in turn could cause serious corrosion to the stainless steel portions of the beam-pipe.

Tile No.	Large	Small	Total	Counts/Min	Repair Req'd?
8	443	430	873	174.6	N
14	517	397	914	182.6	Y
1	573	416	989	197.8	N
16	559	440	999	199.8	N
5	578	433	1011	202.2	N
2	540	520	1060	212.0	N
6	601	575	1176	235.2	N
13	616	560	1176	235.2	Y
11	650	532	1182	236.4	N
10	804	432	1236	247.2	N
17	688	695	1383	247.2	N
4	896	490	1386	276.6	Y
15	907	504	1411	282.2	Y
7	673	798	1471	294.2	N
12	1388	592	1980	396.0	Y

Table 7.1: Results of the basic tile testing using a Sr-90 source on the large and small sections of the paddle tiles (see figure 5.1). Tiles 14, 1,16,5,2,6,13 and 11 were chosen for use in the BSC1. Tile 17 was the primary reserve tile.

7.2 Tests of PM Tube Operation

A total of 36 channels are provided by the BSC1 and BSC2 scintillator tiles mounted around the forward hadron (HF) calorimeters. The PM tubes are

* Available from Radiospares. P/N 494-506.

set out in four groups of nine and housed in aluminum alloy boxes in the upper quadrants of the HF structures. Once *in situ* the PM tubes are not physically accessible until the LHC is shut down for the first phase of maintenance. The fundamental goal of the BSC is that it must be installed and operational on day 1 of the LHC operation. Hence, it is imperative that all hardware is checked rigorously prior to installation. The PM tube tests were done to show which tubes had deteriorated the most, find the maximum magnetic field in which they could operate and inspect the effects on the output signal for varying orientations of the externally applied magnetic field.

7.2.1 Basic PM tube operation

The first aim was to check the gain verses high voltage of each tube individually using the LED embedded within the tiles. As PM tubes age, a higher supply voltage is required to obtain a specified output signal amplitude. By providing a fixed intensity pulse of light from the LED, output vs. HV supply response curves for all the tubes were produced.

The tubes needed to be checked individually using the same set up for each. The PMT to be tested was connected to the HV power supply and its signal output connected directly to a digital oscilloscope (Tektronix 3032B). Optical fibres were connected to the PMT using a prefabricated loom identical to the ones used in the final assembly. A set of 4 wavelength shifting fibres were connected to the end of the optical fibre loom and a UV/Blue LED was placed in 1cm away under a light shielding cloth. Light captured from the LED by the wavelength shifting fibres was converted to 453nm light

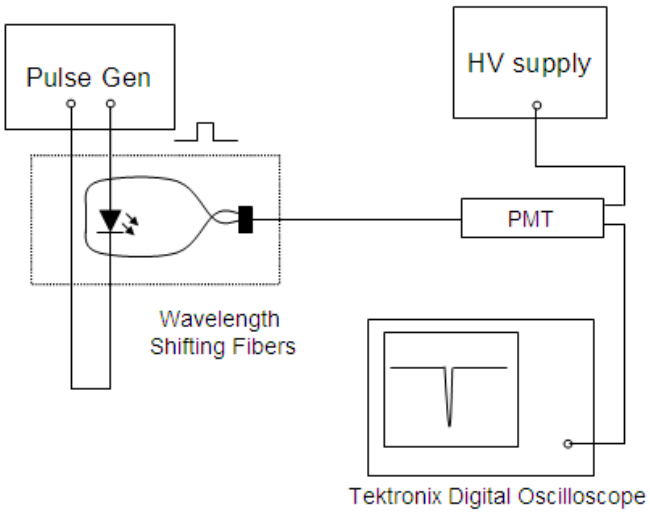

Figure 7.1: The experimental setup for the Gain vs. Supply voltage measurements. Averages of 100 amplitude measurements were taken from the oscilloscope and plotted again supply voltage for all 43 PM tubes.

to which the PM tube window is the most sensitive. The light then traveled down the PMMA optical fibre to the PM tube and the resulting signal trace could be seen on the oscilloscope.

The gain of the PM tube is a function of the high voltage supplied across the dynode chain. The EMI9902KA tubes have 10 dynodes. The gain can be calculated by

$$G = (KV_d)^n$$

where n is the number of dynodes, V_d is the high voltage supply across each dynode and K is a constant [60]. Figure 7.2 shows the results of one of the PM tubes tested alongside the calculated output curve. As can be seen, the measured response is close to the predicted response, proving that the PMT is in good working order.

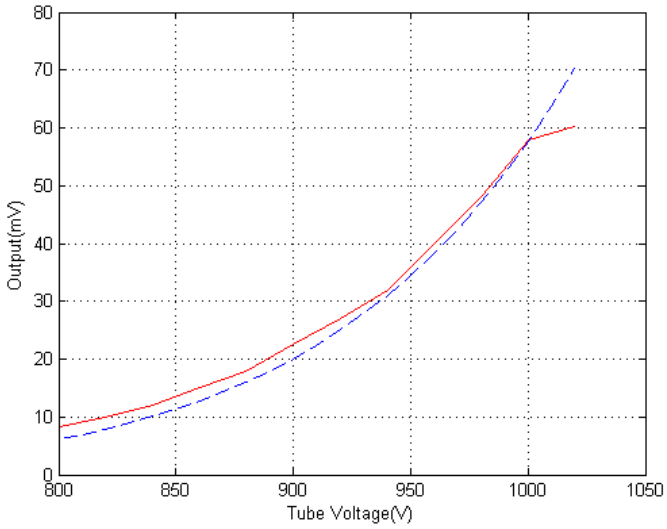

Figure 7.2: Example plot of a PMT Gain vs. HV supply curve. The red solid line shows the measured result. The blue dashed line shows the calculated result using a K value of 0.0018.

A complete set of curves for all the PM tubes is given in Appendix I.

The results showed that out of the available 43 PM tubes, only one tube was faulty. With this basic knowledge of the PM tube operation, further testing and characterization could be undertaken (see section 7.4).

7.2.2 Magnetic Field Tolerance Tests

The PM tubes used for the BSC front-end are Thorn 9902KA with 10 dynodes and a negative operational voltage. They have a 32mm diameter active area, with a green-sensitive bialkali photocathode. The dynodes are set out in a linear focused design. The manufacturers recommended operational voltage is -750v [18].

The tests described in this section were conducted to determine the

maximum magnetic field strength in which the PM tubes are able to operate with no appreciable signal reduction. When installed in to the CMS cavern, the PM tubes will be contained within a 10mm thick walled aluminum alloy box which will provide a small level of shielding from the fringe magnetic field. They will also be surrounded by a μ-shield, a laminated iron cylinder that deflects the magnetic field, shielding the PM tube inside from electromagnetic interference. However, it was not possible to place the large box between the poles of the test magnet. So the PM tube to be tested was done so with only the μ-metal shield attached.

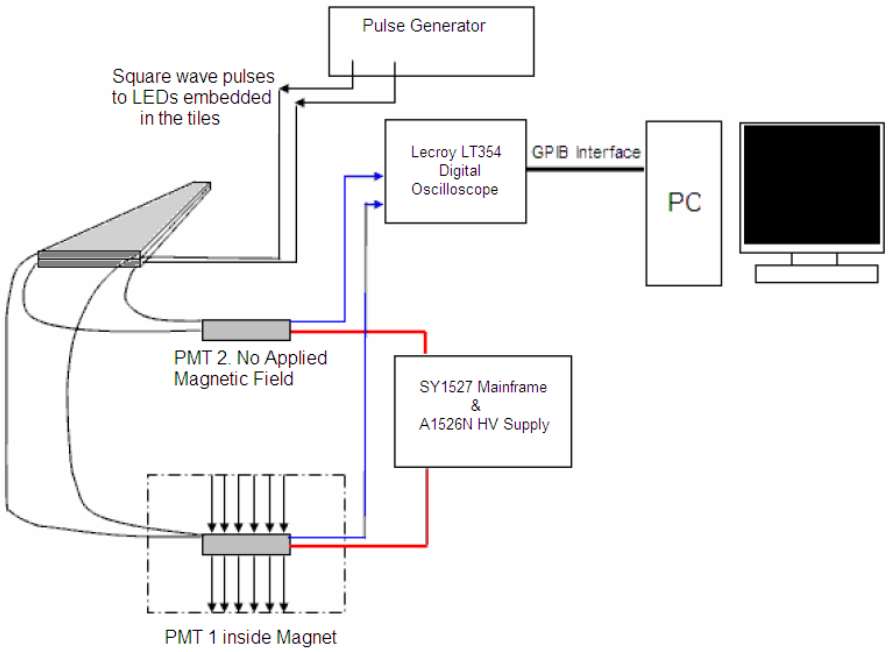

Figure 7.3: The experimental set up for the PMT Magnet tests conducted using the magnetic test facility at CERN.

The set up consisted of two scintillation tiles each containing a UV LED with external contacts. The embedded LEDs were pulsed simultaneously by the Pulse Generator. The LED light was captured by the internal wavelength

shifting fibres and sent to two PMTs, one of which was placed in a variable strength magnet with its central axis laid horizontal and perpendicular to the field and surrounded by a μ-shield. The second PMT was situated about 2 m from the magnetic field and acted as a reference to gauge long term stability and to determine if induced noise in the tube in the magnet was caused by the magnetic field itself or the surrounding high current power supplies. The Gauss meter measured no field at the position of this PMT at any of the field strengths used. It was assumed that any HV instability would be equal on both channels and that the embedded LEDs would behave similarly. The electrical signals from the PMTs were sent to a Lecroy digital oscilloscope with a GPIB interface card to communicate with the PC.

By adjustment of the HV and the pulse generator signal amplitude to the LEDs, the amplitude of the signals seen on the oscilloscope were equalized in the absence of any magnetic field. Measurements of the peak-peak amplitudes were made for various values of magnetic field ranging from zero (magnet off) to 1000 Gauss (0.1T). Fifty points were plotted per run. Each of these points represents the average of fifty RMS amplitude data acquisitions.

The results from each of the eight applied fields are shown in Appendix II. Figure 7.4 shows the relative outputs of the two PM tubes when an external magnetic field of 960 Gauss is applied to PMT 1. The red line represents the RMS signal averages from the PMT 1. The blue line is the data for PMT 2.

As can be seen from the graphs in Appendix II, the average RMS signal amplitudes from each PMT are initially almost equal (within 5mV) and remain so throughout the measurement run (approximately 8 minutes). The

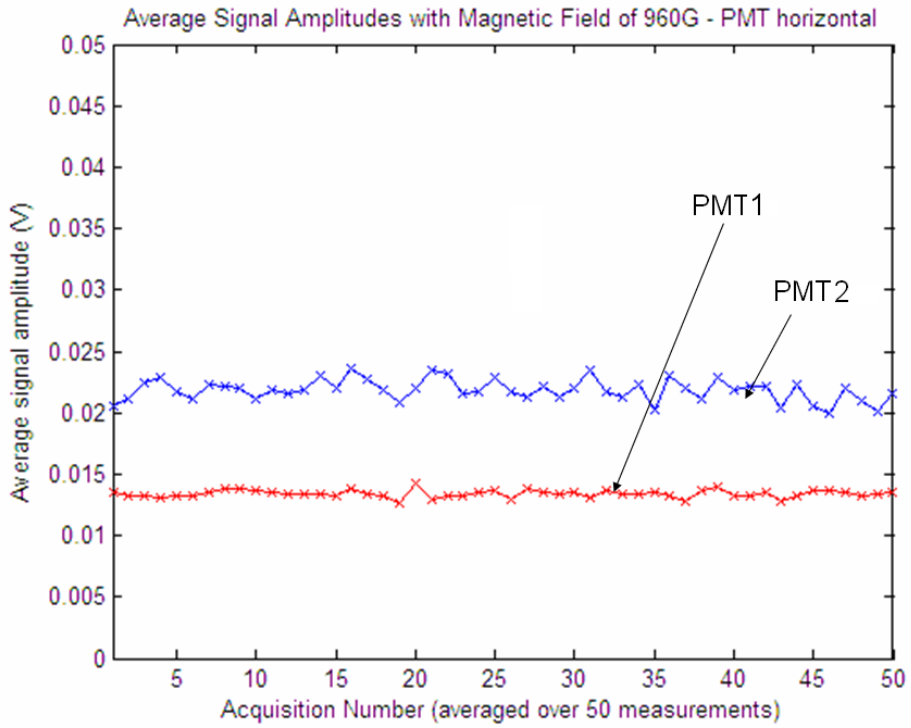

Figure 7.4: Average output amplitudes of the two PM tubes with PMT 1 (red line) being subject to a 960G external field applied perpendicular to its central axis. PMT 2 is not subject to the magnetic field

graphs show no sign of signal degradation until the externally applied field reaches 960G. Furthermore, at 1000G the signal from PMT 1 is completely lost. For all values of magnetic field, the HV current monitor remained constant at 214 μA @ -850V for PMT1 and 205 μA @ -815V for PMT2. RMS measurements of the noise also remained constant at around 0.5mV for the particular tube chosen) up until 900G when the signal and noise began to be suppressed by the magnetic field. It was noted that one of the tubes used for this test produced considerably more noise than the other. It is likely this noise can be blocked by the use of discriminators in the back-end readout. The data sheet for the 9902KB PMT (9902KA is the same tube

except that the photo-cathode's sensitivity is highly uniform) only states the magnetic sensitivity for this tube in its most sensitive orientation (parallel to the field) and with no μ-shield. The figure quoted is of 1.3×10^{-4}T (1.3 Gauss) for the signal output to fall by 50%. This figure could not be verified as the minimum field for the magnet used was approximately 100G. However, placing the tube in a 100G field with no μ-shield quickly eradicated the signal in any orientation other than the horizontal showing the obvious importance of using the μ-shields.

The results of these tests demonstrate that the PM tubes for the BSC are capable of operating in a magnetic field of <900G with no adverse effects on the signals, providing that μ-shielding is fitted and the orientation of the tube to the magnetic field is perpendicular. The expected magnetic field magnitude in the PM tube region is <200G[48]. With the angular adjustments built in to the PMT box mounting structure, explained in Chapter 5, and an adequate availability of μ-shields, no problems associated with the magnetic field are foreseen.

Magnetic Field Analysis of the PMT Region

Simulation models have been constructed to predict the magnetic field strengths and directions around the CMS solenoid. With the aid of these models, it was possible to map the magnetic field in tangential areas in the region of the HF calorimeter. The models are based on symmetry around x and do not include the effects of the platform structures which surround the HF calorimeters. However, these structures are not expected to have a large effect on the magnetic field.

A suitable region in the upper corners of the HF calorimeters, beneath the top platform structure has been located which places the PM tubes within a magnetic field of < 200G with a uniform direction with respect to the central PM tube axis. As seen in figure 7.5, the predicted field vectors, shown by the cones, rotate around the central axis of the PM tubes (depicted by the arrow), but remain perpendicular to it. This is important as the tubes were shown to be sensitive to magnetic fields which were incident on the central axis at angles less than 70°.

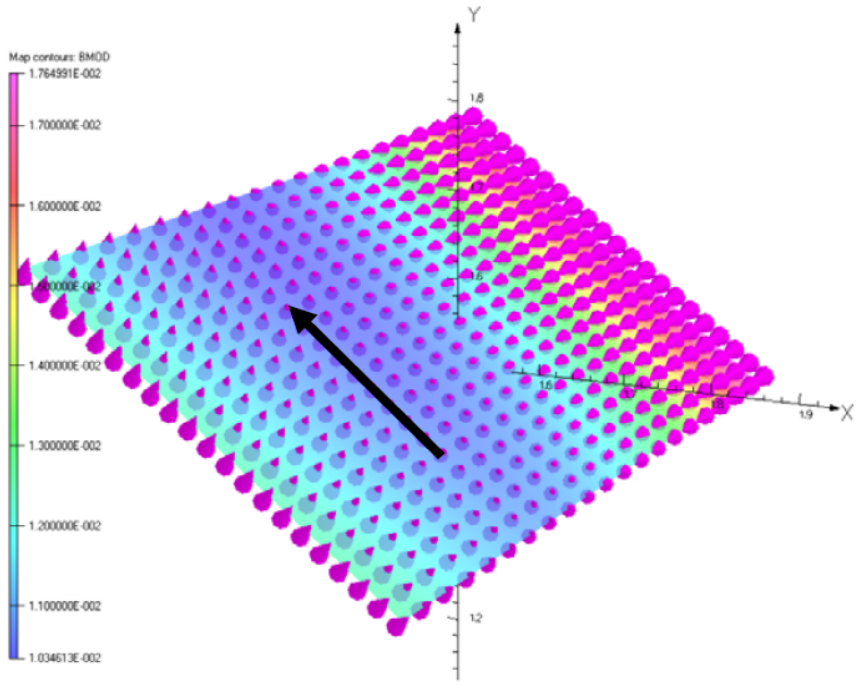

Figure 7.5: The simulation results of the magnetic field in the desired BSC PM tube location. The black arrow represents the orientation of the photomultiplier tubes in this region. The cones represent the direction of the magnetic field.

The PM tubes will be mounted at an 45°angle with respect to the x axis. If the results of the simulation data are correct, the angle between

the magnetic field vectors and the PM tube central axis should not deviate from the perpendicular by more that 1°, as shown in figure 7.6 in which the gradient of the magnetic field in the x-y plane has been plotted for positions along the z axis. The chosen location puts the PM boxes tangential to the HF calorimeter at a z distance of 11.5 - 12.5m with the centre line being at $x = 1.5$m, $y = 1.4$m.

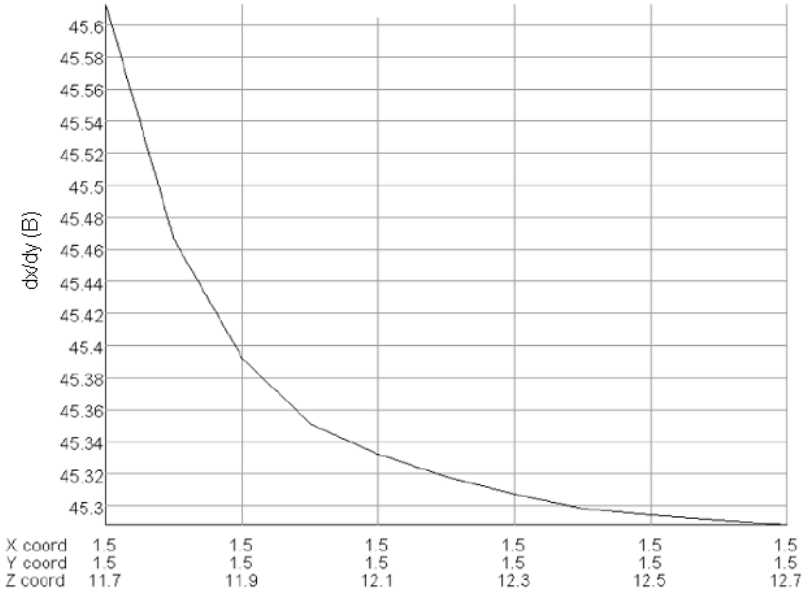

Figure 7.6: The radial angle of the magnetic field vector in the x/y plane. The simulation shows a nearly constant angle of 45°w.r.t the horizontal x axis. The PM tubes are mounted to provide a 90°angle of incidence between the field and the PM tubes' central axis, depicted by the black arrow in figure 7.5 for $z = 11.7$ to 12.7m.

7.3 Plateau Curves

One method of finding the correct bias voltage for the PM tubes is to plot curves of count rate verses bias voltage [60]. A scintillator tile connected

to the PM tube under test provides a constant rate of signal from cosmic muons. The PM tube output was connected through a discriminator to a counter that recorded the number of hits in the tile over a given time. An example plateau curve is shown in figure 7.7 for tube number 17206.

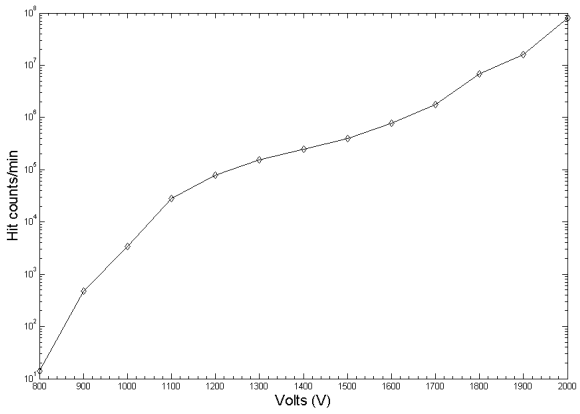

Figure 7.7: An example of a scintillator counter plateau curve. The correct bias voltage lies midway on the linear section between the knee and the second sharp rise of the curve [60]. Notice that the data is plotted with a $LogY$ axis. Hence, the linear section represents the exponential curve discussed in figure 7.2.

The knee of the plateau curve represents the absolute minimum supply voltage at which each tube should be operated. The correct operating voltage lies midway between this knee voltage and the breakdown voltage, which shows up as an increase in the gradient at the higher voltage end of the x axis. Hence for the tube shown in figure 7.7, the high voltage supply should be set at around 1500v. Measurements for several other PM tubes were made. However, not all produced adequate plateau curves that could be easily used for determining the correct bias voltage.

Many of the plateau curves gave unsatisfactory results leading to the

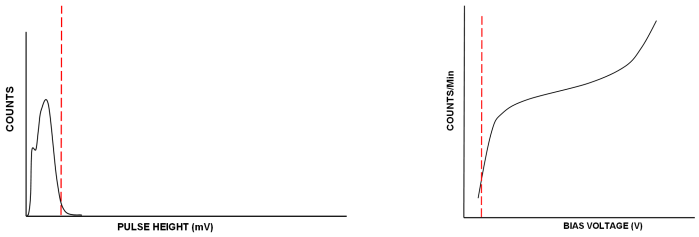

(a) Very Low bias voltage. Few signals get through the discriminator.

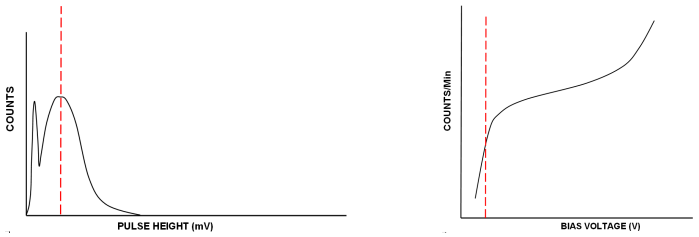

(b) Low bias voltage.

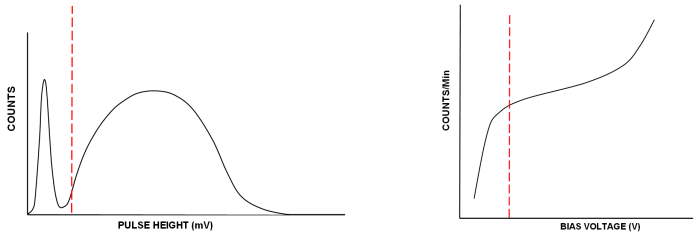

(c) Minimum acceptable bias voltage.

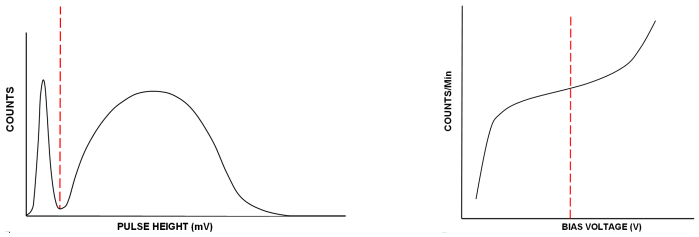

(d) Correct bias voltage. Mid-point of operating range.

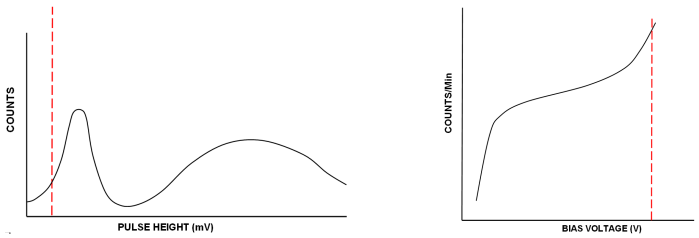

(e) Over-bias voltage. Regeneration effects occur.

Figure 7.8: Explanation of using the pulse height spectra to compensate for the ambiguous results of the plateau curves. The plateau curves (right-hand figures) can be viewed as the integration of all the pulse height spectrum (left-hand figures) counts above the discriminator threshold (red dashed) line[60]. See text for details.

inability to determine the correct bias voltages for the PM tubes. The plateau curve shape for a scintillator tile / PM tube pair is correlated to the pulse height spectra for the particular radiation source used[60]. The left-hand column of figure 7.8 shows the pulse height spectra for increasing bias voltage, with the red, dashed line representing the discriminator's threshold voltage. As the bias is increased, more of the signal spectra overcomes the threshold level and is counted. This effect is depicted by the increased spread of the signal above the threshold level. The right-hand figures show the resulting plateau curve; the red line depicting the relevant point with respect to the pulse height spectra diagrams. The plateau curve can be viewed as an integration of all the pulse height spectra counts that fall above the threshold level. If the plateau curves gathered were adequate, knowledge of the correct bias voltage for each tube could be gained by taking the midpoint of the plateau region. This is equivalent to the *minimum* voltage at which *all* of the signal appears above the threshold and *all* of the noise falls below the threshold in the pulse height spectra diagrams (see sub-figure (c)).

Many pulse height spectra were recorded for various bias voltage values for each tile-tube pair[35]. These spectra are described in section 7.4 and were used to determine the correct PM tube bias voltages in lieu of satisfactory plateau curve results. With this knowledge and the use of the embedded LEDs, accurate bias voltage tuning will be achieved once the BSC is fully installed.

7.4 Tile & PMT Signal Characterization

The PM tubes have a specified operating voltage between 750v – 900v, with a maximum voltage rating of 1800v [18]. For a 10 dynode tube, such as the EMI9902KA, a change in supply voltage of 1% will alter the overall gain by 10%. At low supply voltages (700v – 800v), the noise output from the tube, as explained in Chapter 5 is minimised. However, this is at the expense of energy resolution with most of the ionizing particles passing through the scintillator resulting in roughly equal amplitude signals irrespective of the energy they deposit or may be too weak to overcome the discriminator threshold levels resulting in a loss of detection eficiency.

The PM tubes were therefore tested to determine the optimum voltage level at which the signal and noise can be best differentiated without increasing the noise beyond a reasonable level or running the risk of damaging the PM tube.

7.4.1 Signal Characterization of Tile - PM Tube Pairs

Preliminary tests of the front-end hardware had been carried out and shown that the majority of the components were in good condition or needed only minor repairs. However, comprehensive measurements of the typical signal amplitudes, fall-times and widths needed to be made as these play an important role in developing a successful readout system. Figure 7.9 shows a typical signal from a scintillator tile and PM tube when a cosmic muon traverses the tile. The amplitudes, pulse widths and fall-times were measured using the math functions of a Lecroy oscilloscope and a GPIB

interface controlled with MATLAB software [35].

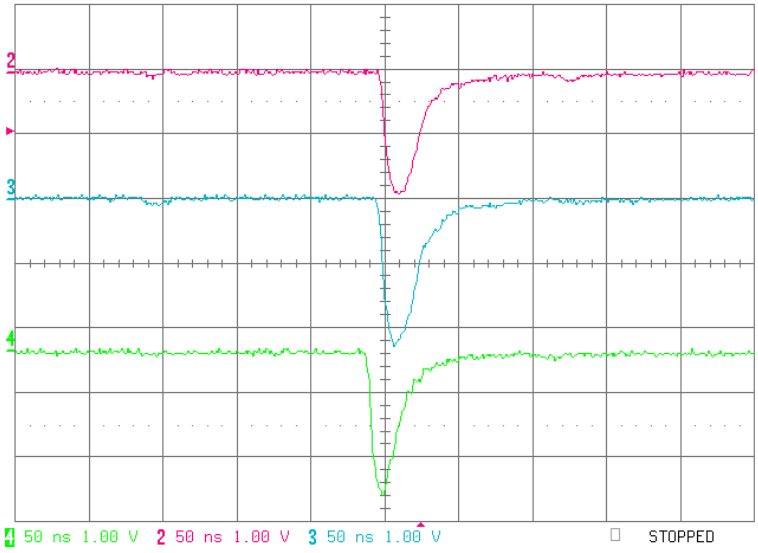

Figure 7.9: An example of typical muon pulse traces seen on the oscilloscope. Triggering was achieve using two scintillator tiles set up as a coincidence hodoscope (upper and lower traces).

The amplitude spread of a typical channel determines the dynamic range requirements of the readout pre-amplifier and helps set the PMT operating voltage to a optimum level. The spread of the fall-times and pulse widths play a part in determining the time resolution of the system; longer fall-times and longer pulse widths result in pulse pile up if two or more hits occur in quick succession. The experimental set up, shown in figure 7.10 used two tiles, one above and one below the tile to be tested, acting as a coincidence hodoscope for a trigger.

The signals from these two tiles were amplified by a PM amplifier with a 10× gain in order to overcome the minimum discriminator level of -30mV and hence minimizing the bias to the measurements. The discriminator thresholds were set to this minimum level. The outputs from

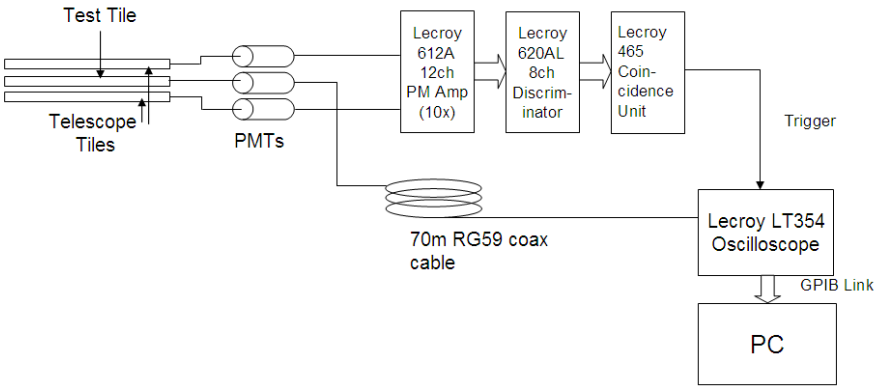

Figure 7.10: Experiment set up for measuring the signal characteristics (amplitude, fall-time and width spectra) of the PMT-Tile pairs. 70m of RG58 coax cable was used to mimic the effects (reduced signal amplitude, loss of high frequencies etc) of the signal cable used in the UXC.

the discriminator were fed in to the coincidence unit and the coincidence window set to 20ns. Signals from both of the tiles had to occur within this time window in order for a coincidence trigger pulse to be produced. The trigger pulse was connected to channel 3 of the oscilloscope while the direct analog signal from the test tile and PM tube was connected to channel 1. Using MATLAB and the GPIB interface, channel 3 was constantly monitored for the appearance of a coincidence trigger signal, marking the event of a cosmic muon traversing the three tiles. When a trigger occurred, the corresponding signal from the test tile was measured for its peak amplitude, fall-time and negative pulse width. 10000 hits were made for each tile-PMT pair and histograms made for each data set. An example of an amplitude spectra, fall-time spectra and pulse width spectra are shown in figure 7.11.

The operating voltage of the PM tube under test was set to a level at

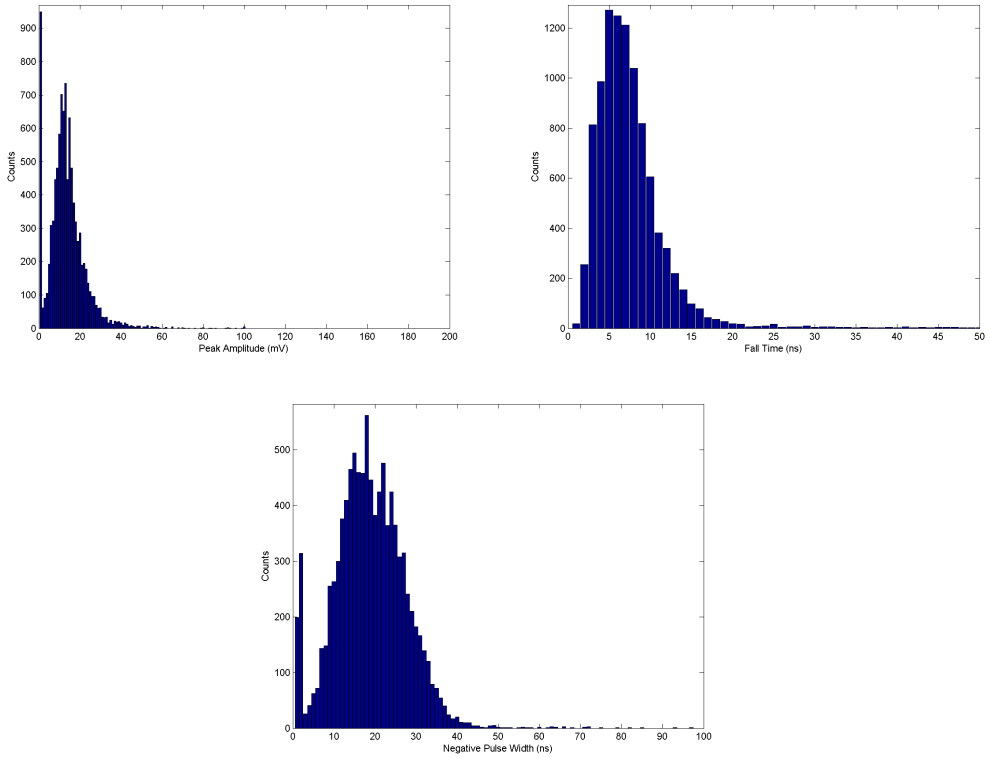

Figure 7.11: Example of the signal characteristics for a PMT-Tile pair (Tile number 14small, PM tube #17211). (top) Amplitude histogram, (middle) Fall time histogram, (bottom) Negative width histogram.

which the signal and noise began to have a visible separation in the resulting signal amplitude histogram. This voltage differed between each PM tube and represented the minimum voltage level at which each PM tube could be operated. Essentially, it represents the voltage at which the knee occurs in the plateau curves explained in section 7.3. These voltages were noted and are given in table 7.2.

7.4.2 Scintillator Efficiency Curves

It was known that the scintillator tiles may have suffered some radiation damage during their use in OPAL. This radiation damage would cause 'dead centers' or opaque areas in the plastic scintillator, effectively reducing the active area of the tile. For a detector like the BSC, it is important that all the scintillator tiles are functioning in a uniform way with no large differences in tile efficiency. Any differences must be known to enable a correction factor to be applied to the count rates from each individual tile. For this purpose, efficiency curves were plotted for several of the tiles. The set up for the generation of the efficiency curves is shown in figure 7.12.

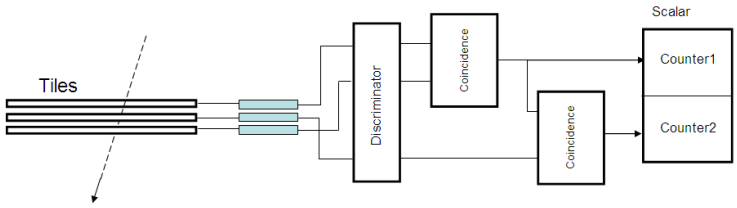

Figure 7.12: The experimental set up for producing efficiency curves.

The top and bottom tiles form a hodoscope from which a coincidence trigger is produced when a cosmic muon particle traverses the three tiles. The PM tubes connected to these two tiles are supplied with a sufficiently high bias voltage to ensure all hits in the scintillators are registered. In this case, the voltages were set to 1700v. Any particle that passes through the upper and lower tiles must also have passed through the center tile connected to the PM tube under test. The coincidence from the upper and lower tiles thus forms a reference counter for the number of particles per minute to be

detected and is displayed on counter 1. The output from the central tile passes through the discriminator to a second coincidence unit where it is compared with the coincidence of hits per minute from the hodoscope tiles. If the operating voltage of the tested PM tube is too low, a lower count rate will be recorded on counter 2 as many signals fail to pass through the discriminator. As the operating voltage is increased, the count rate of counter 2 rapidly increases. At some point, the count rate of counter 2 will equal the count rate of counter 1 if the tile under test is of equal efficiency. If however, 'dead' patches or opaque centers exist in the test tile, the compared efficiency will be lower. Therefore, a knowledge of the relative radiation damage of each tile can be obtained. Increasing the operating voltage further should show little difference between the two count rates until the PM tube noise is produced at such a high rate and amplitude that the count rate of counter 2 exceeds that of counter 1.

The efficiency curve is formed by dividing the value of counter 2 by the value of counter 1. The error of each point was dependent on the number of true counts N taken and was calculated by;

$$\sigma = \sqrt{\frac{\epsilon(1-\epsilon)}{N}} \tag{7.1}$$

where ϵ is the efficiency calculated by taking the ratio of *true counts* of counter 1 and *detected counts* of counter 2.

An example of an efficiency curve is shown in figure 7.13. In this example, the efficiency rises to approximately 90% at a bias voltage of 1100V. The position of the three tiles were then exchanged so that the previously tested

tile was used as one of the hodoscope tiles and visa versa. The efficiency measurements for all 36 tile segments are in progress. So far all tiles tested show a satisfactory level of efficiency ($> 80\%$).

The PM tube bias voltage plays an important role in these tests. Excessive bias voltage causes high amplitude noise and eventual discharge of the PM tube, both of which would effect the efficiency measurements. Therefore, knowledge of the absolute maximum voltage at which the tubes will sustain before discharging was required. The voltage was increased up to 2500V on one tube in an attempt to find the point at which the curve increases beyond the counter 1 value indicating that the tube is on the verge of breakdown. At 2500V, the amplitude and rate of noise from the tube were sufficient to produce multiple counts within the coincidence window of counter 1, thus giving an efficiency ratio greater than 1. At this *breakdown voltage*, the voltage was immediately reduced to prevent permanent damage to the PM tube.

7.5 Magnetic Field Tolerance of the T2 Rack Cooling Fan Tray

The Beam Radiation Monitoring (BRM) front-end electronics are to be housed within the T2 racks on the platforms behind the Hadron Forward (HF) calorimeters in the region of $z = 14.6$m. This rack will also contain the front end systems of TOTEM and possibly CASTOR. As yet, it is unclear what the power dissipation of the electronics will be and it is possible that

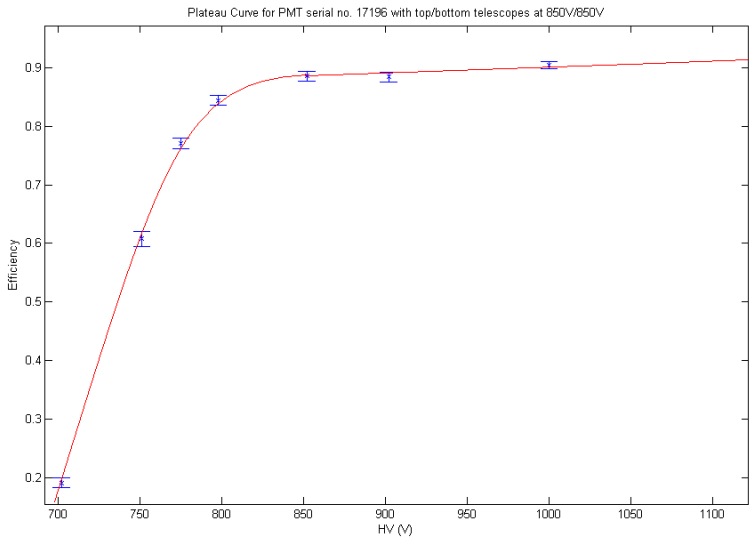

Figure 7.13: An example of an efficiency curve for one of the scintillator tiles.

auxiliary cooling will be required in addition to the standard tangential fan cooling. Any motor-based fan system used in the T2 rack must be capable of operating within the fringe magnetic field environment expected. An auxiliary fan tray, manufactured by INEO ALPES (CERN SCEM No 06.61.77.711.0) was tested in a magnetic field to determine if it could be a suitable solution.

The INEO ALPES fan-tray was placed in the magnet with a Lecroy AP015 current probe attached to the positive conductor of the 240v AC power input. The current probe was attached to a Lecroy LT354 oscilloscope and the rms current recorded for various magnetic field strengths. The ambient current, with no magnetic field and the main switch of the fan tray turned off was 63mA $\pm$ 5mA.

With no magnetic field and the main switch on, the *normal running*

current was 508mA ± 5mA. Each fan consumes 16W. The current flow in to the fan-tray was monitored in the hope that this would give some early indication of the magnetic field effects. However, the change in current was too small and listening to the change in the tone of the fans gave the best indication. The motors ceased rotation when the magnetic field reach 3000G.

The fan tray was too large to turn a full 90° within the magnet poles. The maximum angle was approximately 20°. This was used as a reference angle for the *off-axis* magnetic field measurements. The relevant x and y components of the field could then easily be calculated using trigonometry. The fan tray was set at an angle of approximately 20° from horizontal and the tests were repeated. The fans started to slow down, thus displaying symptoms of the field when the field reached 200G, corresponding to a y-component of 187G and an x-component of 68G. Therefore the maximum x-component field allowed is approximately 60-70G and the y-component maximum is approximately 2500G.

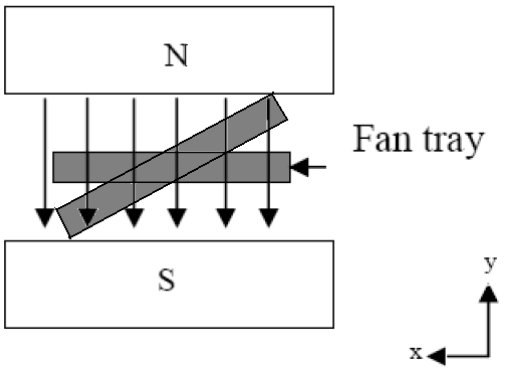

Figure 7.14: Diagram of the IENO fan tray in the horizontal and approximately 20°position in the test magnet.

7.5.1 Predictions from Simulation Data

CMS magnetic field simulation data had been prepared by the CMS integration group. With this data, line and surface plots can be made for any defined region on CMS. The T2 racks will be positioned on a ledge behind HF and an approximate position of $x = 1.8$m, $z = 14.6$m. Figure 7.15 shows a surface plot of the magnetic field for this region with y starting at the level of the center of the beam pipe and going down -2m to the approximate level of the edge. The field strength in this region varies between 525G near the HF rim, down to 100G near the position of the ledge. The majority of T2 will be situated in a 100G - 250G field. The direction of this field with respect to the fan-tray is important in determining the effect that it will have on the fans operation.

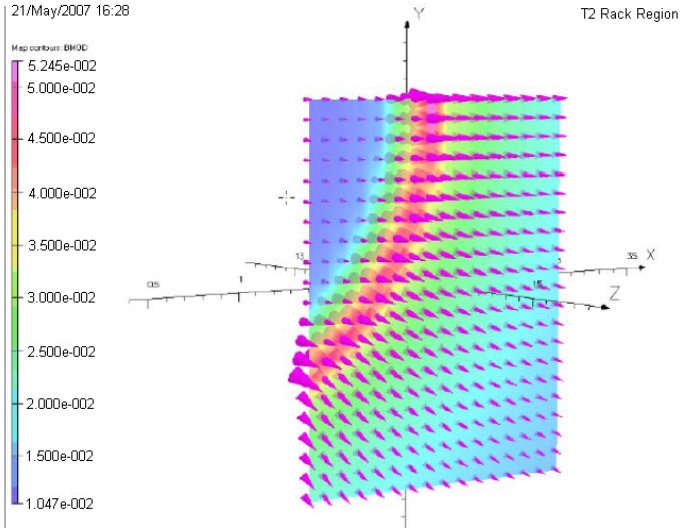

Figure 7.15: Vector field map of the magnetic field strength and direction around the T2 rack region[48]. Field strengths are given in Tesla*

The graphs shown in figure 7.16 represent the field strength (red) and

field vector angle w.r.t the horizontal fan tray (blue) for a line along $y = 0$ to y = -2m at x = 1.8m, z = 14.6m. The incident angle was calculated by:

$$\theta = arctan\frac{by}{bx} \tag{7.2}$$

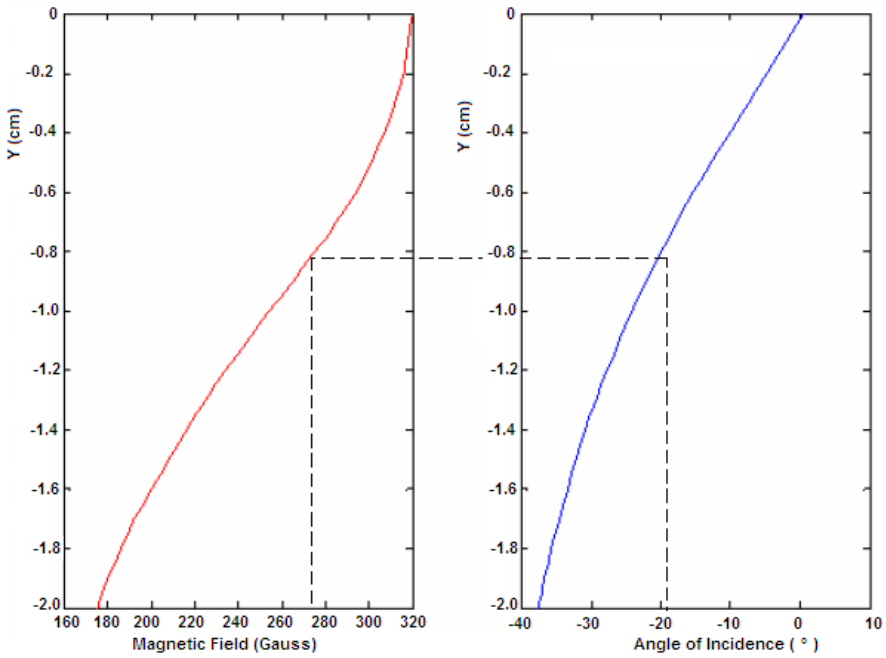

Figure 7.16: A plot of the magnetic field strength and angle of incidence along a vertical line through the T2 rack. Simulations show that the magnitude of the field at this angle of incidence will be in the region of 270G.

As stated previously, the maximum horizontal field magnitude in which the fan-tray could operate was measured to be in the region of 60 - 70 Gauss. Figure 7.16 shows the magnitude of the simulated magnetic field (left) and the angle of incidence of the magnetic field (right) in the region of the T2 racks as a function of height. Tracing a line from 20°on the right-hand graph, the magnetic field will enter the T2 region at this angle at around y = -0.8m. On the left-hand plot, the magnitude of the field at y = -0.8m is

approximately 270G with x and y components of 110G and 246G respectively. This magnitude is 200G over the measured limit.

The conclusion drawn from this experiment is that the INEO fan trays cannot be used for cooling the T2 rack electronics as they will not rotate due to the CMS magnetic field. Magnetic field shielding is not a feasible option due to lack of available space within the rack and the obvious impedance to airflow that this would cause. It was therefore decided that a water-cooled system will be fitted to the T2 rack and this system must remain on at all times to help protect the BRM front-end electronics.

PMT No.	Tile No.	Voltage (min)	Voltage (set)
17065	C1B	964V	1582v
17102	C1C	803V	1502V
17103	C3D	864V	1532V
17104	6S	858V	1529V
17105	5S	974V	1587V
17106	C5C	1049V	1624V
17107	C4B	1002V	1601V
17108	C2D	758V	1479V
17109	1S	1017V	1609V
17110	C1A	984V	1592V
17111	C3B	997V	1598V
17113	C2C	967V	1584V
17114	13S	1028V	1614V
17115	C4A	1167V	1684V
17116	C2B	1149V	1675V
17117	C5B	911V	1556V
17118	C3C	925V	1563V
17119	C6D	966V	1583V
17120	C2A	1189V	1694V
17121	C3A	923V	1561V
17136	C4C	792V	1496V
17187	10L	960V	1580V
17196	6L	998V	1599V
17197	1L	947V	1573V
17200	C6A	793V	1496V
17203	16S	941V	1570V
17206	14S	1206V	1703V
17207	11S	943V	1572V
17209	C1D	1098V	1649V
17211	14S	993V	1596V
17217	C5A	998V	1599V
17219	16L	865V	1532V
17225	14L	967V	1583V
17227	5L	950V	1575V
17229	C4D	798V	1499V
17230	C6C	799V	1500V
17231	C6B	930V	1565V
17232	C5D	900V	1550V
33001	11L	870V	1535V
33002	13L	984V	1592V

Table 7.2: List of tile and PM tube pairing, their defining S/N separation voltages (V_{min}) and their approximate operating voltages (V_{set}).

B field	Current (RMS)
200G	515mA ± 5mA
500G	509mA ± 5mA
1000G	503mA ± 5mA
1500G	507mA ± 5mA
2500G	508mA ± 5mA
3000G	Motors Stopped

Table 7.3: Current drawn by IENO fan tray as the magnetic field is applied. The current did not provide the expected early warning sign of fan failure.

Chapter 8

BSC Readout

The BSC uses two almost independent readout systems to fulfill its design requirements as a particle and background rate monitor and as a technical trigger generator. The primary role as a rate monitor will be carried out using VME* hardware controlled by a rack mounted PC running Scientific Linux 4, described in detail in section 8.1. The secondary purpose of providing technical trigger inputs will be done using older NIM modules which are robust and easy to rewire without the need for any control and acquisition software. This is described in section 8.2. The signals from the 36 PM tubes will first enter a NIM based PM amplifier module with a fixed 10× gain. This module also provides a dual output for each input so the signals can be duplicated for the purpose of the VME and NIM based readouts. This scheme does not rely on the use of a VME discriminator with ECL fan outs to split the signal and keeps the technical trigger NIM readout independent

* Versa Module Europa. Based on the earlier Eurocard standard. As well as allowing connectivity of many modules of differing functions, the VME bus provides a method of fast module control and data acquisition by access to the modules' registers.

of the VME readout. Hence, the primary rate monitoring readout can be altered more freely without changing the important timing characteristics of the technical trigger signals.

8.1 The VME Readout System & HAL

The core purpose of the BSC readout is to monitor the timing and relative quantities of incoming background and outgoing collision products in the CMS region. As such, the readout electronics must be capable of resolving signal timings on the sub-nanosecond scale with adequate accuracy. A readout system consisting of VME (Versa Module Europa) modules designed for purposes such as this along with a PC running Linux OS (SLC4) was chosen due to previous usage in other HEP experiments as well as the available support from the manufacturers and CERN based software groups.

The basic units of the VME crate is shown in figure 8.1. The raw PM tube signals are first split in to two paths. One path goes to the NIM based technical trigger crate as explained in subsection 8.2. The second branch is directed in to the inputs of several VME Constant Fraction Discriminator modules [9].

8.1.1 V812 Constant Fraction Discriminator

The CAEN V812 constant fraction discriminators (CFD) serve two purposes. First, they remove the low amplitude background noise inherent from PM tubes. Secondly, they convert the analogue signal in to a fast rise time ECL pulse that is required by the TDC module. CFDs were chosen due

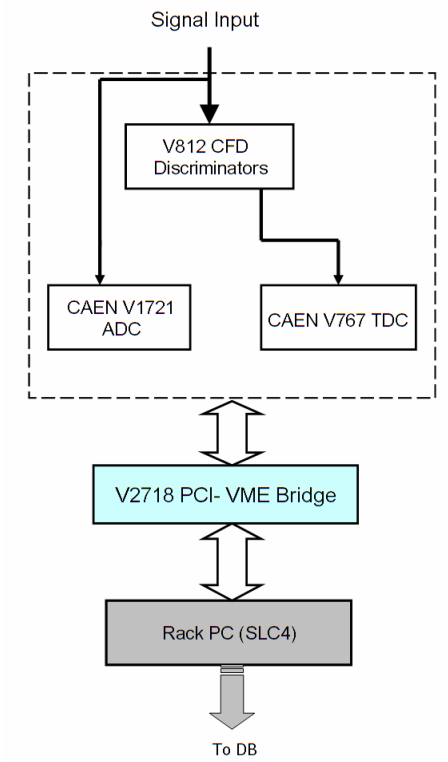

Figure 8.1: The inter-connections of the VME modules to form the BSC's rate monitoring readout.

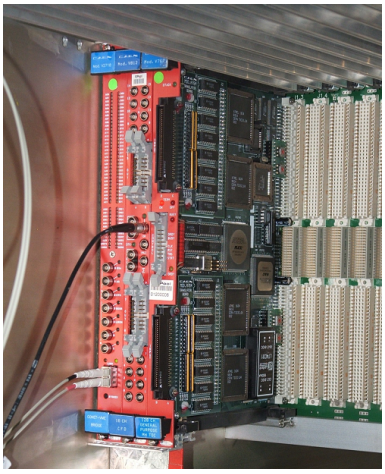

Figure 8.2: The VME Crate and modules which will form the BSC's readout system for rate monitoring.

to the necessity for accurate and consistent timing of the BSC system. Unlike standard discriminators which produce a logic output only when the amplitude of the input signal crosses a preset threshold, a CFD uses an algorithm that determines when the input signal voltage surpasses a fixed fraction of its own peak amplitude, as shown in figure 8.3. This in effect gives a well defined output trigger time which is independent of the input pulse height.

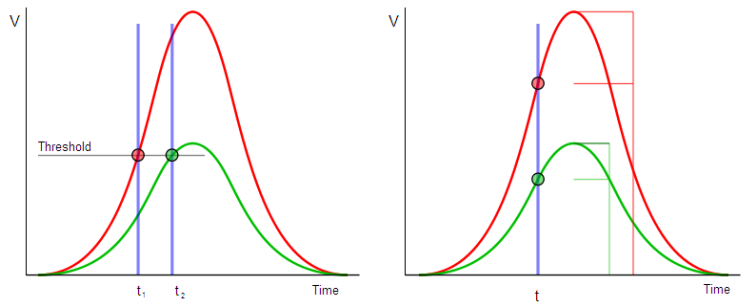

Figure 8.3: Diagramatical representation of the trigging response of the constant fraction discriminator (right) compared with that of a standard discriminator (left).

The V812 uses a fixed fraction level of 20%. The user can still define the input level threhold to reject signals below a chosen amplitude, as with the standard discriminator module. The difference with the CFD is that these thresholds do *not* corrospond to the actual level that triggers the discriminator output, this being a 'constant fraction' of the input signal [3].

The adjustment of the thresholds for the CFD is done via a script that is called before the start of a data acquisition by the Hardware Access Library (HAL), explained in 8.1.3. The script is in the form of a text file and can enable or disable any of the 16 discriminator channels as desired and set up the threshold levels of each channel individually up to a level of -250mV.

8.1.2 V767 Time-to-Digital Converter

The CAEN V767 Time-to-Digital converter (TDC) comprises of 128 independent input channels spread over 4 deadtimeless Time-to-Digital Converter (TDC) chips developed at CERN by the ECP-MIC group [25]. The internal block diagram of the 32 channel TDC IC is shown in figure 8.4. A 40MHz clock is fed into the CLOCK pin of the IC and divided by the Delay Locked Loop to provide the required time resolution. Hit signals from the detectors (in the case of the BSC this is the scintillator tiles and PM tubes) are input in to the HIT pins of the IC where they are stored temporarily in the Hit Registers. When a hit is detected the timing information is loaded into the primary hit register. The time measurement is then transferred in to the secondary hit register before being passed to the event buffer. This double register scheme ensures that very good double pulse resolution can be obtained.

A START pulse input is provided via a dedicated channel on the TDC chip. The connection to this is made via the START input pins on the 'control' connector of the V767 module*. A detailed explanation of the TDC32 IC is given in [25].

The V767 module contains a 32-bit output buffer, 20-bits of which are assigned to the time information. Figure 8.5 shows the bit assignments of the output buffer.

The data content of the output buffer is given by the values of END OF

* The CONTROL input connector uses Emitter Coupled Logic (ECL) levels. The advantage of ECL is that the I/O transistors are always in the active region and can thus change states at very high speed.

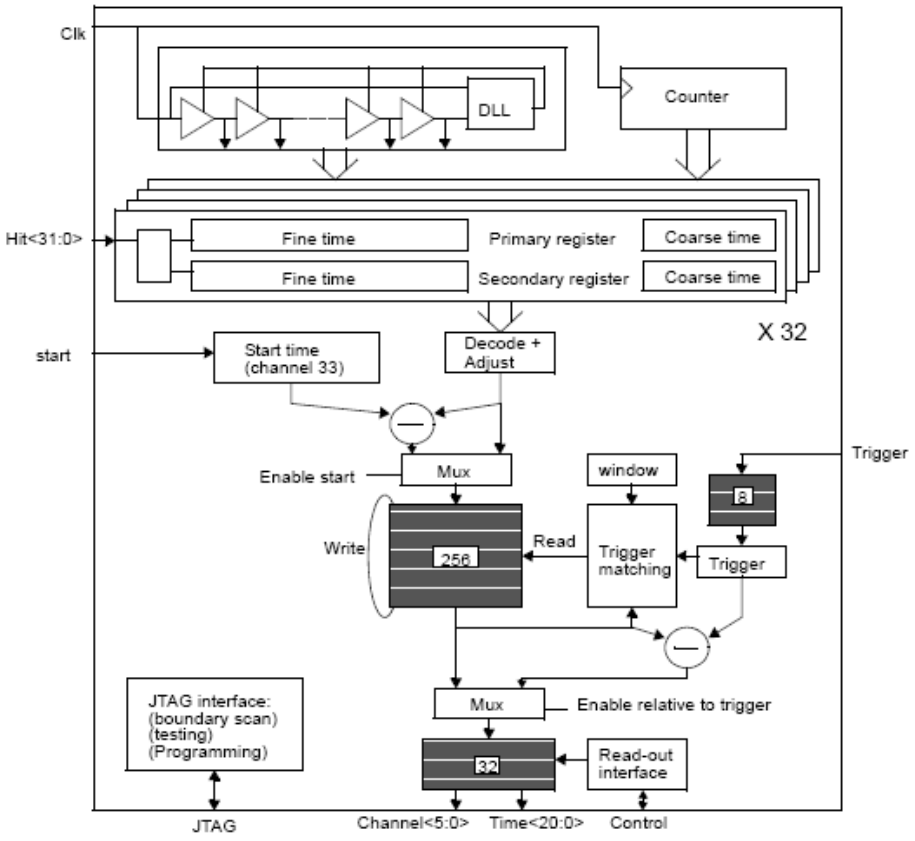

Figure 8.4: Block diagram of the 32 channel TDC IC used in the V767 [25].

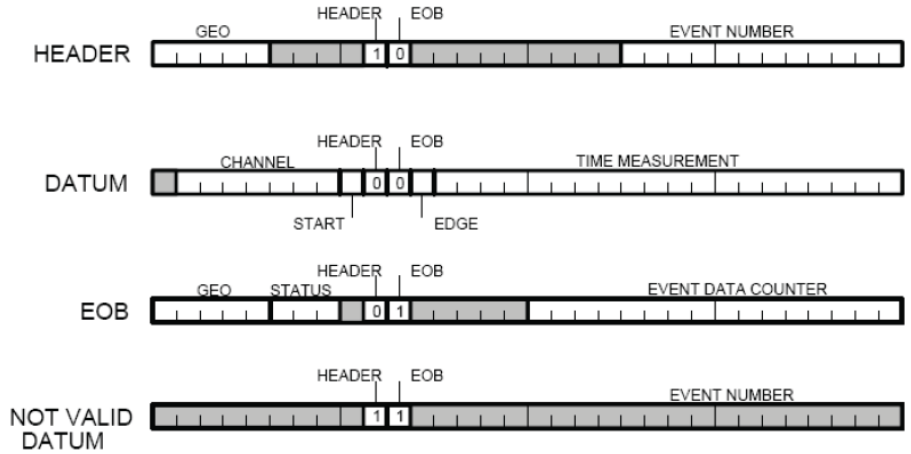

Figure 8.5: Diagramatical representation of the CAEN V767 output buffer.

BLOCK (bit 21), HEADER (bit 22) and START (bit 23). For instance, if the values of these three bits are all zero, there is event datum in the buffer. Bits 1 to 20 contain the event time measurement in the number of clock pulses. Bits 25 to 31 contain the channel number on which the hit was registered. If the START bit is high, this would signify the occurence of a start pulse on the specialized START control line pin.

The Time Measurement data appears as a number of clock pulses since the previous reset. The internal clock of the TDC runs at 40MHz and is divided internally in to 32 equal pulses by a Delay Locked Loop. The time represented by the LSB of the output buffer event time measurement is therefore $\frac{1}{32}\frac{1}{40MHz} = 0.78125ns$. With a counter size of 20 bits, the time measurement counter will rollover every $(2^{20} - 1) \times 0.78125ns = 819.2\mu s$.

Four basic errors can occur with the TDC acquisition due to excessive data rates or because of the TDC internal Delay Locked Loop (DLL) failing to synchronize after a module reset. An error code register exists which contains four 1-bit flags to report if any of these errors occur. If the input signal rates are too great, the event buffer or trigger buffer of one or more of the TDC ICs may overflow resulting in a loss of data. To clear the error codes, a front-end reset of the module must be carried out. Acquisition cannot recommence until the DLL has had sufficient time to resynchronize. If a hit signal arrives before the DLL has locked, 'Not Locked' and 'Hit Error' flags will be appear in the error register. Further explanation of these errors can be found in the TDC IC manual [25].

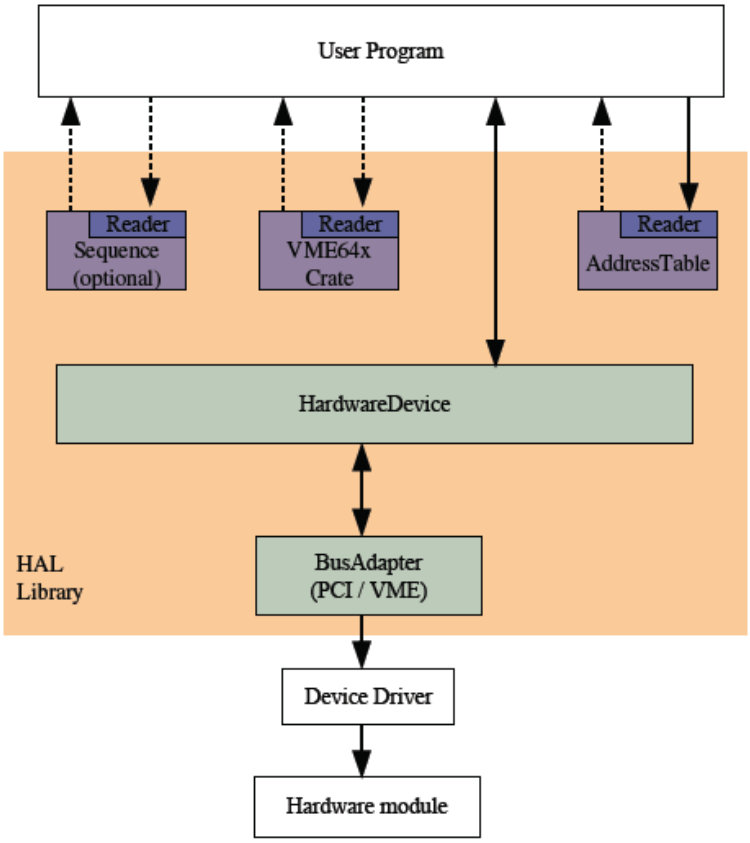

Figure 8.6: Functional blocks of the HAL. The arrows represent information exchange. A dashed arrow indicates an optional information flow [14].

8.1.3 VME Control & the Hardware Access Library

Control of the VME modules is done via a V2718 PCI-VME optical link bridge as shown in figure 8.1. Control commands are generated by a software system developed at CERN called the Hardware Access Library, HAL [14].

HAL is a library developed for the CMS data acquisition system and provides a high level interface which facilitates hardware access to VME or PCI modules. It is particularly useful in the event where hardware modules may need to be changed for newer models. In such cases, only the module's access table needs to be replaced in the code. In effect, HAL acts as a layer

between the the hardware device drivers (in this case the CAEN drivers) and a user program, allowing user-friendly and manageable access to the device through the use of a bus adapter and address tables [3]. Figure 8.6 shows a block diagram of the HAL functionality.

8.1.4 TDC Acquisition Modes

The V767 TDC modules has the ability to run in one of five acquisition modes [8]. These modes are;

- Continuous Mode
- Stop Trigger Mode
- Start Trigger Mode
- Common Stop Emulation Mode

After investigating these modes [3], the Continuous Mode proved to be the one most suited to the task of the BSC. In this mode, the entire LHC orbit train can be sampled without the need of triggering to start or stop the acquisition.

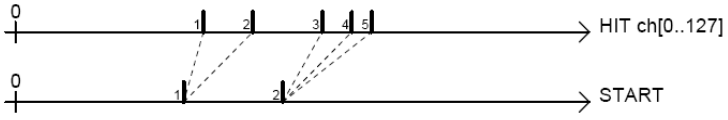

Figure 8.7: Continuous mode sequence. In this mode, there is no selection of a specific set of 'valid data'. All HIT signals that reach the enabled channels and all START signals lead to the storage of data in the local buffer [8]

8.1.5 Development Acquisition Code

The acquisition code was written in C++ on Scientific Linux 4. The code was written to give the maximum data sampling rates. Error flags were checked only when the output buffer contained 'Not Valid Datum', therefore minimizing the amount of time spent checking the error register unnecessarily. A flow diagram of the data acquisition code used for development purposes is shown in figure 8.8.

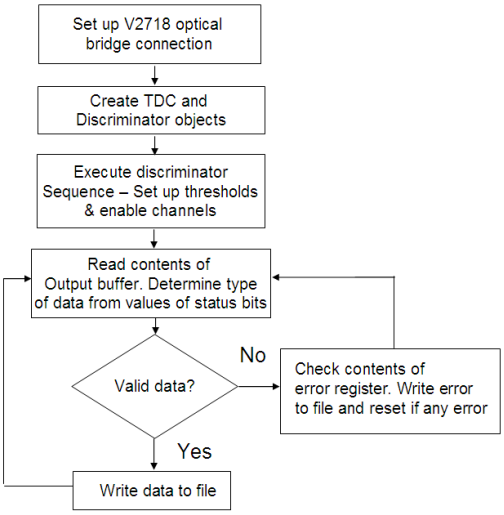

Figure 8.8: Flow diagram of the VME acquisition C++ code used during the BSC development.

This code acquired the data during the PS test beam for the time-of-flight measurements and is also the core acquisition code for the BSC particle rate measurement readout.

8.2 The NIM Readout System & Technical Trigger

As the BSC is one of the few systems capable of detecting single minimum ionizing particles, it will serve the purpose of supplying an *almost* minimum bias trigger in to the Global Trigger (GT) system. Minimum bias pertains to decisions based on measurements where no prior expectations are implemented to filter out the possible false positives. Hence, a minimum bias trigger is by definition, the most sensitive trigger available. The GT requires ECL level trigger signals from the BSC based on a variety of schemes requested by the trigger group. These schemes are made up of a combination of *majority over threshold* outcomes and *signal timing* outcomes, as explained in section 10.3. The initial design for the BSC trigger output uses NIM modules, shown in figure 8.9. These modules were widely used in high energy physics until their replacement with CAMAC and, more recently, VME modules. However, they still provide a very useful method of building a simple, reliable readout system. As a provider of a trigger input, it is vital that the trigger signals produced by the modules do not drift in time relative to the input from the PM tubes.

An analysis of the time delay and time jitter of each of the basic NIM modules was carried out. The set up, shown in figure 8.10 consisted of a signal generator which provided both the (direct) trigger signal and a processed signal via each of the modules. Four basic NIM modules were used. First was the PM amplifier, followed by a standard discriminator followed by a coincidence unit and finally a majority over logic (MAJ) unit. The delay

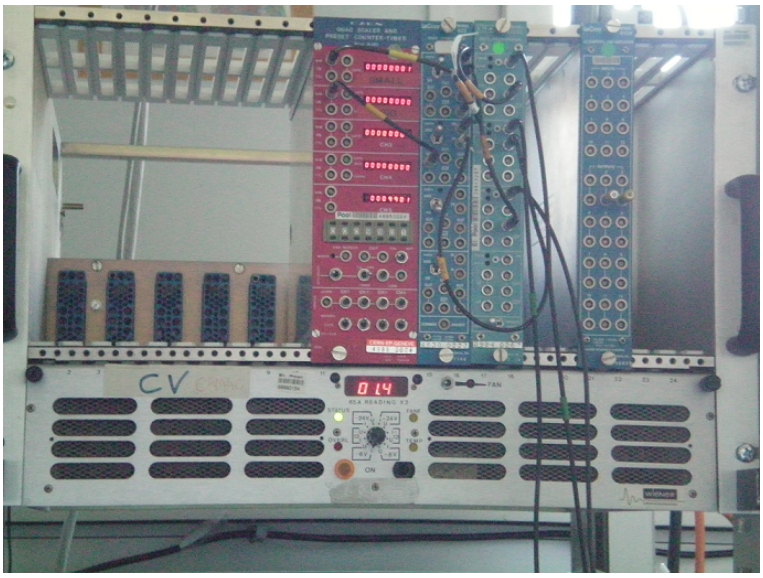

Figure 8.9: The NIM crate and modules which will form part of the BSC's technical trigger readout.

between the direct signal and the processed signal was measured over 5000 counts using MATLAB and a GPIB interface. The measurements were made in the following order (see also figure 8.10):

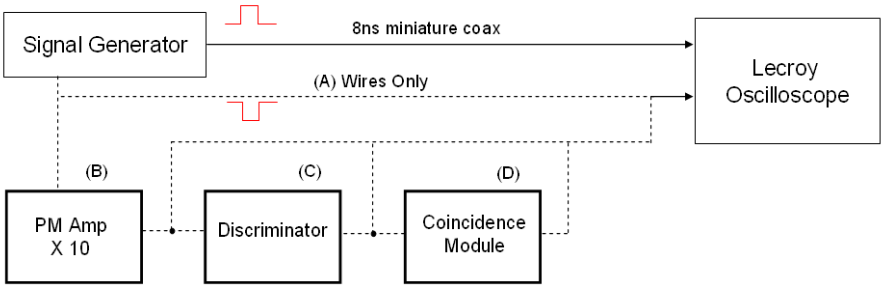

Figure 8.10: Set up of the NIM time jitter measurements. The intermediate cables between the modules all had a 1ns delay.

Figure 8.11 shows the resulting time jitter histograms for the signal generator, PM amplifier, discriminator and coincidence modules plotted on

the same axis to help visualize the inherent spread of each device as well as the time delay between the output of one module and the next. Table 8.1 summarizes these results of the Δt measurements and their corresponding 1σ spreads. The results show that the NIM modules do not generate any significant increase in the time jitter of the signal from the pulse generator and that the delay of the modules as a whole is stable with a mean value of 27ns. These characteristics are adequate for use in the BSC trigger readout. Details of the proposed design and implementation of the trigger readout is given in chapter 10.

- (A) Direct signal input with wires only.
- (B) Signal via the PM amplifier.
- (C) Signal via the PM amplifier and discriminator.
- (D) Signal via the PM amplifier, discriminator and coincidence unit.
- (E) Signal via the PM amplifier, discriminator and coincidence unit and majority over logic unit.

Section Tested	Δt	$\pm$
A	0 ns	0.8ns
B	10.2 ns	0.8ns
C	17.2 ns	0.7ns
D	29.2ns	0.6ns

Table 8.1: Time delays and jitter of the sequence of NIM modules used for the BSC technical trigger readout.

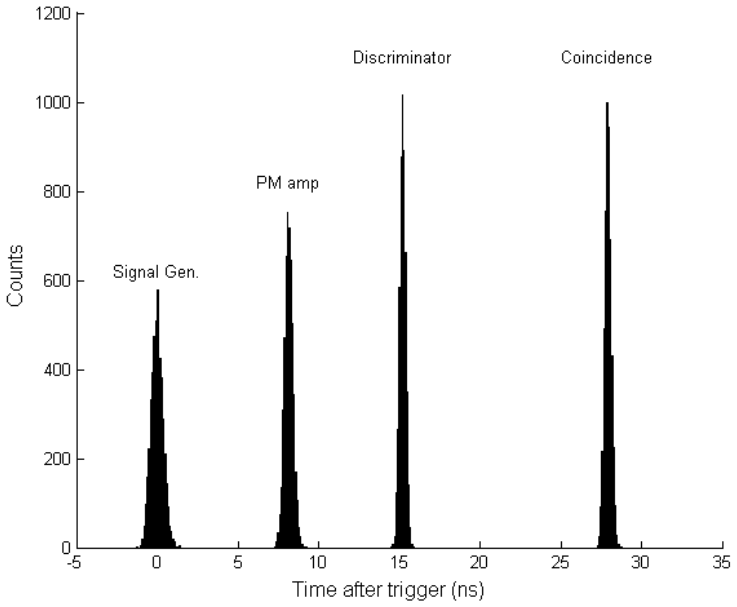

Figure 8.11: Results of the NIM time jitter measurements. The mean delay and standard deviation of the spreads for each module are given in table 8.1.

Chapter 9

Test Beam Measurements

There were two opportunities to put the BSC system into test beams during the course of development. The first test beam was held at the H8 beamline on the Super Proton Synchrotron (SPS) at Prévessin. The aim of the SPS experiments was to gather signal characteristics from the tiles and PM tubes and to further check the front-end hardware in a higher rate setting. The second set of test beam experiments were conducted during October - November 2007 at the Proton Synchrotron (PS) T11 beamline. The aim was to measure the timing resolution of the BSC system including the readout. Details of the experiments and their results are given in the following sections.

9.1 SPS Test Beam.

The first test beam experiments were held at the SPS accelerator during August 2007 and used protons and pions with an energy of 180GeV. The beam intensity was set at 10^5 particles within the 4.8s spill and the beam

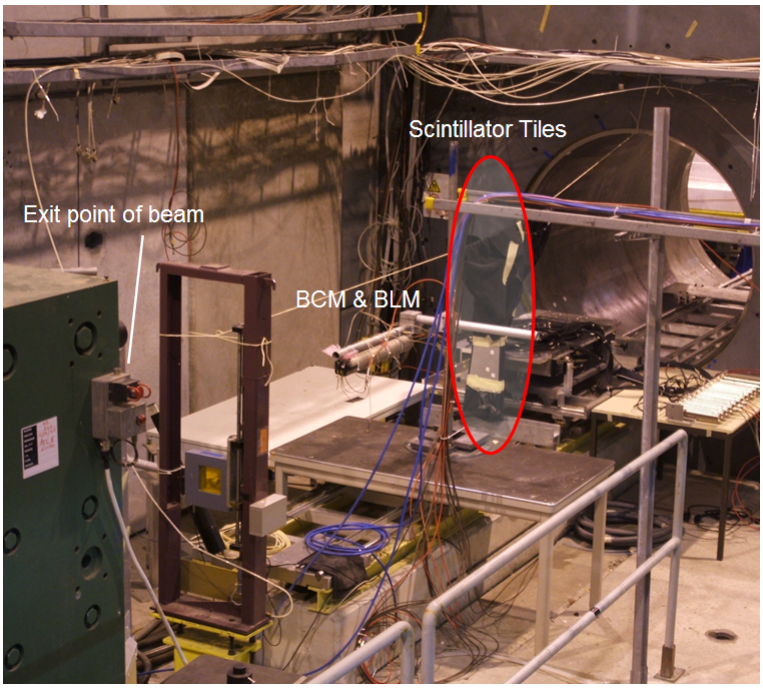

Figure 9.1: The SPS test beam set up in H8 Area. The three tiles are situated under the light-tight curtain in the centre of the photograph. The Beam Conditions Monitor (BCM) was undergoing tests in the same beamline and was the Beam Loss Monitor (BLM) ionization chamber.

size was measured to be 7.7 $\times$12.9mm (one σ) using a wire chamber mounted at the exit of the focusing magnet.

The set up is shown is figure 9.1 and consisted of a three tiles positioned back-to-back in line with the proton-pion beam. Coincidence logic set up between the front and rear tiles was used to trigger pulse measurements of the central tile in the same way as explained in section 7.4.2. Spectra of signal heights, fall-times and pulse widths were recorded using the test beam and confirmed the previous measurements made using cosmic muons.

Signals were sent to the readout hardware via a 70m RG59 coaxial cable to replicate the cabling installed from the UXC to the S1 area in the USC.

Measurements of the amplitude, fall times (a measurement of the time width of the leading edge of the raw pulses) and pulse widths (FWHM) were recorded using MATLAB and a Lecroy LT354 digital oscilloscope via a GPIB interface. 10000 beam induced signals were measured and histograms made.

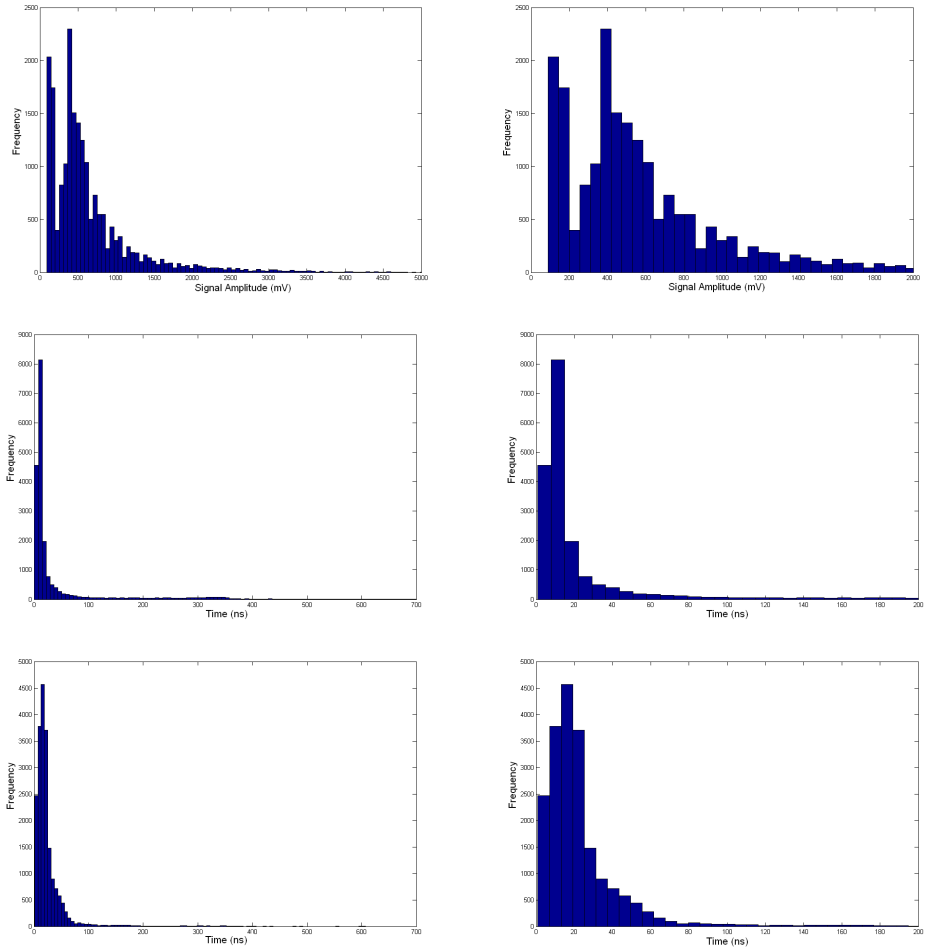

Figure 9.2: Examples of signal spectra histograms obtained at the SPS test beam on beamline H8. Full Spectra are given on the left. A closer view of the main data in shown on the right. Amplitude spectra (Top). Fall time spectra (Middle). Pulse width spectra (Bottom).

The spectra shown in figure 9.2 were obtained when running the PM tube at 1500v. At this voltage, a clear separation between the low amplitude PM

tube noise ($< 200mV$) and the greater amplitude signal can be seen. Lower operating voltages did not provide such a visual distinction between signal and noise. The signal to noise ratio for this particular set up operating at 1500v was calculated to be 14.3dB.

The information gained from the SPS test beam demonstrates that the front-end hardware will provide a sufficient signal-to-noise ratio and that the majority of signals produced from protons and pions have sufficiently short fall-times in the range of 5 - 15 ns. The width (FWHM) of the signals is reasonably long at a mean of approximately 20ns and a maximum of approximately 70ns. This feature will limit the BSC to a maximum signal rate per tile segment of around 15 - 20MHz before pulse pileup occurs which is much greater than the expected rates during the low luminosity commissioning stages.

9.2 PS Test Beam.

The Proton Synchrotron (PS) test beam was available in October to November 2007. The main aims of the PS test beam were to measure the time resolution of the BSC readout and obtain an estimate of the data rates. The output of the PS was set to a 2GeV proton-pion beam pulse of 400ms with a luminosity in the range of $\mathcal{L} = 10^4 - 10^5 cm^{-2}s^{-1}$.

Figure 9.3 shows the PS test beam area set up with two of the BSC tiles visible. A third tile was placed behind the black structure in the background. The set up is show diagrammatically in figure 9.4.

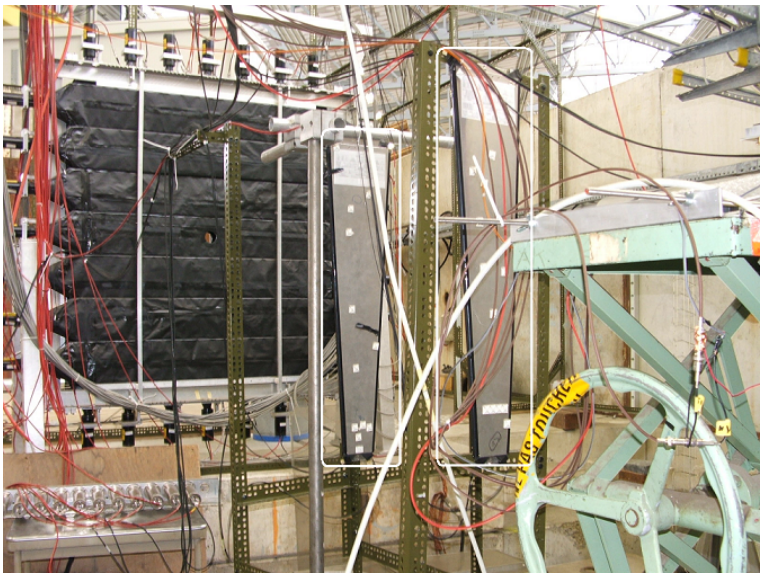

Figure 9.3: Tile set up in the PS test beam area.

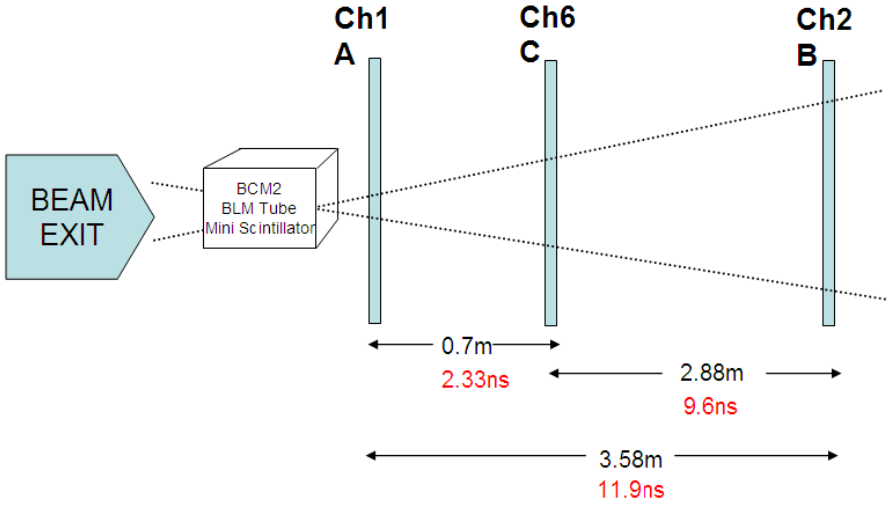

Figure 9.4: Schematic diagram of the PS test beam set up. The distances between the tiles A, B and C were chosen to simulate the calculated TOF of the LHC beam for the BSC1 and BSC2.

9.2.1 VME Hardware Time Jitter Measurements

In order to make any accurate conclusions about the resulting time of flight measurements produced at the PS test beam, it was first necessary that the inherent jitter of the discriminator and TDC were known. A Philips PM5786 signal generator was adjusted to give a negative going 1.0v pulse of 10kHz which was fed into CAEN TDC via the CAEN discriminator.

```
 8  127495     0     30
80  577180     0     30
 6  117564.844 1 143682
 6  217868.750 2 143683
 6  318171.875 3 143684
 6  418475.000 4 143685
 6  518776.562 5 143686
 6  619080.469 6 143687
 6  719385.156 7 143688
 6     488.281 8 143689
 6  100793.750 9 143690
 6  201096.875 10 143691
 6  301399.219 11 143692
 6  401703.125 12 143693
 6  502007.031 13 143694
 6  602308.594 14 143695
 6  702610.938 15 143696
 6  802914.062 16 143697
```

Figure 9.5: An example of the TDC output text file taken during the SPS test beam. The columns represent (from left to right) channel number, time in nanoseconds, local event counter and total event counter.

Figure 9.5 shows an example of the TDC output text file generated during these measurements. The first column shows the channel number, in this case channel 6*. The second column gives the time of the hit in nanoseconds since the initial reset. The internal clock of the TDC operates at 40MHz and is divided into 32 equal pulses. Hence, each clock output from the

* The numbers 8 and 80 occur only when a start pulse arrived on the start control line of the TDC and do not represent a true channel number. These numbers were inserted into the code to ease the data plotting routines.

TDC represents 0.78125 ns. To convert from number of clock pulses to nanoseconds, the user must multiply the TDC raw counter output by 0.78125 as explained in chapter 8. The third column is an event counter which is reset at the reception of each start pulse. The forth column is an event counter which is only reset at the start of the acquisition.

Close examination of the second column shows that the events input on channel 6 occur roughly every 100000 ns, in line with the time period of the 10kHz waveform present on channel 6 of the TDC. The TDC event counter is 20 bits deep and running at 40MHz will rollover every $(2^{20}-1)\times 0.78125ns = 819.2\mu s$. The counter rollover was detected when the clock output from channel 6 was less than the previous output. In these cases, a value of $819.2\mu s$ was added to the first clock value after the rollover, before the difference between it and the previous one was calculated and plotted. The left hand histogram in figure 9.6 shows the expected peak at $\Delta t = 100\mu s$, the difference between each data value and its previous value. By re-plotting the data with a log y axis, shown in the right hand histogram, more detail can be seen. More peaks occur every $100\mu s$ signaling the occurrence of missed input pulses. For example, if one clock pulse is missed by either the discriminator or the TDC, the time difference between the next one and the previously recorded pulse would be 200 ns. If two adjacent pulses were missed then the time difference would be 300 ns and so on. The data in the right-hand histogram demonstrates that at an input frequency of 10kHz, the discriminator or TDC is missing a single input pulse roughly 0.1% of the time, two pulses roughly 0.1% of the time etc. Also, the noise level is suppressed by 6 - 7 orders of magnitude with respect to the 10kHz signal.

Further measurements are required to determine how the input rate effects the percentage of losses and whether these losses are due to discriminator dead time or TDC buffer overflows.

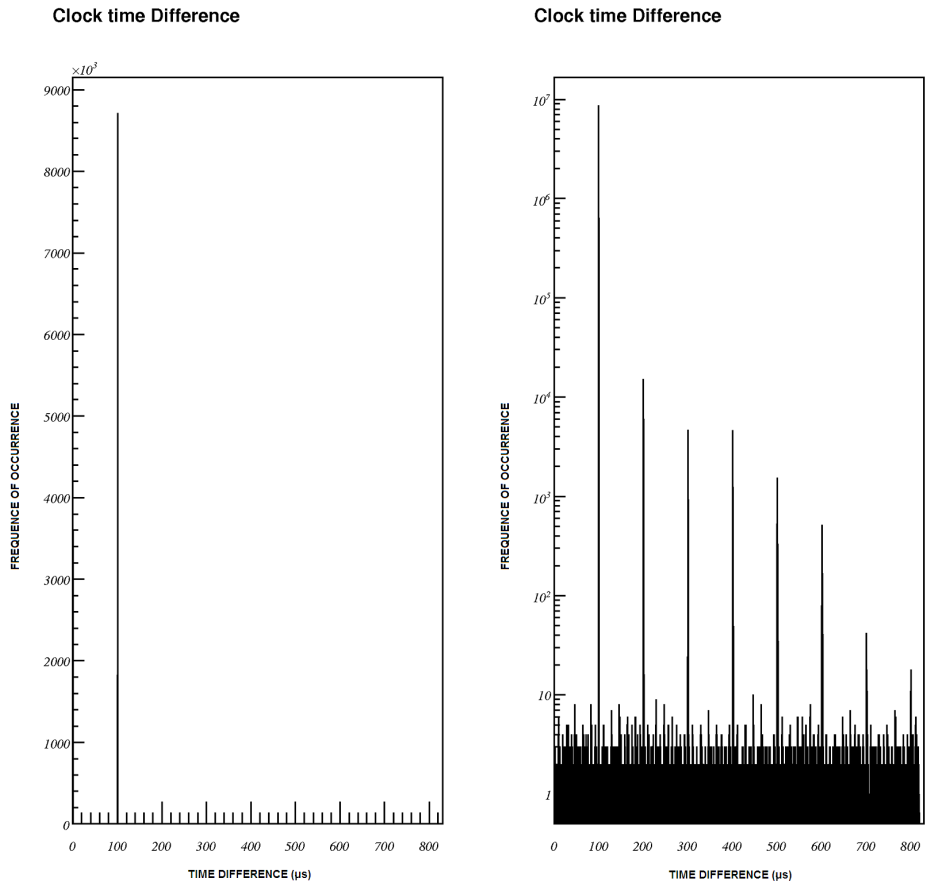

Figure 9.6: The VME output time jitter measured from a 100μs period pulse waveform. The right-hand plot shows the data plotted with a Log(y) axis.

A -1V, 20ns pulse waveform with a period of 100μs was input into four channels of the discriminator. The discriminator thresholds were set to -200mV to ensure all input pulses were selected and a subsequent output

signal sent to the TDC. Theoretically, the TDC should measure all four input signals as arriving at the same time with no inherent offset due to the internal circuitry of the discriminator or TDC itself. A C++ acquisition program was written to record all the timings of the four channels for 1 million pulses. The resulting text file was processed using a ROOT C++ script which looked at the channel numbers and subtracted the channel 2, 3 and 4 event times from the previous channel 1 event time. The results of these calculations are shown in the following two histograms of figure 9.7; one with a linear y axis and one with a logarithmic y axis to enable the low occurrence events to be seen.

The noise signals are displayed only on the positive time axis due to the algorithm used to generate the histogram and the assumption that values read out from the TDC would increase except during a counter roll-over. The algorithm looked at the *n+1* event time and if it was less than the n^{th} event time, a value of 819μs would be added to it. The difference between *n+1* and n event times was then calculated and read into the histogram. In reality, the jitter noise is spread evenly over the x axis. It must be noted that the noise is suppressed by a factor of 10^4.

The internal counter that ultimately generates the hit time information rolls over every 819.2μs. It is important that the TDC counter output always correctly reflects the time information of the input signals. This includes the point at which counter reaches its maximum value and rolls over the continue counting from zero. The data used in the jitter measurements was filtered to only include the lines of data that occurred immediately before and after the rollover points. Histograms of these data, shown in figure 9.8 shows

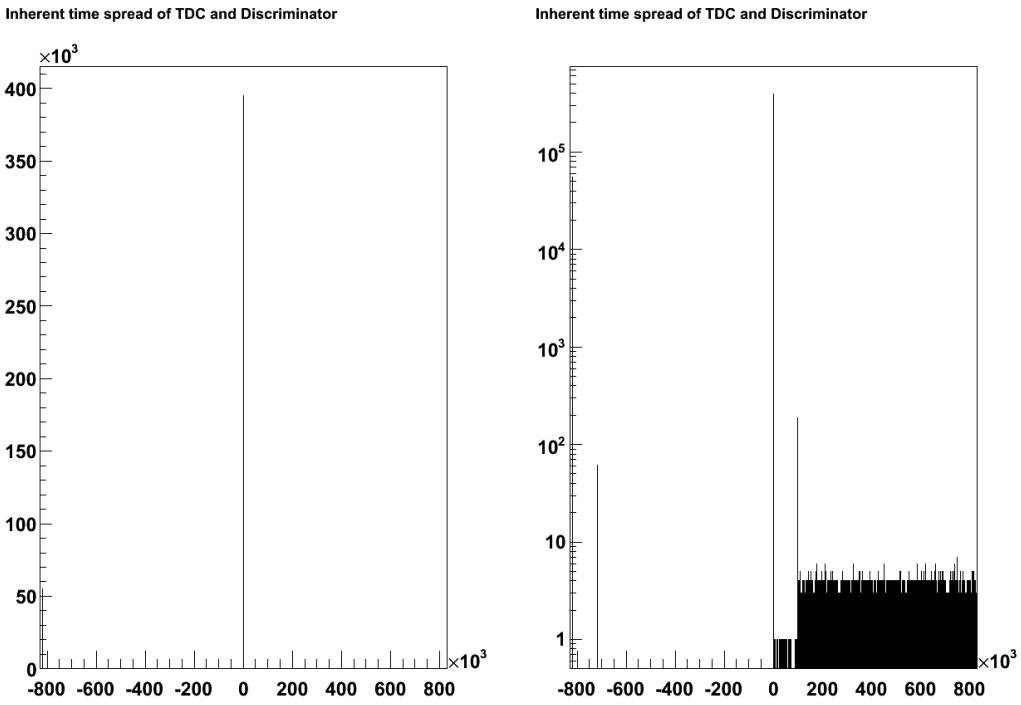

Figure 9.7: Examples of the VME module time jitter due to internal effects of the modules such as bus lines and register reading/writing. The right-hand plot shows the data plotted with a Log(y) axis.

that the counter continues to measure the correct time difference between adjacent pulses even at the rollover point. The Log(y) plot also shows that the TDC or discriminator are missing the occasional input hit measurement as explained earlier.

Overall, the VME TDC and discriminator modules proved to be satisfactory for the rate monitoring readout of the BSC, at least for the initial commissioning stages when hit rates should not be too high. Faster discriminators are available and may replace the present CFD discriminator if the signal rates increase beyond the ability of the current discriminator. The

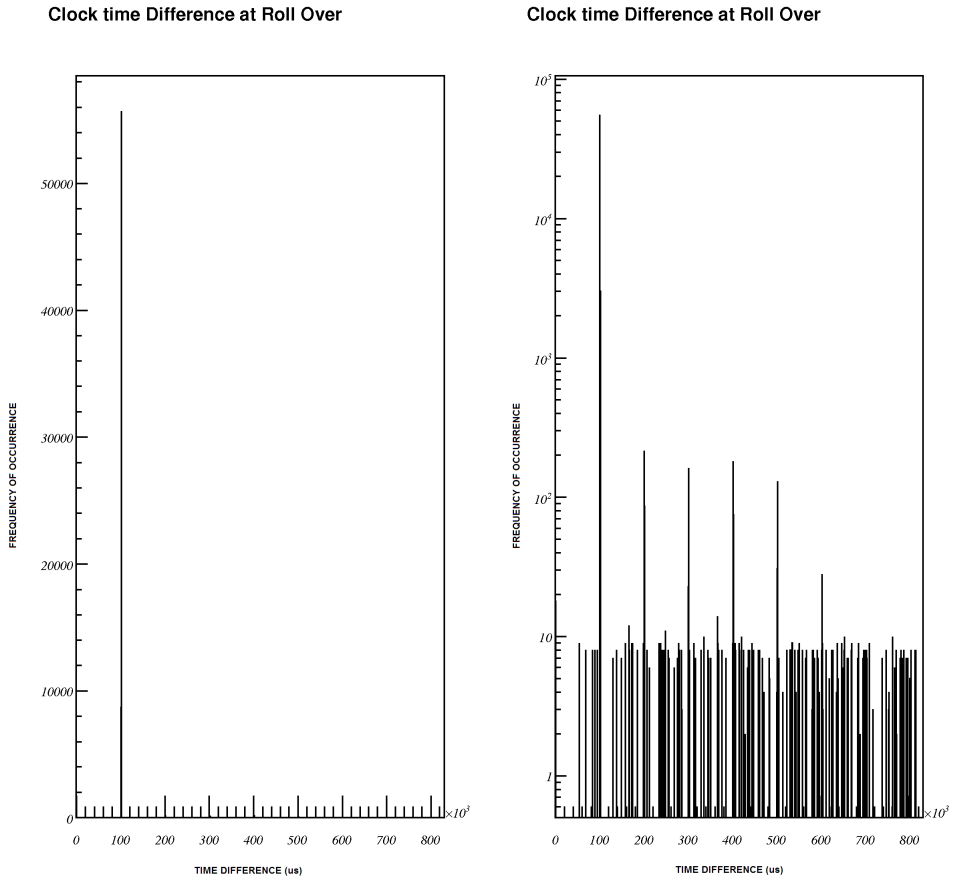

Figure 9.8: The VME output time jitter at the point where the internal TDC counter rolls over measured from a 100μs period pulse waveform. The right-hand plot shows the data plotted with a Log(y) axis.

TDC does not introduce any timing errors when signals arrive at multiple channels simultaneously or during the internal clock roll-over. This is very important as the location of the BSC1 tiles are such that only 2.26ns exist between incoming and outgoing bunches during the LHC commissioning phase B with 75ns bunch spacing. Any loss of time resolution due to the readout system would have serious implications for the BSC1 system.

9.2.2 Time-of-Flight Measurements

The p /π^+ / μ^+/μ^-beam was extracted from the PS accelerator at the T11 junction and was directed at three scintillation tiles labeled Tile A, C and B arranged as shown in figure 9.4. The distance from tile A to C was set at 70cm to provide a 2.33ns time of flight (TOF) similar to the timing expected in the LHC between the outgoing background and collision fragments and the next incoming background particles. The distance between Tile A and Tile B was set at 3.58m, similar to the distance between the BSC1 and BSC2 tiles on each side of the CMS experiment. To be able to distinguish between tiles A and C means that it will be possible to differentiate between incoming and outgoing particles with the BSC1 channels.

With this spacing it was possible to ascertain the competency of the most stringent requirements of the BSC as a solitary system with regards to its timing resolution.

A particle in the beam could pass through the three tiles in turn causing a signal to be seen by the discriminator and TDC. Traveling at c, the time-of-flight between tiles for the particle was calculated. Between tile A and tile C (distance = 68cm) the TOF is calculated to be 2.33ns. Between tile C and tile B, the TOF is calculated to be 9.6ns. Due to beam focusing issues* not all of the particles were guaranteed to pass through all three tiles. This effect produces a large number of spurious peaks in the resulting histograms as time stamp of a particular hit in one tile may not have a time stamp in another tile from which the difference can be calculated.

* The beam was set to be focused on the BCM2 diamond roughly 1m in front of tile A. The beam then diverged from this point.

The TDC was run in continuous mode with a small modification to the code to start and stop the acquisition during the long (30s) breaks of the PS extraction cycle*. A PS cycle generated pulse was used to trigger the TDC acquisition. The pulse was set to arrive $1\mu s$ prior to the start of the PS spill. After 1s, the TDC acquisition was halted by the software at which point it waited for the next PS trigger pulse. During each acquistion, the 400ms spill was recorded on three channels of the TDC. Data was gathered over the course of two days resulting in over 6.9million hits in the three tiles.

Using ROOT[42] software, the time difference between the hits occurring on the three channels was calculated and histogrammed, given in figure 9.9. The same data is displayed with more detail in figure 9.10. Here the mean values of the time of flight between tiles can be seen as well as the spread of the times.

9.2.3 Results of TOF measurements

Table 9.1 provide a comparison between the expected TOF values and the measured results obtained from the PS testbeam.

	B-A	C-A	C-B
Calculated	11.9ns	2.33ns	9.67ns
Measured	12.1ns	2.4ns	10.1ns
σ	4.2	3.1	4.2

Table 9.1: Results of the TOF measurements from the PS test beam and the calculated values.

The mean time of flight measurements agreed closely with the calculated

* This reduced the file sizes by around 90%. The data otherwised gathered during this time would be random cosmic muon events and high amplitude PMT noise.

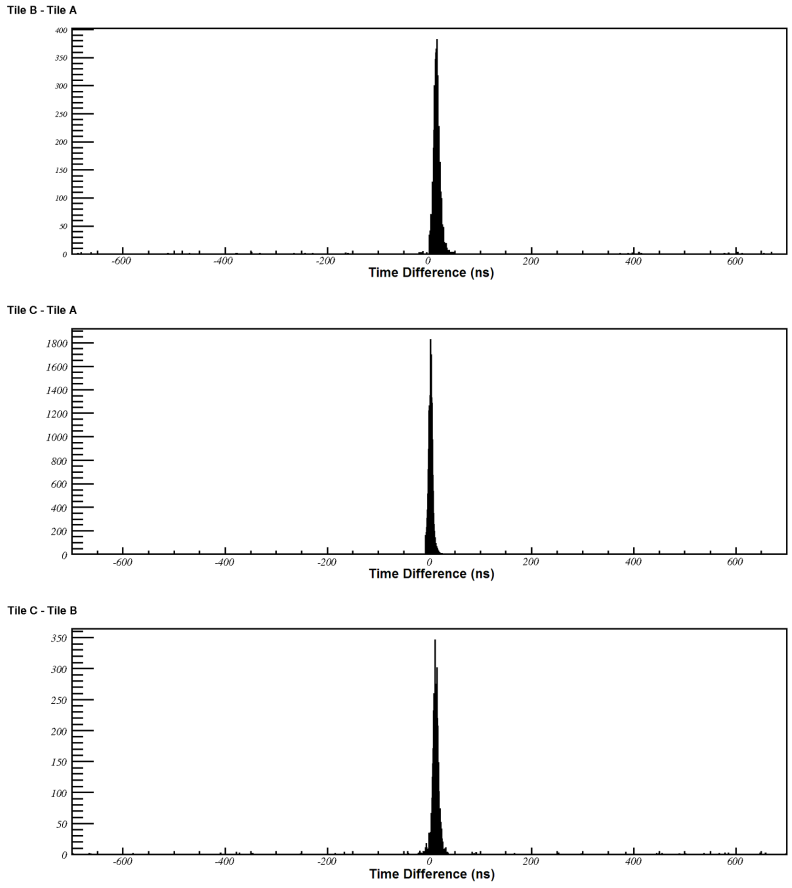

Figure 9.9: The VME output time of flight measured from the PS test beam and three scintillator tiles separated by B - A = 68cm, B - C = 288cm. The upper histogram shows the results of the subtraction of the tile B times (input on channel 2 of the TDC) and the nearest tile A times (input on channel 1 of the TDC). The middle histogram shows the results of the subtraction of the tile C times (input on channel 6 of the TDC) and the nearest tile A times. Finally, the lower histogram shows the time differences between the hits on tile C and the hits on tile B.

values (See table 9.1). Even though the geometry and beam profile were not ideal the results of the time-of-flight measurements agreed with the calculated values to within <1ns. The σ of the spread is a convolution of spread of the two channels combined.

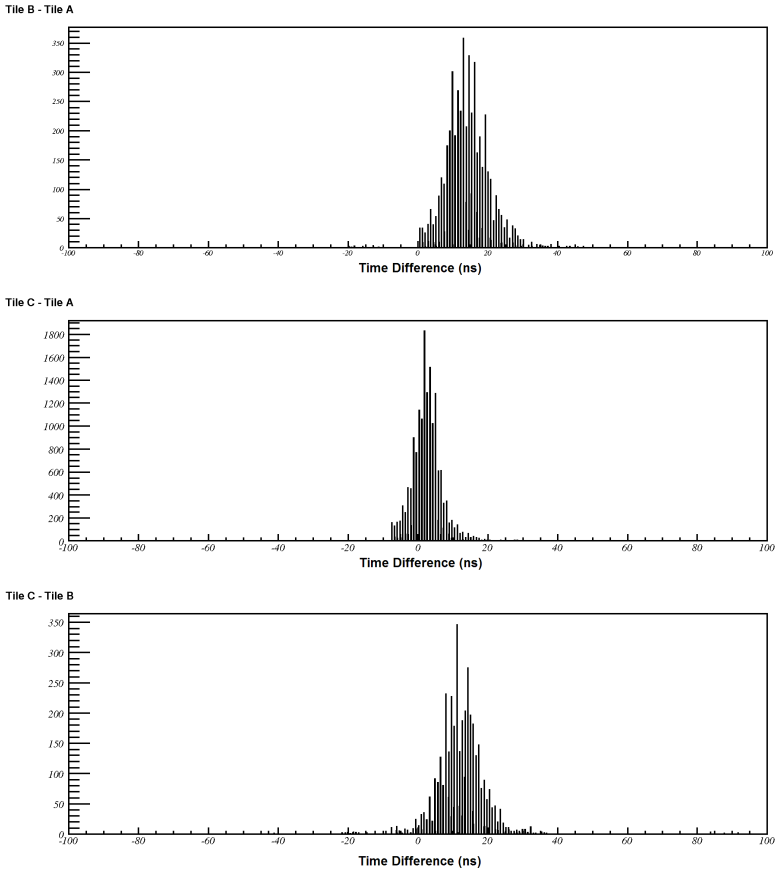

Figure 9.10: The VME output time of flight measured from the PS test beam and three scintillator tiles separated by B - A = 68cm, B - C = 288cm in greater detail. The upper histogram shows the results of the subtraction of the tile B times (input on channel 2 of the TDC) and the nearest tile A times (input on channel 1 of the TDC). The middle histogram shows the results of the subtraction of the tile C times (input on channel 6 of the TDC) and the nearest tile A times. Finally, the lower histogram shows the time differences between the hits on tile C and the hits on tile B.

$$\sigma_{com} = \sqrt{(\sigma_{chA}^2 + \sigma_{chB}^2)} \approx \sqrt{(2\sigma^2)} \tag{9.1}$$

$$\sigma_{chA} = \sqrt{\frac{\sigma_{com}^2}{2}} \tag{9.2}$$

The single channel resolution can be calculated if the assumption is made that each channel (tile, PMT and VME hardware) has the same σ. For example, using equation 9.2 the combined resolution of channel A and channel B is $\approx 3ns$. This is the same time resolution as achieve with the tiles and PM tubes in the OPAL experiment in LEP [20]. These results indicate that even with the current basic readout algorithms, the time resolution will be sufficient for the BSC2 and reasonable for the BSC1. The BSC2 was added to the initial BSC project for the sole purpose of enabling the readout of unambiguous timing data that the BSC1 would possibly not provide. The successful results of the TOF measurements means that the BSC1 and BSC2 readout system performs adequately well.

Chapter 10

Monitoring, Data Networking and Technical Triggering

10.1 Data Networking

The proposed data network for the BSC is shown in figure 10.1. This scheme is designed to be identical to that of the rest of the BRM subsystems.

The Linux rack PC will primarily control data acquisition from the VME crate via an optical VME-PCI bridge card and HAL as described in chapter 8. Efficient post-acquisition processing will be carried out on this PC to ensure the maximum data transfer rates can be achieved while minimizing the risk of VME or PCI bus errors. The raw data will be processed on board the BSC rack mounted PC to produce histogram data and therefore compress the amount of data to be sent to the BRM collector PC. The raw data will be saved on to local disk in a circular buffer regime with new data overwriting the unimportant historical data. In the event of an abort, a post-mortem

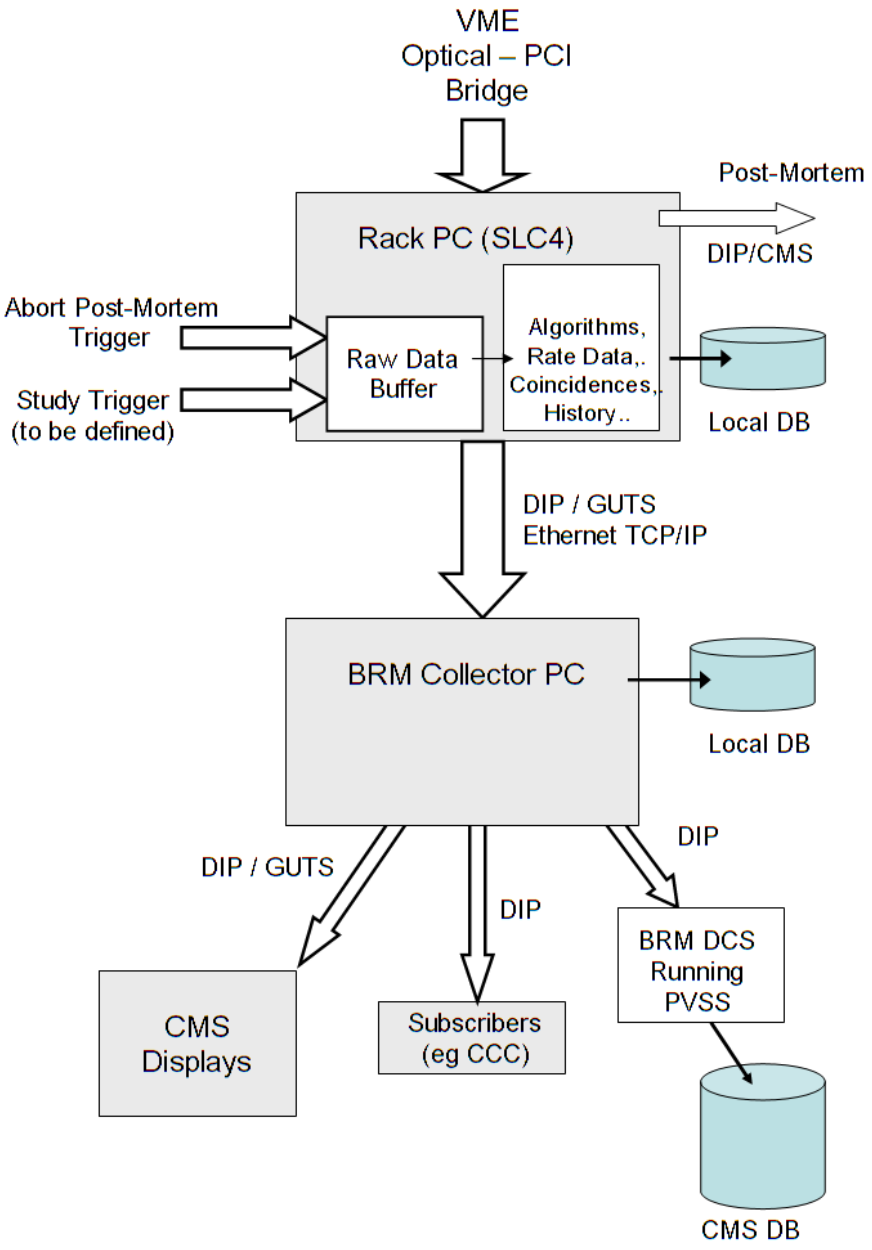

Figure 10.1: A block diagram of the planned data flow from the BSC to the BRM PC and CMS.

trigger will be issued and the most recent historical data can be read out to help determine the beam conditions in the lead up to the abort. A summary of the histogram data will be sent to the BRM collector PC using a TCP/IP publisher/subscriber client protocol such as GUTS* or DIP[6]†. From here, histograms and graphical forms of displaying the BSC data will be produced.

10.2 Display

This section concerns itself with the display of the BSC data, as obtained from the readout as detailed in the previous sections. As the framework for the readout monitoring for the BSC is being developed at the present time, it is not possible to construct realistic templates of the display of the data. However, it is crucial to the design of the display that there is an understanding of how the data might be useful for tuning or understanding beam conditions. Essentially, the display is the most important 'deliverable' of the BSC. The idea of the BSC was inspired by similar monitoring devices from the previous generation of detectors at the LEP, TEVATRON and HERA rings. In all cases these monitoring devices were considered to give a clear insight into the running conditions of the accelerator and were vital in obtaining an understanding of these conditions. Therefore, to demonstrate the BSC data that may be displayed, in the following figures, the ZEUS C5 detector[26] (at HERA) is taken as an example. The quantities derived from the C5 are expected to be very similar to those derived from the BSC data

* Generalized Unilateral Transfer Server, a Java framework that is designed to transfer BRM data from a server to a client PC.

† Data Interchange Protocol. Used for publishing small amounts of real-time data to the relevant subscribers.

(i.e. rates, gated rates, coincidences, z vertex and bunch structure). Similarly in terms of performance, the signals are uncannily similar between the two systems*.

Figure 10.2 below shows an example of how the rates may be presented i.e. history plots of rates against time; examples are shown here of raw rates, and coincidences between particular counters. The snapshot was taken during a period of particularly low loss rates. This figure shows live data; i.e. the data scrolls through as it is received.

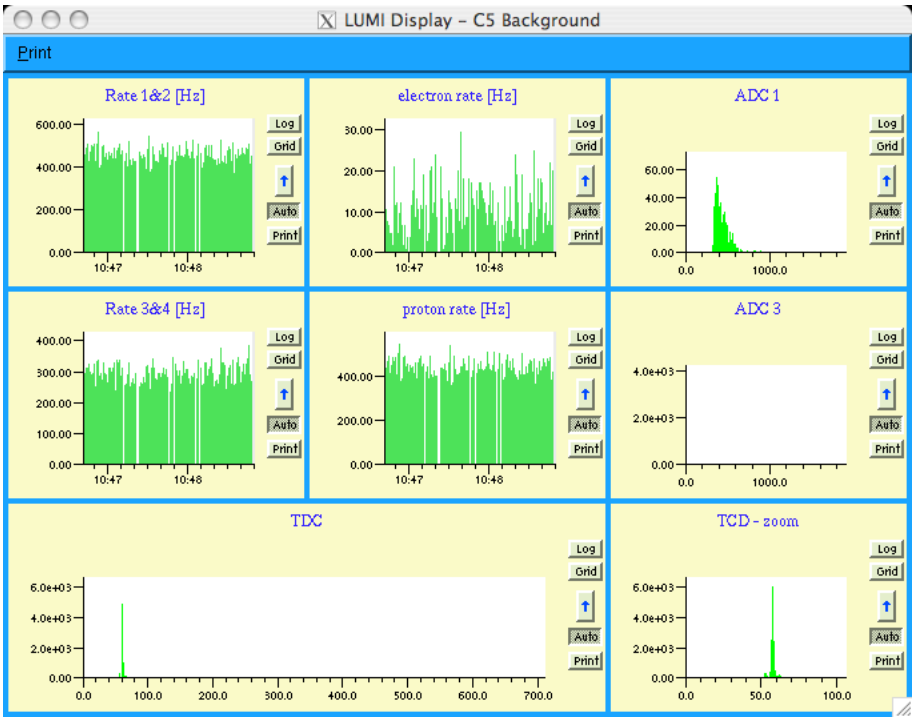

Figure 10.2: An example of the planned display format for the BSC. This example is the display used in the C5 detector in ZEUS at DESY, Hamberg.

Figure 10.3 shows how the hit data summed over may orbits can be used to extract the bunch structure around the machine. 10.3(a) shows the entire

* Richard Hall-Wilton; Private communication.

orbit; 10.3(b - e) are zooms of parts of the full bunch train. A similar display should be possible with BSC hit data. This information is very useful in that it gives a snapshot of the bunch structure of the beams and their losses.

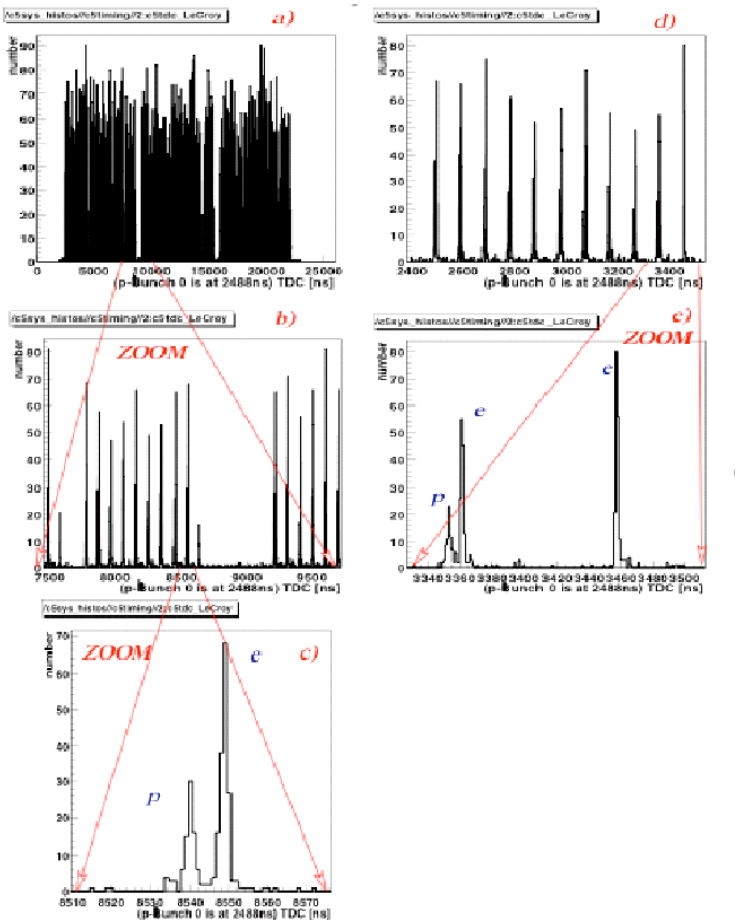

Figure 10.3: An example the bunch train structure for an entire orbit as obtained by the ZEUS C5, and an example as to how the timing resolved the two different beams. All of these histograms are created periodically (every few seconds) from the most recent hit data[26].

Figure 10.4 demonstrates the gating of the electron and proton beams for the ZEUS C5 system [26]. The BSC data is expected to look similar, with the two peaks being incoming background from one beam, and outgoing

background from the second beam plus collision products respectively. The timing difference between these two peaks is determined by the distance from the IP along the beampipe, and by the bunch spacing as detailed earlier. In figure 10.4, similar data is demonstrated to be able to additionally to resolve the satellite proton bunches which may occur in empty rf buckets; this filling of the adjacent RF buckets is possible to occur also at the LHC, with the buckets having a 2.5 ns spacing. The occupancy of these 'empty' buckets is one of the key indications of problems in the LHC RF system as in also one indicator of beam conditions in the early commissioning stages.

The BSC will be able to give information on coasting beam, i.e. the fraction of the beam which has escaped the RF system and is effectively debunched. Coasting beam has been problematic at times both at TEVATRON and HERA and typically develops during a fill and has been as high as 10% - 20%; it is not yet known whether this will occur at the LHC, nor at what fraction.

Lastly, the timing of the peaks from each bunch with respect to the bunch clock and orbit marker can be used to give an accurate measurement of the z position of the vertex (not shown) which is expected to be very useful in the early days of commissioning before the track reconstruction packages are fully understood. The tracker will only be operational if stable beam conditions are present. Information on the beam conditions can therefore be provided before the tracker is turned on, ensuring its safe operation.

Figure 10.5 shows an example of the proposed display for CMS containing BRM and luminosity information. This is foreseen to include rate data and bunch structure information from the BSC.

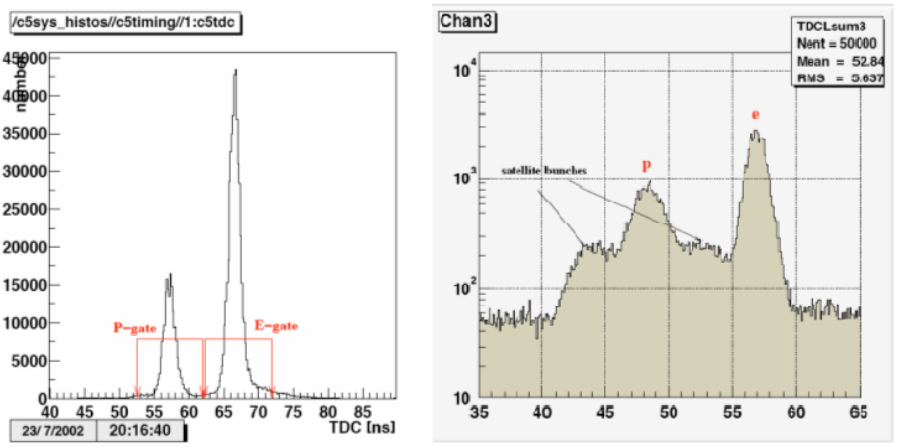

Figure 10.4: Timing spectrum with electron and proton beam. The left-hand-plot shows the gating scheme for gating the 2 different beams. The right-hand-plot shows a similar plot, with a log y axis. Both of these histograms are created periodically (every few seconds) from the most recent hit data [26].

Figure 10.5: Example of the prototype CMS Static Display to be implemented for the BSC data display.

10.3 Technical Triggers

The LHC luminosity is expected to start at $\mathcal{L} = 10^{27} cm^{-2} s^{-1}$ in 2007 and gradually rise to the nominal luminosity of $L = 10^{34} cm^{-2} s^{-1}$ by 2010 [53]. At this nominal operation, it has been calculated that approximately 19 collision events per bunch crossing will occur [29]. The purpose of a trigger system is to enable the particle detector to select events in the presence of background.

A simple trigger system was used in the characterization of the BSC tiles using cosmic muon hits by selecting coincident signals from the telescope tiles (see chapter 7). Unlike the cosmic muon experiments, where the arrival time of particles was random, the arrival time of particles in CMS is known and set by the LHC bunch structure. The recording of each event can be synchronized to the CMS master clock which is in time with the instant of each collision at the interaction point.

The event rates in modern colliders, particularly hadronic (*ep* and *pp*) colliders are very high requiring a trigger system with greater selectivity. Many of the interactions that will occur in the LHC have relatively large cross-sections compared with those involving possible Higgs mechanisms or symmetry breaking. Consequently, these interactions have been well studied by previous experiments and are considered as part of the physics background in CMS and the other LHC detectors. These background events must be excluded by the trigger system and only the interesting, typically low-cross section processes are recorded for further investigation. The selectivity or *bias* of the trigger algorithms must therefore be designed in a way which will minimize the data storage of background events but should not be heavily

biased in such a way that only 'searched-for' signatures are selected and that its acceptance for physics can be determined. A biased trigger could prevent the discovery of new unexpected processes. For this reason, trigger systems in experiments such as CMS are designed with several levels of selectivity. The amount of data is reduced through each level until only events of interest remain. The BSC is to be used to provide up to six technical triggers to the global triggering group. Four of these triggers are intended for beam halo; the remaining two are for minimum-bias event triggering.

In consultation with the CMS Trigger group, the following trigger schemes from the BSC detectors.

1. Logical OR of coincidences between opposing ($+z$ and -z) inner ring scintillator tiles with gating to select $+z$ going particles in time with the beam.

2. Logical OR of coincidences between opposing ($+z$ and -z) outer panel scintillator tiles with gating to select $+z$ going particles in time with the beam.

3. The logical OR of the output of the previous two triggers.

4. Same as 1 above but gating to select -z going particles.

5. Same as 2 above but gating to select -z going particles.

6. The logical AND of true, non-delayed coincidences between opposing scintillator tile hits. $\geq n$ channel hits create a trigger output where n is adjustable. Here, the signals are produced by particles originating from the I.P.

The trigger logic is being implemented using the NIM modules described in section 8.2 of Chapter 8. Taking coincidences from opposing tiles only, greatly simplifies the implementation of the halo trigger. The signals from the PMT arrive at the NIM crate in the S1 counting room via the VME V812 constant fraction discriminator as ECL level signals. After conversion in to NIM standard, the signals from opposite corresponding tiles are sent to a coincidence module with a short (3ns) window. The signal from the -z tile is delayed by 72.7ns* minus the inherent delay time of the cabling along this route. In this case, signals from a particle traveling from $+z$ to -z will arrive in coincidence and generate a trigger pulse indicating both the existence of beam halo and its direction. Similar logic with the delay in the $+z$ route to detect -z to $+z$ traveling beam halo will also be assembled. Figure 10.6 shows a block diagram of the beam halo logic for the technical trigger readout.

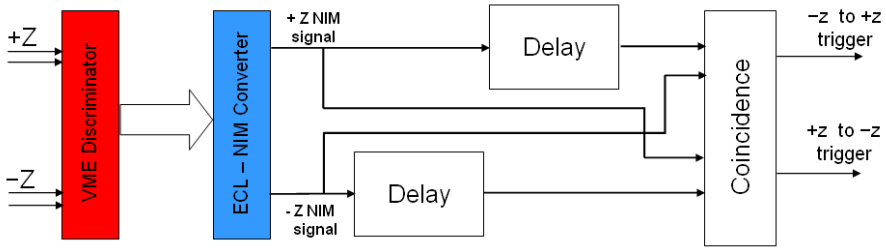

Figure 10.6: The halo muon trigger logic for the BSC technical trigger. The $+z$ and -z signals arrive from the VME V812 constant fraction discriminator as ECL signals. After converting to NIM, the signals are connected to the coincidence module with in-line delays to determine the direction of the halo muons.

The time-of-flight for halo muons passing through the 21.82m between the opposite ends of the BSC1 detector is 72.7ns. Therefore, to ensure the

* The time of flight for a particle traversing the 21.82m of the detector.

signals arrive at the coincidence module simultaneously, a delay of 72.7ns minus the delay of the other cabling is required. Also, a narrow time window of $\leq$ 3ns is needed for coincidence acceptance. When coincidence hits from the opposite corresponding channels have generated a halo trigger, it will be necessary to know the approximate locations from where the halo muons originated. The cross-sectional area of the BSC tiles is relatively large; from 489 - 823 $\text{cm}^{-2}s^{-1}$. Any beam halo muons which manage to traverse the CMS detector must have enormous energies and therefore it is safe to assume they will be undeflected from one side of the BSC to the other. If a halo muon from a beam gas event was to traverse any two opposite end tiles of the BSC detector, there is a minimum calculable distance from where it could have originated, based on simple geometry and trigonometry.

Assuming that any halo muons stemming from a beam gas event travel radially from the point of interaction, the minimum distance in Z can be estimated by taking the minimum and maximum radial distances of the BSC tile segments as shown in figure 10.7 which demonstrates the calculation for the inner annulus tiles for a -z to +z traveling halo muon.

The minimum radius of the inner annulus tiles is 200mm. The maximum radius of the inner annulus tiles is 420mm. The distance between the +z and -z tiles is 21820mm. From these values, the maximum angle of the halo particles with respect to the beam pipe is;

$$\theta = arctan(\frac{220mm}{21820mm}) = 0.014^{\circ} \tag{10.1}$$

and the minimum distance from the I.P to the origin of the beam gas

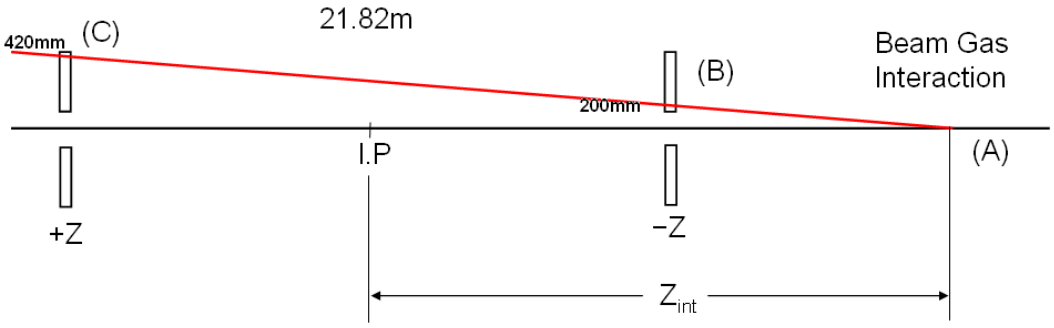

Figure 10.7: A beam gas event occurring at (A) may produce muons which pass through the minimum radial point of the -z BSC inner annuls tile (B), through the CMS detector and out via the maximum radial point of the opposite corresponding BSC inner annulus tile (C). The distance between the tiles is 21.820m. A minimum interaction distance, Z_{int} can be calculated using trigonometry.

interaction is;

$$Z = \frac{310mm}{tan\theta} = 30.75m \rightarrow \infty \tag{10.2}$$

where 310mm is the distance of the traversing particles above the I.P.

Any particle which traverses both corresponding tiles across the length of the detector could have originated from a minimum distance of 30.75m from the I.P. Similar calculations for the paddle tiles give a result of $Z_{int} = 70.86$m. Table 10.1 shows the range of distances from which the halo muons are likely to have originated, depending on whether they pass through corresponding disk-to-disk, paddle-to-paddle or from disk-to-paddle.

Obviously, any halo muons that are produced at distances much greater than these would travel almost parallel to the beam pipe. There is no way of determining the exact distance to their origin. However, if coincidence hits are being seen in the inner annulus tiles but not in the outer paddles

Traversed Tiles	Probable Distance to Origin from I.P
Disk-to-Disk	30.7m $\rightarrow \infty$
Paddle-to-Paddle	70.9m $\rightarrow \infty$
Disk-to-Paddle	17.5m $\rightarrow$ 31.7m

Table 10.1: The probable distances from the I.P that the beam halo originated dependent on the tiles of the BSC1 that the particles traverse from one end of the detector to the other. The trigonometric calculations assumed that all particles are of very high energies and will travel almost undeflected through the detector and that the beamline is straight, centred on $x = y = 0$.

it is likely that the origin of the particles lies somewhere between 30 - 70m from the I.P. Consideration of this could be extremely useful information for troubleshooting the LHC vacuum sections and halo losses on the beampipe near the CMS detector.

Chapter 11

Conclusions & Outlook

The beam scintillator counter is a small but vital component of the CMS detector which will provide possibly the most important data for CMS in the very early stages of commissioning. Additionally, several large and complex sub-detectors such as the inner tracker, need to use the triggering capabilities of the BSC for the track based alignment procedures. Data on the halo and collision fragment rates will be made available from the BSC readout systems that in turn can be used to troubleshoot the LHC beam conditions in and around the CMS cavern. Other BRM systems will take over this role once the LHC luminosity has been increased to sufficient levels for these detectors to be sensitive.

Hadronic & Muon Rates

The BSC, being the most sensitive detector of the BRM group, will be the sole device capable of generating beam halo, minimum-bias and hadronic rate data throughout Stage A and Stage B of the LHC commissioning.

Commissioning Stage A ($\mathcal{L} = 10^{27}$) is scheduled to run for 44 days. The time requirements for Stage B are not yet defined. However, the signal hit rates will be sufficiently low that the BSC will be able to generate clean, unambiguous data. The expected halo hit rates are 490Hz for the BSC1 inner and BSC2 tiles and between 55 - 82Hz for the BSC1 outer tiles for the Stage A luminosity of $\mathcal{L} = 10^{27}\text{cm}^{-2}\text{s}^{-1}$. During Stage B, these rates are expected to increase to $4.9 \times 10^{7}\text{s}^{-1}$ and between $5.5 - 8.3 \times 10^{6}\text{s}^{-1}$ respectively; the BSC readout was designed to cope with these rates.

BSC Tile Geometry & Timing

The locations of the BSC1 tiles on the HF front faces were not the optimum position with regards to timing. With a bunch spacing of 75ns, the Δt between incoming background particles and outgoing background + collision fragments is calculated to be 2.26ns (refer to section 5.1.1). This value remains for the bunch spacing of 25ns. The BSC2 tiles at z = ±14.46m, were incorporated into the design to remove the timing ambiguity, particularly for the 75ns bunch spacing operation throughout commissioning Stage B. These tiles provide a Δt of 20.7ns at 75ns spacing and 4.27ns during the nominal 25ns bunch spacing (refer to table 5.4). The results of the PS time of flight measurements (refer to section 9.2) showed a timing resolution of 3ns for the BSC front-end hardware and readout, sufficient for differentiating the incoming particles from the outgoing particles. The geometry of the BSC1 presents an active surface area of approximately 1.2m^2 and the inner annulus tiles encompassing the beam-pipe gives a pseudo-rapidity range of $3.9 < \eta < 4.4$.

Hardware Tests

Each component of the BSC hardware has been tested and the operational characteristics measured to provide information that predicts the performance and functional parameters of the detector once they are installed into CMS. The front-end hardware installed in the UXC cavern will be in a harsh environment. It will be exposed to high levels of radiation, EM noise and potentially a high ambient helium background which can potentially inflict fatal damage to the photomultiplier tubes. The hardware will also need to function correctly in proximity to the CMS magnetic field.

The polyvinyl toluene (PVT) scintillator tiles had previously be employed in the OPAL experiment at LEP [20] where, together with the PM tubes they gave a time resolution of 3ns. It is not possible to quantify the amount of radiation damage already sustained by each individual tile segment but measurements explained in Chapter 7, sections 7.1 and 7.4 showed that most of the tiles are functioning sufficiently well to incorporate into the BSC detector. The results of the signal characterization measurements confirmed that, at the correct PM tube bias voltages, a spectrum of the cosmic muon energy deposited within the tiles can be seen. A separation of the muon signals and the PM tube noise would occur above a certain bias voltage specific to each tile/tube pair. These bias voltages were measured and recorded as the minimum operating voltage for each PM tube shown in Chapter 7, table 7.2. Higher PM tube bias voltages will be used to ensure a good spread in the energy spectrum and a large separation between the particle induced signals and the electronic noise.

CMS will house the world's largest superconducting magnet. The stray field from this magnet will have an effect on many devices if they are not properly shielded or installed in the correct orientation with respect to the field. The PM tubes of the BSC are one such device which are extremely susceptible to magnetic fields. Special attention was paid to researching the effects on the PM tube signals, simulating the magnetic field in the potential installation areas and ensuring that the mechanical structures holding the PM tubes can be adjusted to compensate for any differences in field strength or direction of the expected magnetic field. The HF calorimeters, having a large steel content, provide some shielding from the magnetic fields if the PM tube boxes are installed close enough to the bulk structure. Simulation studies showed that the magnetic field strength should be approximately 170G and with an almost constant $\frac{dx}{dy}$ (radial direction in the x/y plane). i.e. The angle of incidence of the magnetic field on the PM tube will be almost constant and at 90°if the PMT boxes are mounted correctly. The measurements performed on one of the PM tubes proved that they can operate up to a maximum $\overrightarrow{B}$ field of approximately 950G with the field perpendicular to the central axis of the PM tube and μ-metal shielding correctly fitted. The tube was extremely sensitive if placed close to parallel with the field. For this reason and the possibility of discrepancies between the simulation field results and the real magnetic field, the brackets that hold the PM boxes in position were designed to allow a large range of tilt and rotation.

Magnetic field tests were also performed on a INEO cooling fan tray which was a proposed solution to the airflow problems within the BRM electronics

rack in the UXC. Although this model of fan tray maintained operation within a vertical magnetic field of <3000G, it was very sensitive to magnetic fields from any other orientation and proved to be unacceptable for use in the vicinity of the CMS magnetic field (refer to section 7.5).

Test Beam Results

Perhaps some of the most important results are those from the PS test beam time-of-flight measurements. Three scintillator tiles were positioned in line with the PS proton-pion test beam at the T11 beamline and the signal timings recorded using the VME discriminator and TDC modules. Despite the non-optimum beam profile of the T11 beam line, the results confirmed that the timing resolution is close to 3ns, the same as in the OPAL experiment (refer to 9.1). Further tests of the VME discriminator, TDC and VME-PCI bridge showed that there was no inherent time spread due to these modules. Development of the readout system is continuing to optimize the readout rate of the VME modules and account for all possible time uncertainties of the TDC and discriminator. A fast ADC is currently being investigated which will form part of the BSC readout, providing information of the pulse shapes and amplitudes from the scintillator tiles and PM tubes.

Contribution of the BSC to CMS

Initially, the LHC will operate with very low bunch occupancy ($<10^{10}$ protons per bunch) and with only a single bunch traveling in each direction. The luminosity at the interaction points will be of the order of $\mathcal{L} = 10^{27}\text{cm}^{-2}\text{s}^{-1}$. The simulation studies[54, 56] of muon and hadron fluxes in CMS suggest

a muon flux of approximately 7000s^{-1} and 6.3×10^{9}s^{-1} through the entire area of the BSC1 during nominal running. i.e. 25ns bunch spacing, 14TeV center of momentum energy and $\mathcal{L} = 10^{34}$. During the initial single bunch phases, the hadronic flux and muon flux rates are likely to be several orders of magnitude below these values. With the ability to detect single minimum-ionizing particles, the BSC detector will be sensitive to these very low particle fluxes and will be extremely useful in measuring these particle fluxes and 'seeing' the beam conditions until and beyond the time that the flux intensities are high enough to be within the sensitivity range of the BCM diamonds.

Even after the Stage A and Stage B commissioning phases, the BSC will supply at least six technical triggers to the Global Trigger based on time-of-flight gating between combinations of detector panels on opposite z ends of the BSC (refer to section 10). These triggers will aid in the track base alignment procedures of other large scale detectors such as the central tracker and could also provide some clue as to the point of origin of beam halo muons that pass through the 21.8m of the CMS detector depositing energy in the BSC tiles on both ends. The BSC trigger system will also generate a minimum-bias trigger based on a selected number of tiles hit by particles originating from the IP. No doubt further uses of the BSC detector will surface once the LHC and CMS commissioning work commences.

Commissioning & early data

Installation of the BSC has recently begun. All items of equipment are already 'in hand'. The immediate aim is to have one complete section of

installed (PMT box, 9 PM tubes, optical fibers, LED fanout and scintillator tiles) so that any unforeseen problems can be rectified before proceeding with the other three quadrants. Measurements of the cosmic background rates in the UXC will then be made and compared with the simulation studies[55].

Limitations & Upgrade of the BSC

The initial BSC is only a commissioning device; the operation of the current BSC will diminish once the plastic scintillator tiles begin to show degradation from radiation damage, probably during the second year of LHC running. Also, the front-end hardware will not cope with the high hit rates expected during nominal operation of the LHC. In previous colliders such as LEP, Tevetron and HERA, scintillation counter devices have proved to be an invaluable sub-system, providing clear, unambiguous information on the running conditions of the accelerator.

It can be foreseen therefore, that a BSC upgrade will be desirable by CMS for operational purposes. The upgrade will require the replacement of the scintillation tiles in favor of more radiation tolerant materials compared to the BC408 plastic tiles currently used. Research of the radiation hardness and mechanical robustness of available materials will be required to find the most appropriate detector medium for the BSC upgrade.

One of the current limitations of the BSC design was the imposed z position due to available installation locations for the tiles. The position of the main bulk of the tiles means that there will only be 2.26 ns between incoming and outgoing particle bunches. With the ability to design the tile geometry from scratch, the BSC upgrade detector positions could be chosen

to give a greater time between particle bunches, giving less ambiguous results. Similarly, the time resolution of the readout can be improved from the present few ns, to less than 1ns by the employment of more modern, off the shelf detector materials. Additionally, the tile areas can be chosen to produce particle hit rates at full luminosity which are within the range of modern readout hardware.

The BSC presently uses photomultiplier tubes to convert the scintillator light signals to electrical signals and send them to the S1 counting room. The use of PM tubes in the outlying areas of the CMS magnet is troublesome. The upgrade should use a different method of signal conversion which is not affected by the CMS magnetic field. One possibility is the use of photo-diodes (Hybrid Photo Diodes or Avalanche Photo Diodes). These small semiconductor devices are much faster than traditional photomultiplier tubes and could be embedded within the new detector tiles to reduce the complexity of the system. Tests to determine the efficiency, radiation hardness and expected lifetime of the photo-diodes and the related amplifier circuitry will need to be performed.

In addition, new pixel detector ASICs such as the Medipix IC[30] could provide interesting information on the types of particles hitting the detector as well as their energy deposits and quantity. Combined with the timing information gathered from the BSC upgrade, a complete measurement of the beam halo, collision fragments and hadronic particles passing into and out of the CMS experiment can be obtained.

Acknowledgements

My wife, Rati and cat, Mir for their unwavering support and patience during a very difficult year.

Richard Watts for his supervision and support and ensuring my degree stayed on track with the University of Canterbury.

Richard Hall-Wilton & Alick Macpherson for day-to-day support and sharing their vast knowledge and experience.

Emmanuel Tsesmelis & Christal Paris for day-to-day support and financial assistance.

Phil Butler for financing me through the use of the TEC grant and for his valuable advise throughout the year.

Jenny Williams for introducing me to CERN and for her organization skills throughout 2006 - 2008.

David Krofcheck for providing flights and accommodation expenses during my initial visits to CERN.

The BRM group for help with various sections of the BSC design and installation.

Roland Rey-Mermier for use of his magnet test facility.

Adrian Folley for use of the scintillator laboratory and guidance with optical

fiber handling.

Martin Gastal for ensuring all installation work was entered into the UXC schedule.

Martin Wensveen for mechanical engineering support in the UXC.

Rob Knegjens for his excellent work with HAL during his stay as a summer student.

Mark Hashimoto for his extensive data gathering of the tile characteristics before and during the SPS test beam.

Dawn Hudson for administrative assistance.

David Mcfarlane for advice on gas systems and piping

Slava Klyukhin for his help with the CMS magnetic field modeling.

Nathalie Bleesz-Griggs for frequent help in cutting the CERN red tape.

Jean-Paul Chatelain for his fast and precise mechanical engineering skills.

Dmitry Druzhkin & Marco Oriunno for BSC mechanical integration and planning.

Emile Sabin for many various CAD designs and drawings.

Andre Coin for BSC2 CAD drawings and modifications.

Bibliography

[1] A. Macpherson. Beam Condition Monitoring and radiation damage concerns of the experiment. *Proceedings LHC Project Workshop, Chamonix XV (2006) 198.*, 2006.

[2] A. S. Bedder *et. al.*. Cerenkov light generated in optical fibres and other light pipes irradiated by electron beams. *Phys. Med. Biol.*, 37 Number 4:925 – 935, 1992.

[3] A.J Bell, R.J Knegjens *et al.* CMS Beam Scintillator Counter VME Readout. *CMS Internal Note.*, 2007.

[4] B. Dehning et al. The Beam Loss Monitor system. *Proceedings of the XIII LHC Project Chamonix Workshop, Chamonix.*, 2004.

[5] B. Dehning et al. The Beam Loss Monitor system. *Proceedings LHC Project Workshop, Chamonix XIII.*, 2004.

[6] BRM Interface Group. Interface Software DIP webpage. *http://hep.phys.utk.edu/BRM_Interface/index.php/Interface_Software_DIP*, 2007.

[7] C. Zamantzas. The real-time data analysis and decision system for particle flux detection in the LHC accelerator at CERN. *Brunel University, PhD Thesis. CERN-THESIS-2006-037*, 2006.

[8] CAEN Nuclear Ltd. CAEN V767 128 channel TDC Module. *http://www.caen.it/nuclear/product.php?mod=V767*, 2003.

[9] CAEN Nuclear Ltd. CAEN V812 Constant Fraction Discriminator VME Module. *http://www.caen.it/nuclear/product.php?mod=V812*, 2005.

[10] CAEN Nuclear Ltd. CAEN A1535N Floating HV power supply. *http://www.caen.it/nuclear/product.php?mod=A1535*, 2007.

[11] CAEN Nuclear Ltd. CAEN SY1527 Universal Multichannel Power Supply System. *http://www.caen.it/nuclear/syproduct.php?mod=SY1527*, 2007.

[12] CERN. CERN Home Page. *http://www.cern.ch*, 2008.

[13] CERN Press Release. CERN celebrates 40th Anniversary. *http://press.web.cern.ch/press/pressreleases/Releases1994/PR11.94E40thAnni.html.*, 1994.

[14] C.Schwick. HAL User Manual. *http://cmsdoc.cern.ch/cschwick/ software/documentation/HAL/manual/HALUsersGuide.pdf*, 2008.

[15] D. Chong et al. Validation of synthetic diamond for a Beam Condition Monitor for the Compact Muon Solenoid Experiment. *IEEE Trans. Nucl. Sci.*, 54:182, 2004.

[16] E. Gschwendtner *et al.* Beam Loss Monitoring for the LHC. *CMS Internal Note*, 2001.

[17] E. Radermacher. The Compact Muon Solenoid. *EP Division CMO Group (EP/CMO)*, 2001.

[18] Electron Tubes Ltd. PMT Data Sheet. *http://www.electrontubes.com/pdf/9902B.pdf*, 2007.

[19] Ulrich Feltzmann. CMS Conventions. *https://twiki.cern.ch/twiki/bin/view/CMS/CMSConventions*, 2008.

[20] G. Aguillion *et. al.* Thin Scintillating Tiles with High Light Yield for the OPAL Endcaps. *Nuclear Instruments and Methods in Physics Research A 417 (1998) 266 277*, 1998.

[21] H. Bichsel. Passage of Particles through matter. *pdg.lbl.gov/2007/reviews/passagerpp.pdf*, 1982.

[22] M. Huhtinen. Radiation Environment in CMS UXC. *CMS Technical Note. CMS TN/95-198*, 2003.

[23] J. Christiansen, V.Bobillier, R. Frey. Grounding, Shielding and Power Distribution in LHCb. *CERN EDMS Document: EDMS 584310*, 2005.

[24] J. Lazo-Flores. CMS BRM Overview. ..., 2007.

[25] J.Christiansen. 32 Channel General Purpose Time to Digital Convertor. *CERN/ECP-MIC Note.*, 1997.

[26] Julia Furletova. Search for Exotic Processes in Events with Large Missing Transverse Momentum in ZEUS at HERA. , 2004.

[27] Kuraray Co. Ltd. Y11-200 Data Sheet. *http://www.kuraray.co.jp/en/*, 2005.

[28] L. Torrisi. Radiation damage in polyvinyltoluene (PVT). *Radiation Physics and Chemistry*, 63:63 (2002) 8992, 2002.

[29] LHC Data Group. Beam Parameters and Definitions, Chapter 2. *http://ab-div.web.cern.ch/ab-div/Publications/LHC-DesignReport.html*, 1, 2007.

[30] M. Campbell, X Llopart et al. The Medipix Homepage. *http://medipix.web.cern.ch/MEDIPIX/.*, 2007.

[31] M. Fuerstner, I. Brunner, *et. al.* First Calibration of Alanine and Radio-Photo- Luminescence Dosemeters To A Hadronic Radition Environment. *IEEE*, 2005.

[32] Mika Huhtinen. Possible consequences of LHC beam losses for CMS. *LHC Machine Protection Working Group*, 2003.

[33] Mika Huhtinen, Nikolai Mokhov,Sasha Drozhdin. Accidental Beam Losses at the LHC and impact on CMS tracker. *CMS Tracker General Meeting*, 1999.

[34] Mike Lamont. LHC Commissioning Home Page. *http://lhc-commissioning.web.cern.ch/lhc-commissioning/*, 2007.

[35] M.M. Hashimoto, A.J Bell *et al.* BSC Scintillator & PMT Characterisation. *CMS Internal Note.*, 2007.

[36] P.Collier. Baseline Proton Filling Schemes. *LHC Project Workshop - Chamonix XIII*, 2004.

[37] Q. Ingram. The Lead Tungstate Electromagnetic Calorimeter of CMS. *IEEE transactions on Nuclear Science.*, 52, 2005.

[38] R. C. Powell, L. A. Harrah. Nonlinear Responses of Poly(vinyl toluene) Plastic Scintillators at High Excitation Doses. *Journal of Chemical Physics, August 15, 1971 – Volume 55, Issue 4, pp. 1878-1884*, 1971.

[39] R. Hall-Wilton. Beam and Radiation Monitoring Systems. *CMS NIM paper*, 2007.

[40] R. Hall-Wilton, A.L. Macpherson, *et al.* BRM Report for CMS Management Board Meeting. *CMS Management Board Meeting, Sept 2007*, 2007.

[41] R. Schmidt et al. Beam interlocks for LHC and SPS. *Proc. Conf. ICALEPS (2003) Gyeongju, Korea.*, 2003.

[42] Rene Brun, Fons Rademakers. ROOT. An object-orientated data analysis framework. *http://www.root.cern.ch.*, 2008.

[43] R.M. Sternheimer et al. Density effect for the ionization loss of charged particles in various substances. *Phys. Rev. B26, 6067*, 1982.

[44] R.M. Sternheimer *et. al.*. Density Effects for the Ionization Losses of Charged Particles in Various Substances. *Phys. Rev B.*, 26 Number 11:6067, 1982.

[45] S. Müller. Strahlmonitore aus diamant fuer teilchenstrahlen hoher intensitaet. *Karlsruhe University, Thesis*, 2006.

[46] Saint Gobain Crystals. BC408 Data Sheet. *http://www.detectors.saint-gobain.com/home.asp*, 2005.

[47] Saint Gobain Crystals. BCF91A Data Sheet. *http://www.detectors.saint-gobain.com/home.asp*, 2005.

[48] Slava Klyukhin et al. Magnetic Field for CMSSW. *https://twiki.cern.ch/twiki/bin/view/CMS/MagneticField/Magnetic_Field_Data.*, 2007.

[49] Matt Hollingsworth Steffan Spanier. GUTS - A Generalized Unilateral Transfer Server. *CMS Internal Note. CMS IN-2008/005* , 2008.

[50] T. Aumeyr *et. al.* BPTX Design Report for CMS. *CMS Internal Note 2007/XXX*, 2007.

[51] T. Han, D. Rainwater, D. Zeppenfeld. Drell-Yan plus missing energy as a signal for extra dimensions. *Physics Letters B*, 463:93 – 98, 1999.

[52] T. Lampén. General alignment concept of the CMS. *Nuclear Instruments and Methods in Physics Research A.*, 566:100 – 103, 2006.

[53] The CMS collaboration. CMS Technical Design Report, Volume II: Physics Performance. *Journal of Physics G*, 34 Number 6, June 2007.

[54] V. Drollinger. . Simulation of Beam Halo and Cosmic Muons. *CMS Internal Note CMS 2005/12.*, 2005.

[55] V. Drollinger. Simulation of Beam Halo and Cosmic Muons. *CMS NOTE 2005/012*, 2005.

[56] V. Drollinger *et. al.* Trigger and Reconstruction Studies with Beam Halo and Cosmic Muons. *CMS Internal Note.*, 2005.

[57] V.Ryjov *et. al.*. CMS BRM Grounding & Shielding. *Presentation to the CMS Grounding Workshop.*, 2008.

[58] W. de Boer et al. Radiation hardness of diamond and silicon sensors compared. *Physica Status Solidi A* , 204:3004, 2007.

[59] W.M. Yao *et. al.* Review of Particle Physics. *Journal of Physics G*, 33:1+, 2006.

[60] W.R. Leo. Techniques for Nuclear & Particle Physics Experiments. *Springer-Verlag: ISBN 3-540-57280-5*, 1994.

APPENDIX I

Figures 1.1 through to 1.20 show the PM tube gain vs. bias voltage for all of the available PM tubes of the BSC. The exponential portion of each curve suggests the correct operating range for each tube.

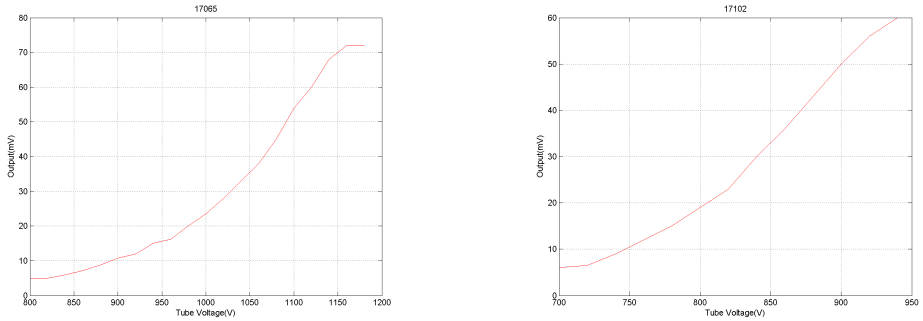

Figure 1.1: PMT Gain vs. HV supply curves. This is shown for PMT17065 and PMT17102.

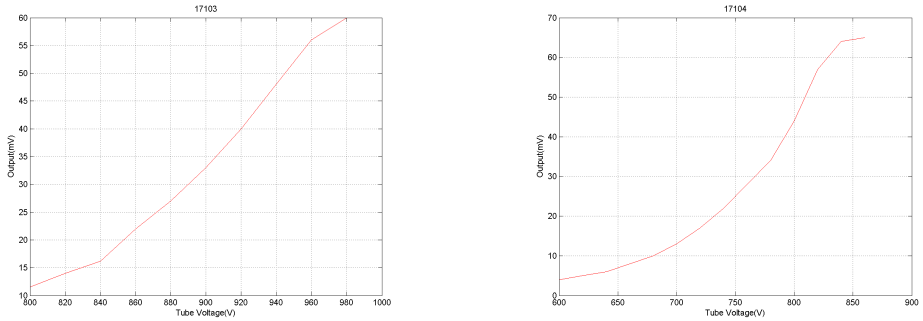

Figure 1.2: PMT Gain vs. HV supply curves. This is shown for PMT17103 and PMT17104.

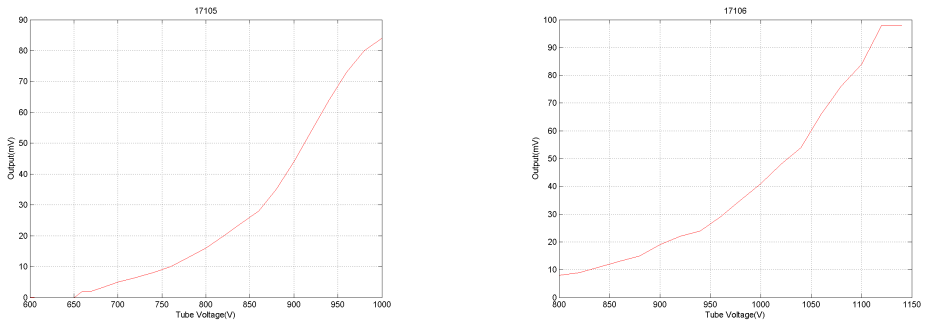

Figure 1.3: PMT Gain vs. HV supply curves. This is shown for PMT17105 and PMT17106.

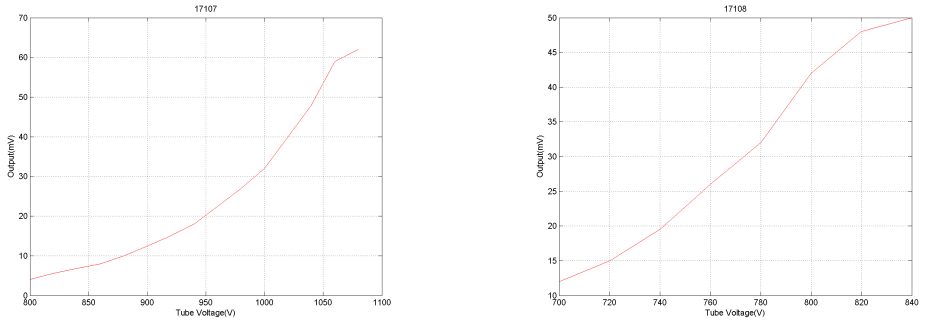

Figure 1.4: PMT Gain vs. HV supply curves. This is shown for PMT17107 and PMT17108.

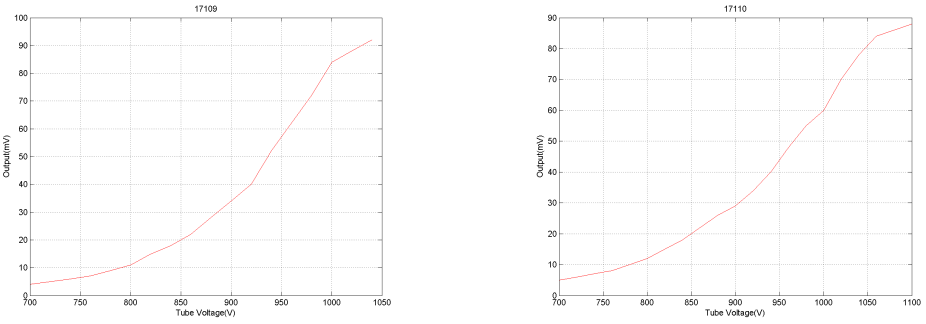

Figure 1.5: PMT Gain vs. HV supply curves. This is shown for PMT17109 and PMT17110.

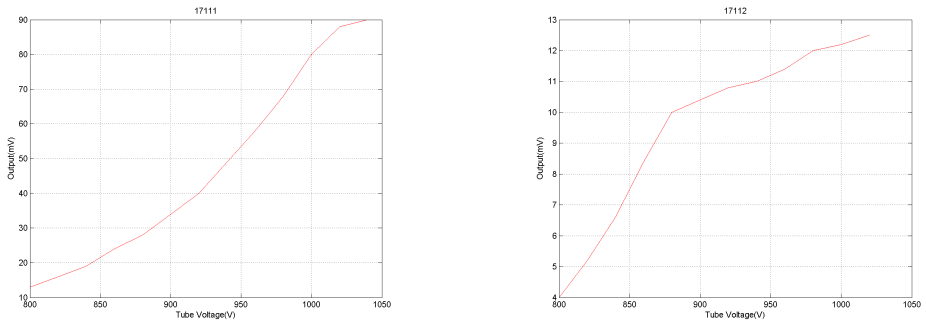

Figure 1.6: PMT Gain vs. HV supply curves. This is shown for PMT17111 and PMT17112.

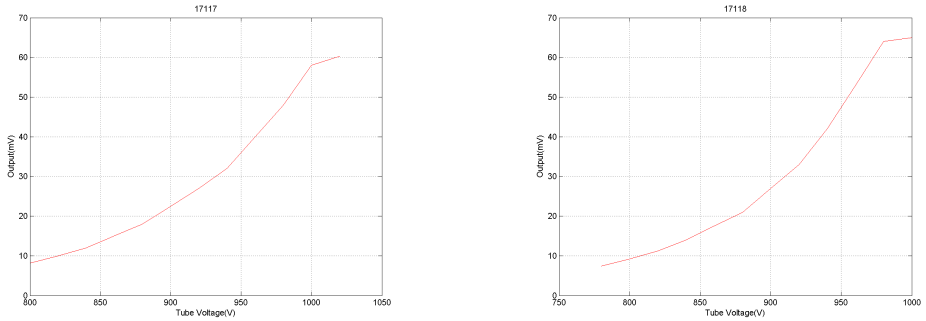

Figure 1.7: PMT Gain vs. HV supply curves. This is shown for PMT17117 and PMT17118.

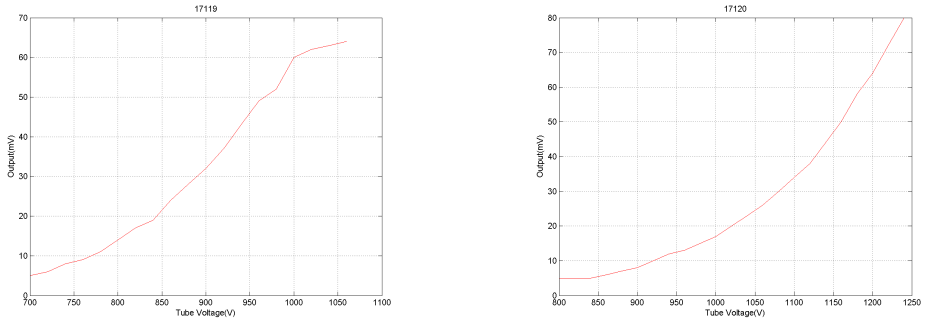

Figure 1.8: PMT Gain vs. HV supply curves. This is shown for PMT17119 and PMT17120.

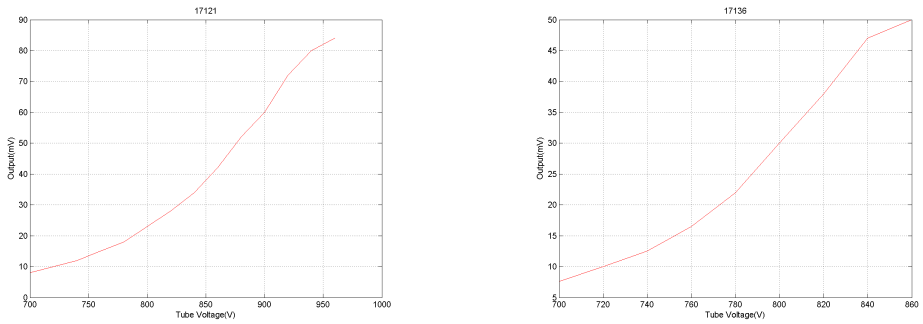

Figure 1.9: PMT Gain vs. HV supply curves. This is shown for PMT17121 and PMT17136.

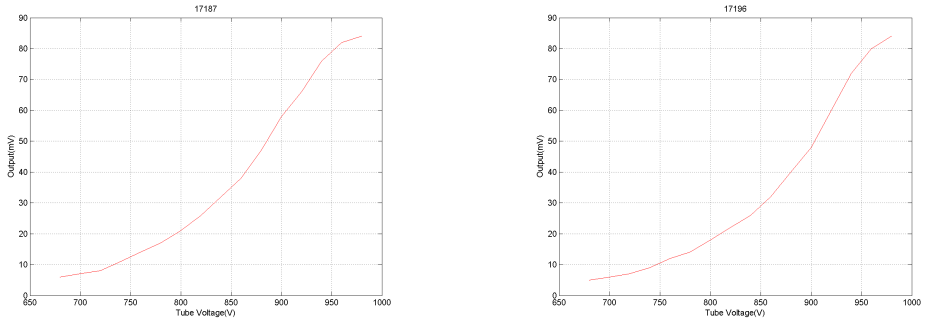

Figure 1.10: PMT Gain vs. HV supply curves. This is shown for PMT17187 and PMT17196.

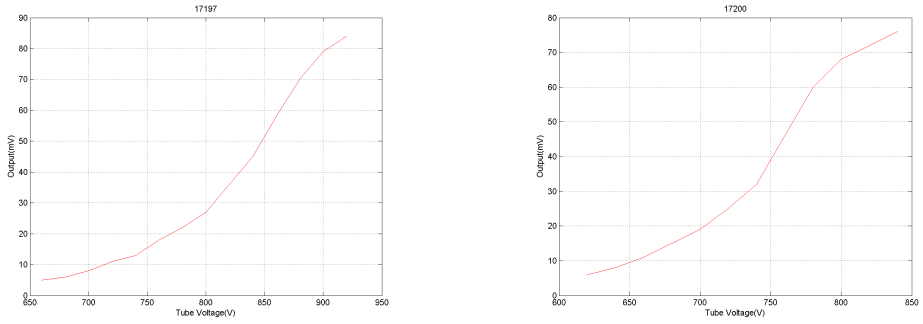

Figure 1.11: PMT Gain vs. HV supply curves. This is shown for PMT17197 and PMT17200.

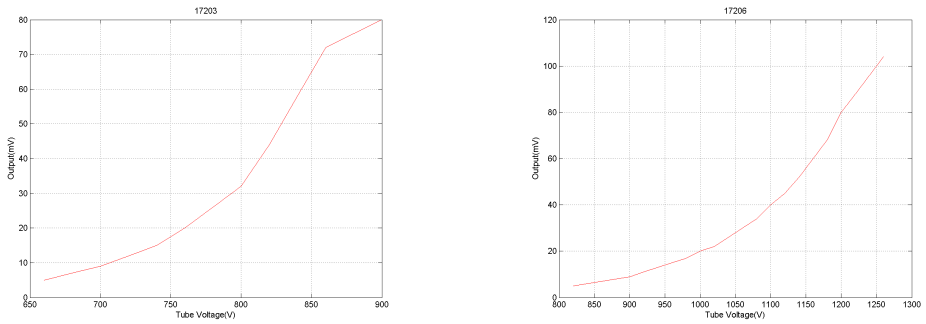

Figure 1.12: PMT Gain vs. HV supply curves. This is shown for PMT17203 and PMT17206.

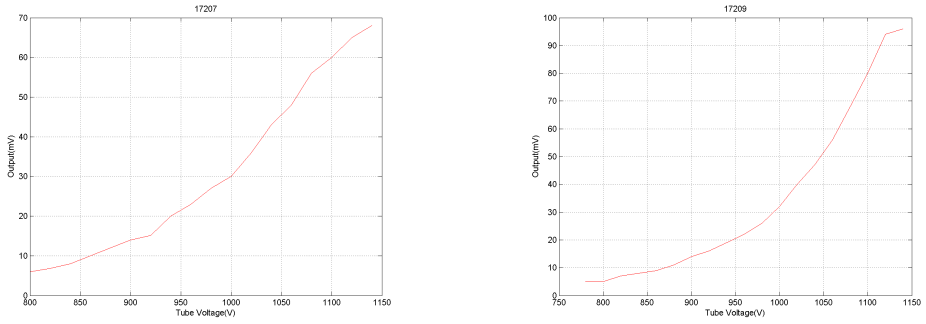

Figure 1.13: PMT Gain vs. HV supply curves. This is shown for PMT17207 and PMT17209.

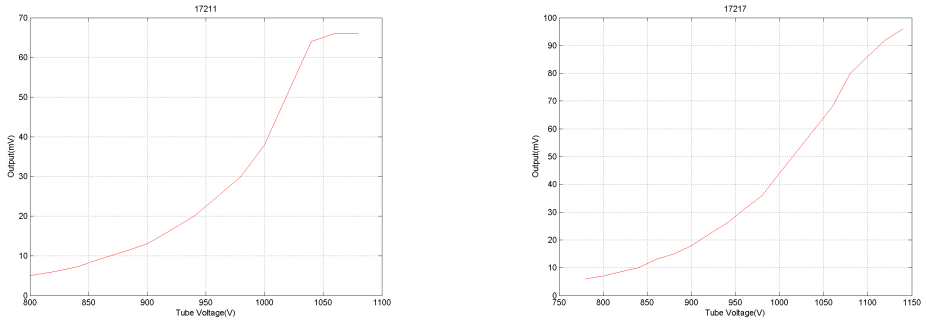

Figure 1.14: PMT Gain vs. HV supply curves. This is shown for PMT17211 and PMT17217.

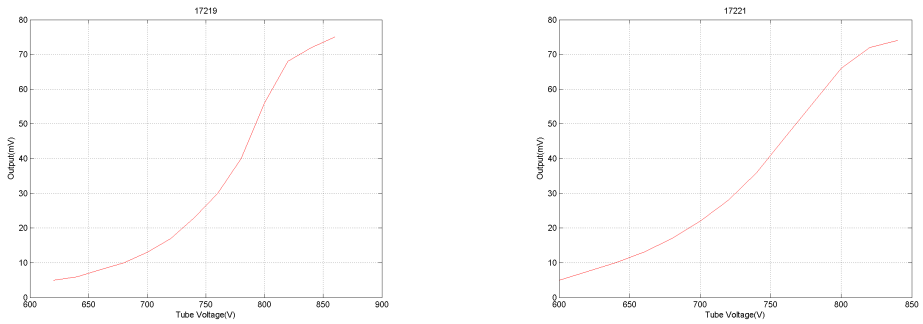

Figure 1.15: PMT Gain vs. HV supply curves. This is shown for PMT17219 and PMT17221.

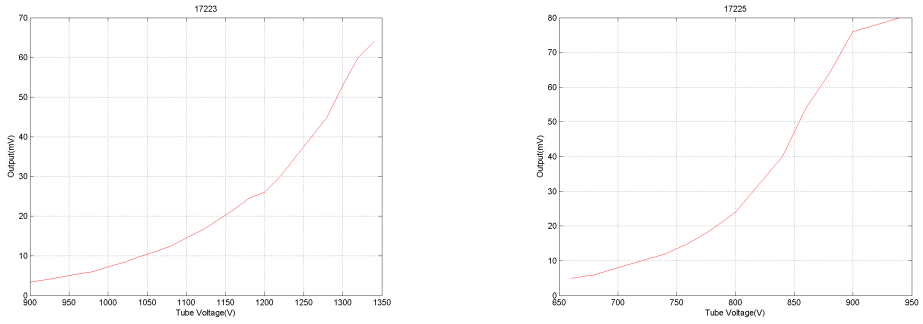

Figure 1.16: PMT Gain vs. HV supply curves. This is shown for PMT17223 and PMT17225.

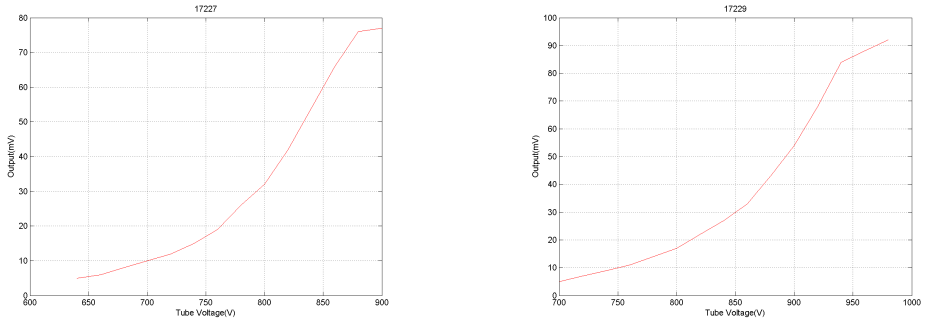

Figure 1.17: PMT Gain vs. HV supply curves. This is shown for PMT17227 and PMT17229.

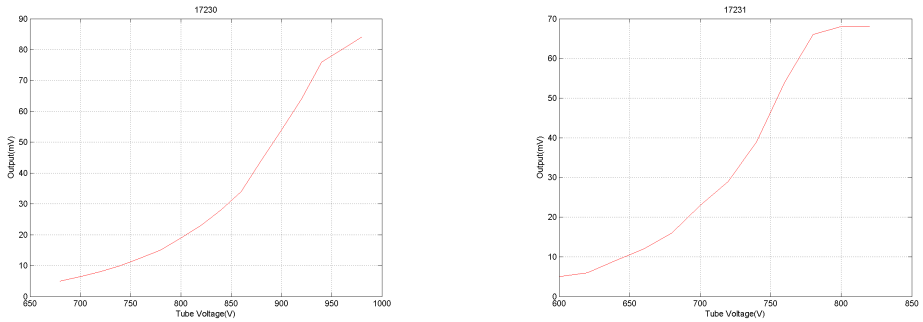

Figure 1.18: PMT Gain vs. HV supply curves. This is shown for PMT17230 and PMT17231.

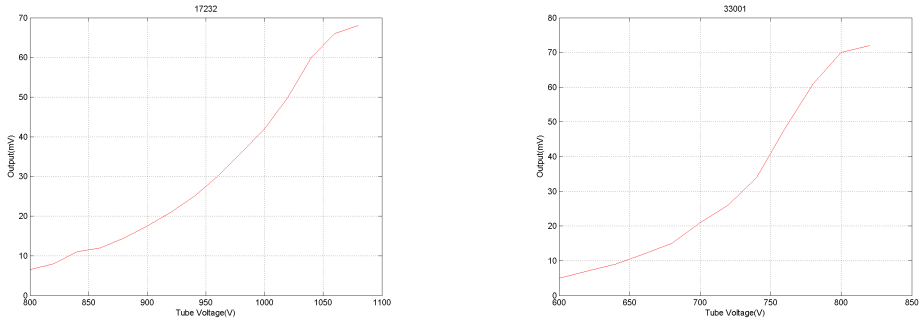

Figure 1.19: PMT Gain vs. HV supply curves. This is shown for PMT17232 and PMT33001.

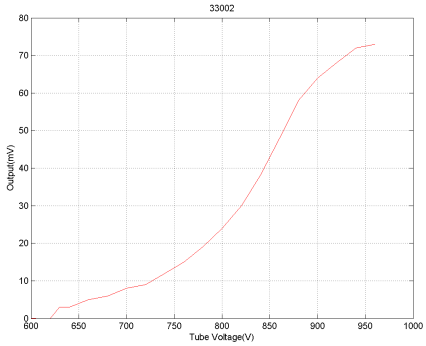

Figure 1.20: PMT Gain vs. HV supply curves. This is shown for PMT33002.

APPENDIX II

The following figures show the results of the magnetic field tests carried out on two of the PM tubes for the BSC. The average amplitude of the signals from the PM tube in the magnetic field is shown by the points on the red line and are an average of 50 readings. Similarly, the average amplitude of the signals from the PM tube outside the magnetic field is shown by the points on the blue line and are an average of 50 readings. The magnetic field was increased to determine the maximum field and optimum PM tube orientation w.r.t the field that the PM tubes could operate in. The results show a failure level at approximately 950G and with a perpendicular orientation w.r.t the magnetic field. The tubes were shielded with mu-metal shields but not placed in the Aluminum PMT boxes.

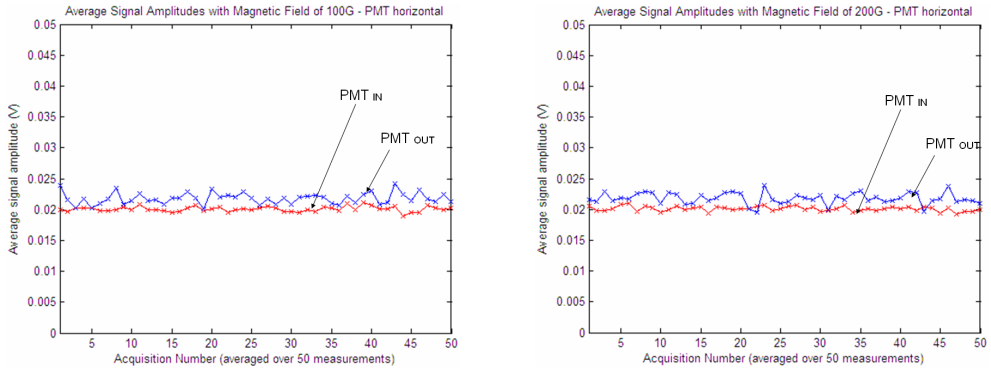

Figure 2.1: Results of the PMT magnetic field test acquisitions at 110G (left) and 200G (right).

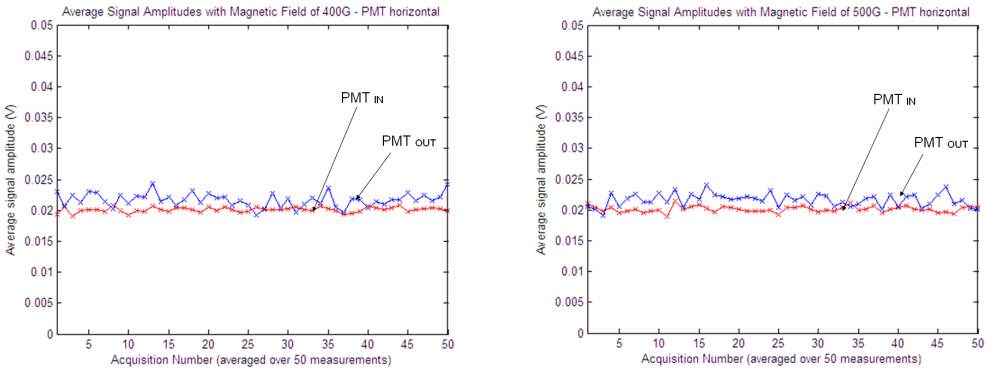

Figure 2.2: Results of the PMT magnetic field test acquisitions at 400G (left) and 500G (right)

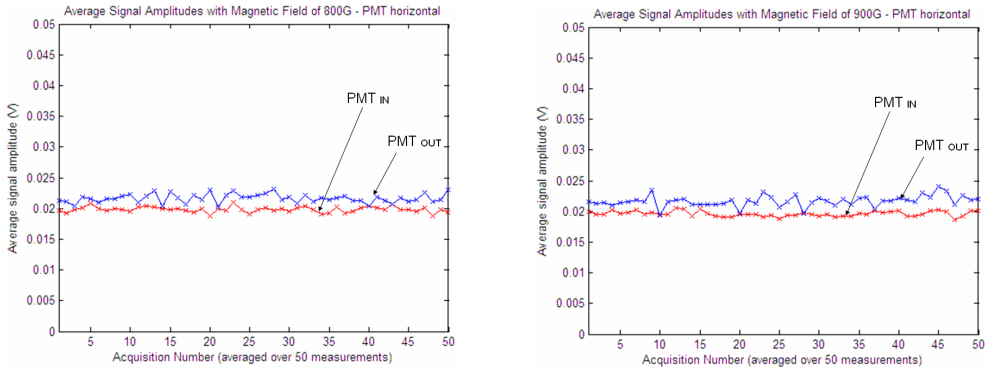

Figure 2.3: Results of the PMT magnetic field test acquisitions at 800G (left) and 900G (right)

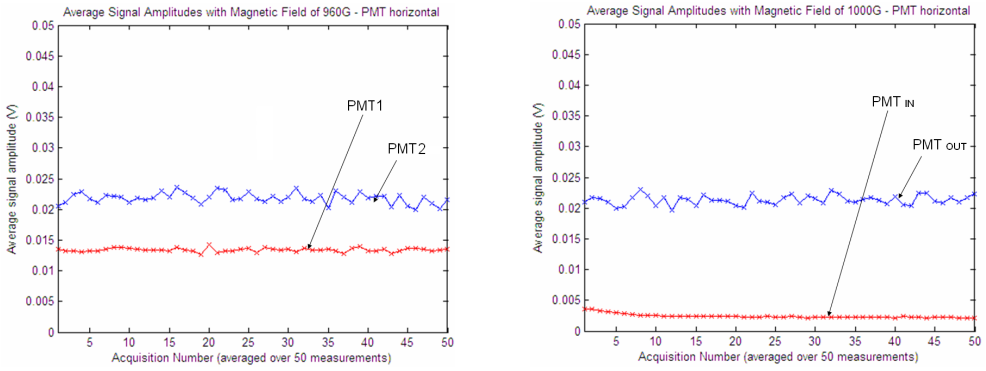

Figure 2.4: Results of the PMT magnetic field test acquisitions at 960G (left) and 1000G (right). The tube began to fail at approximately 940G. The output signal was totally diminished at **B = 1000G.**

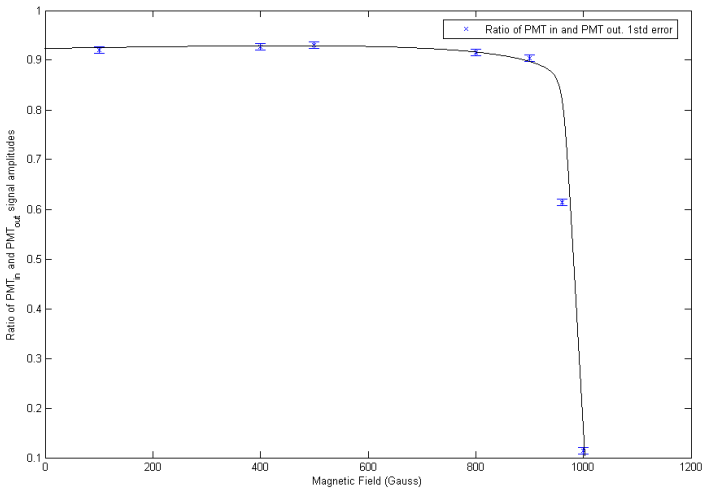

Figure 2.5: Ratio of gains of the two PMTs used in the magnetic field tests. As can be seen, the gain of the PMT in the magnetic field diminishes to zero at approximately 950G.

APPENDIX III

Figures 3.1 to 3.20 show the signal amplitude histograms gathered for Scintillator Tile/PMT pair.s. The histograms have been normalized to the total number of counts as some acquisitions were left to run for a longer time. By normalizing the histograms, the histograms are more easily comparable. The histograms show that, for the specified voltage, a clear distinction between the signal and the noise can be seen.

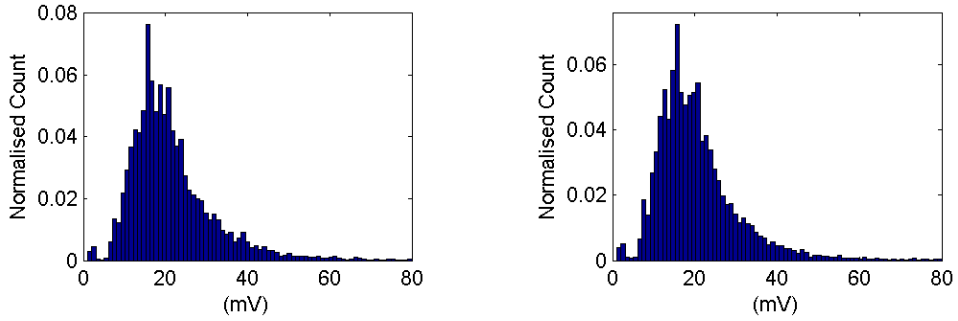

Figure 3.1: Amplitude Spectra for tile/tube pair. PMT17065/C1B at 964V and PMT17102/C1C at 803V.

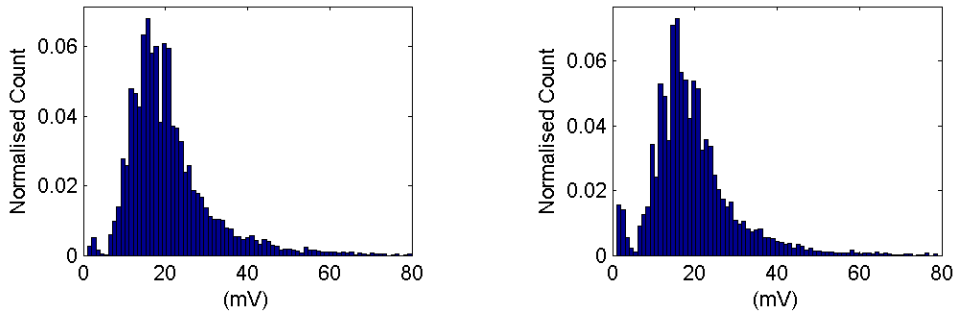

Figure 3.2: Amplitude Spectra for tile/tube pair. PMT17103/C3D at 864V and PMT17104/6S at 858V.

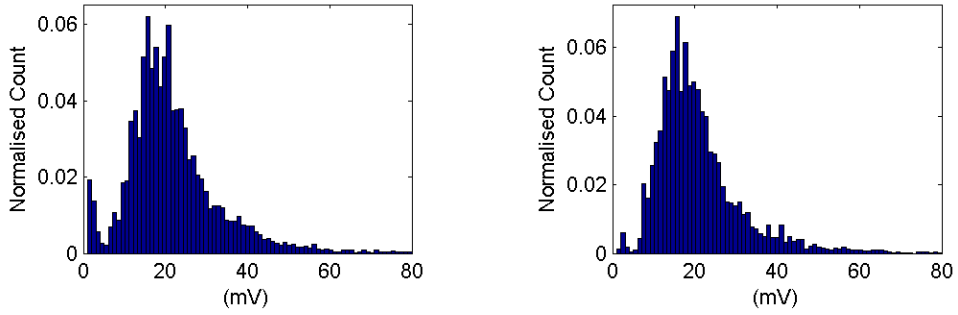

Figure 3.3: Amplitude Spectra for tile/tube pair. PMT17055/S9 at 974V and PMT17106/C5C at 1049V.

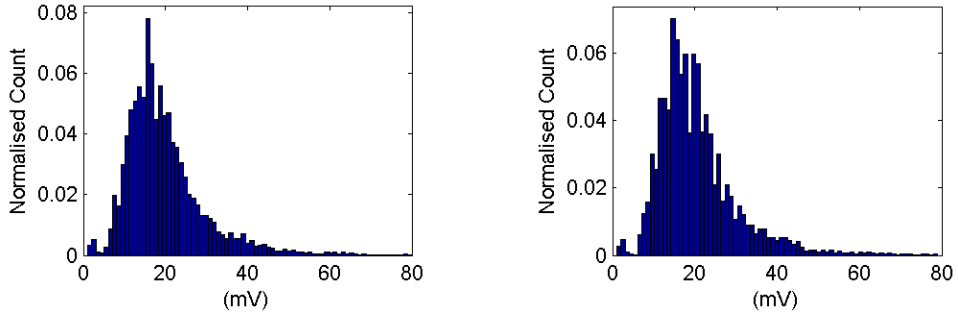

Figure 3.4: Amplitude Spectra for tile/tube pair. PMT17107/C4B at 1002V and PMT17108/C2D at 758V.

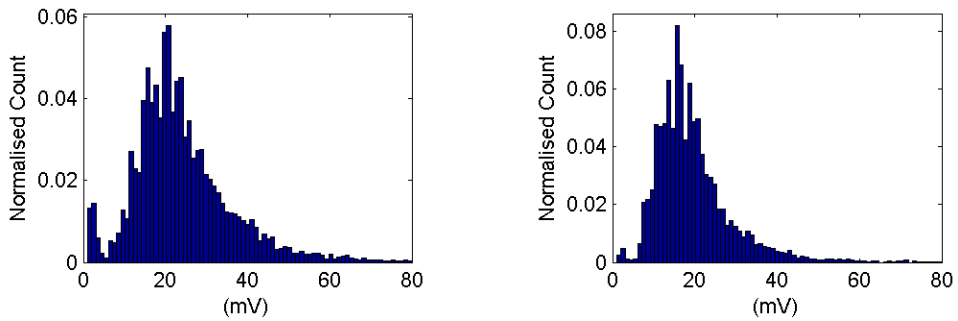

Figure 3.5: Amplitude Spectra for tile/tube pair. PMT17109/1S at 1017V and PMT17110/C1A at 984V.

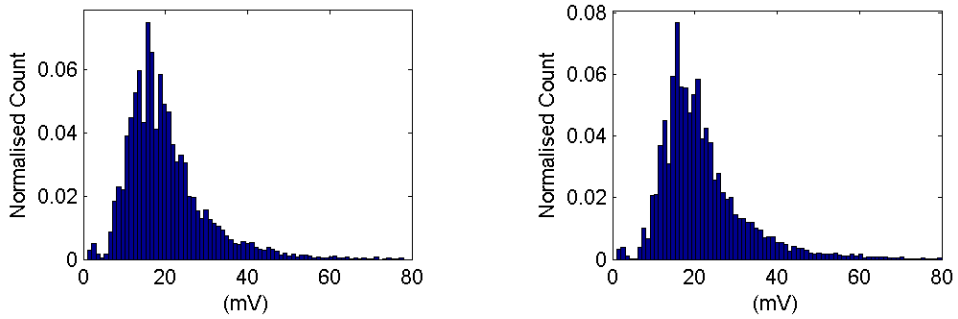

Figure 3.6: Amplitude Spectra for tile/tube pair. PMT17111/C3B at 997V and PMT17113/C2C at 967V.

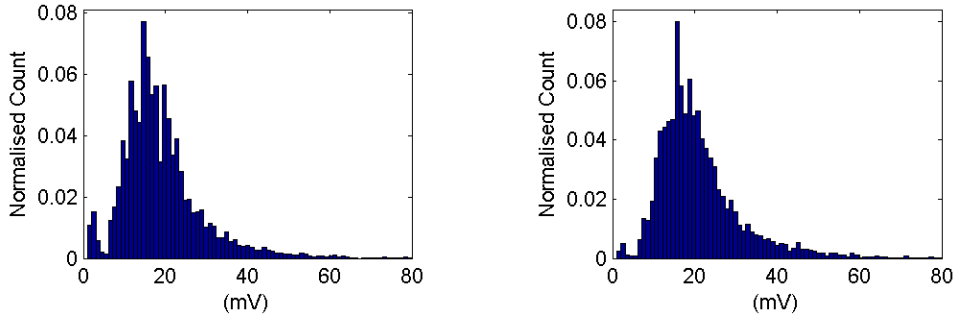

Figure 3.7: Amplitude Spectra for tile/tube pair. PMT17114/13S at 1028V and PMT17115/C4A at 1167V.

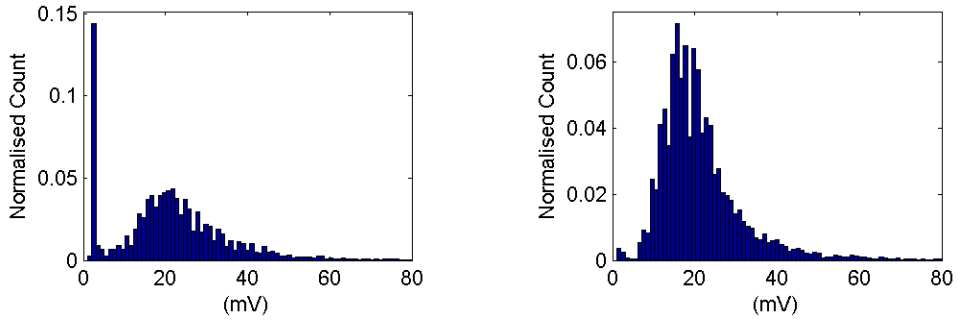

Figure 3.8: Amplitude Spectra for tile/tube pair. PMT33001/11L at 807V and PMT17116/C2B at 1149V.

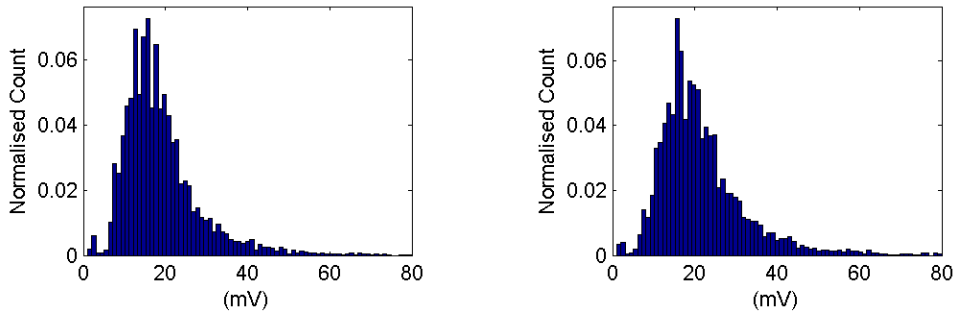

Figure 3.9: Amplitude Spectra for tile/tube pair. PMT17117/C5B at 911V and PMT17118/C3C at 925V.

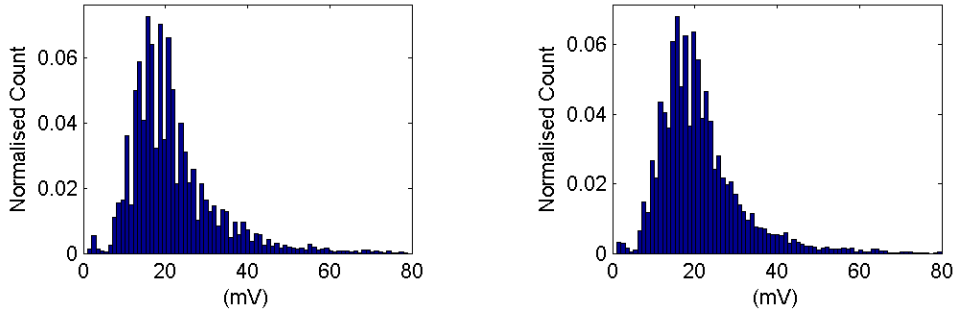

Figure 3.10: Amplitude Spectra for tile/tube pair. PMT17119/C6D at 966V and PMT17120/C2A at 1189V.

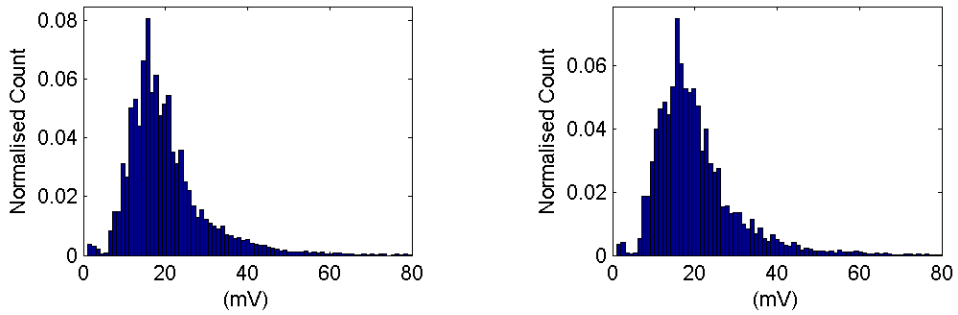

Figure 3.11: Amplitude Spectra for tile/tube pair. PMT17121/C3A at 923V and PMT17136/C4C at 792V.

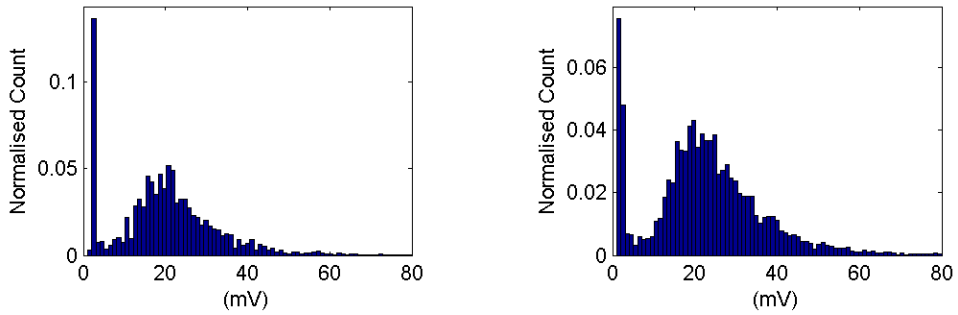

Figure 3.12: Amplitude Spectra for tile/tube pair. PMT17187/10L at 960V and PMT33002/13L at 984V.

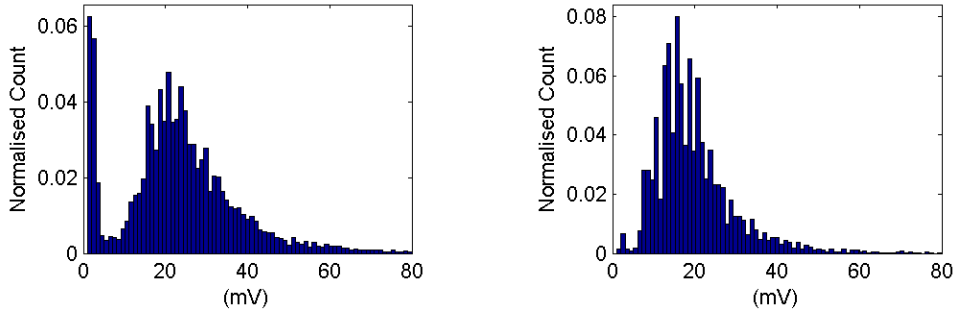

Figure 3.13: Amplitude Spectra for tile/tube pair. PMT17197/1L at 947V and PMT17200/C6A at 793V.

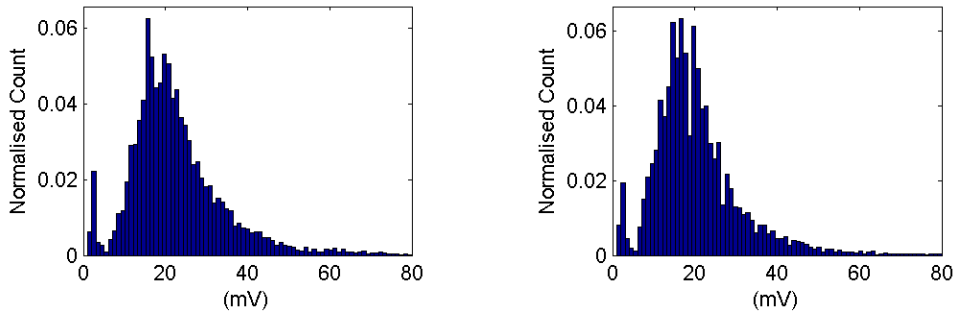

Figure 3.14: Amplitude Spectra for tile/tube pair. PMT17203/16S at 941V and PMT17206/14S at 1206V.

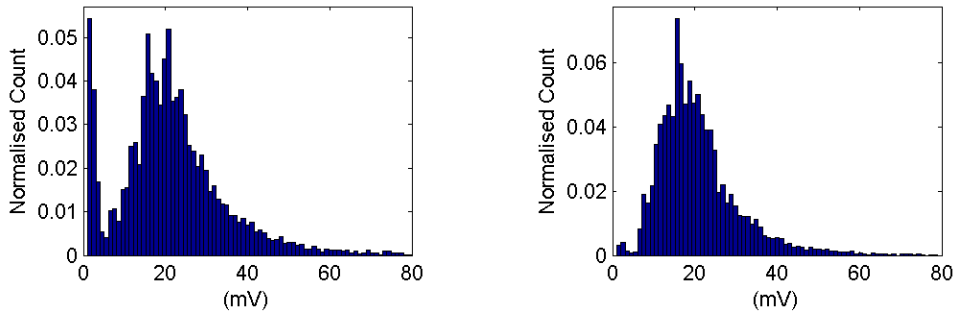

Figure 3.15: Amplitude Spectra for tile/tube pair. PMT17207/11S at 943V and PMT17209/C1D at 1098V.

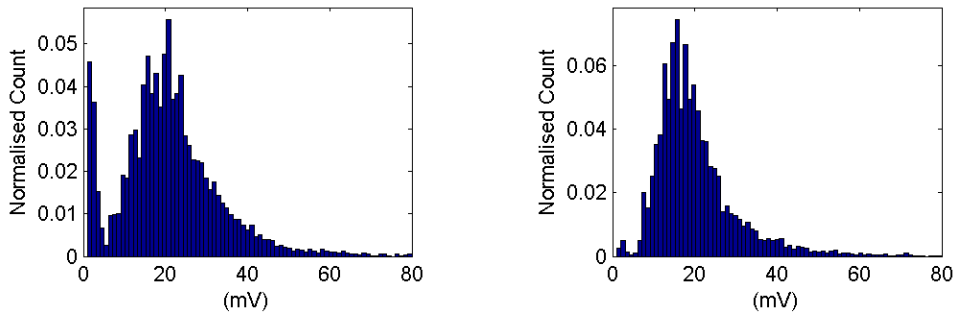

Figure 3.16: Amplitude Spectra for tile/tube pair. PMT17207/11S at 943V and PMT17217/C5A at 993V.

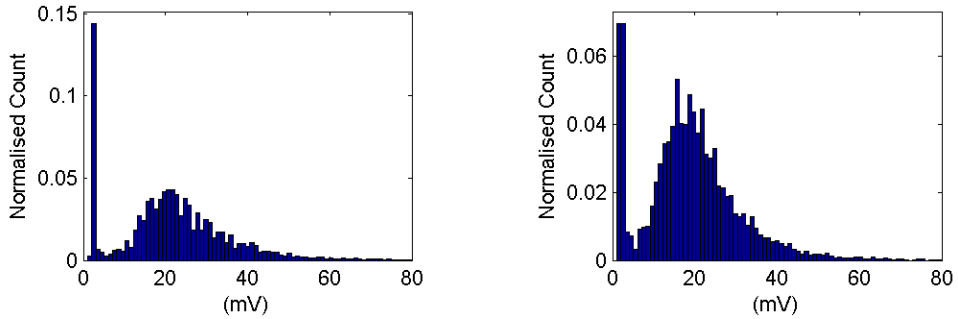

Figure 3.17: Amplitude Spectra for tile/tube pair. PMT17219/16L at 865V and PMT17225/14L at 967V.

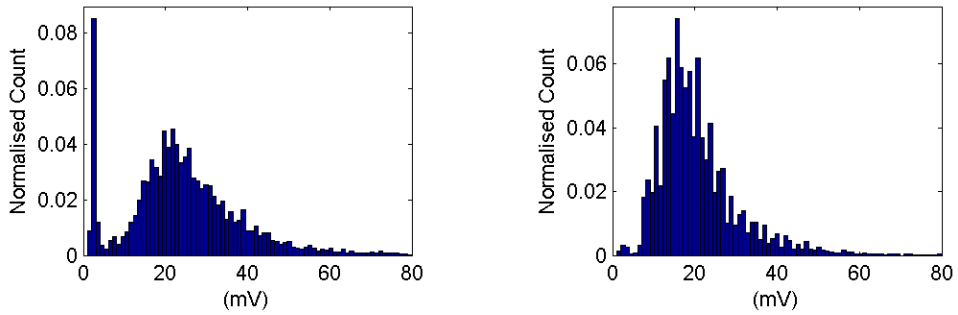

Figure 3.18: Amplitude Spectra for tile/tube pair. PMT17227/5L at 950V and PMT17229/C4D at 798V.

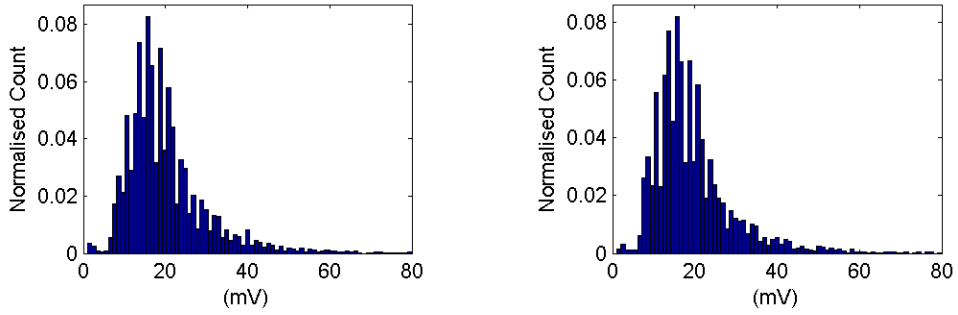

Figure 3.19: Amplitude Spectra for tile/tube pair. PMT17230/C6C at 799V and PMT17231/C6B at 930V.

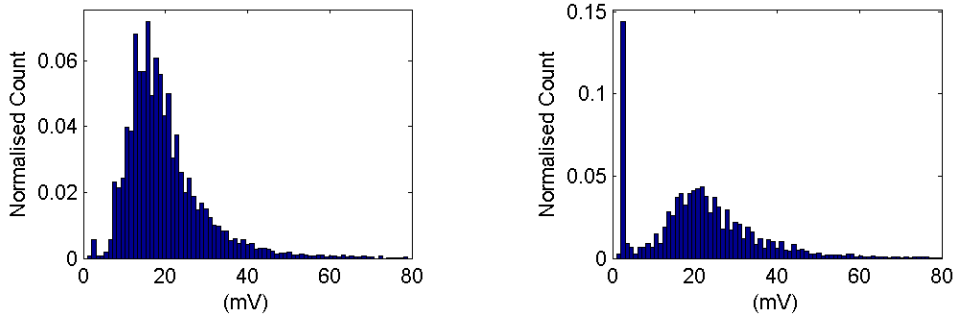

Figure 3.20: Amplitude Spectra for tile/tube pair. PMT17232/C5D at 900V and PMT33001/11Lat 870V.